Monte Carlo simulations of a neutron veto for the XENONnT dark matter experiment

Masterarbeit

am Fachbereich Physik, Mathematik und Informatik
Johannes Gutenberg-Universität Mainz

JG|U

JOHANNES GUTENBERG
UNIVERSITÄT MAINZ

Diego Ramírez García
Mainz, 05.2017

ABSTRACT

XENON1T is the first multi-ton dual-phase xenon time projection chamber (TPC), aiming to directly detect dark matter in the form of weakly interacting massive particles (WIMPs). With dark matter search already operative at the Laboratori Nazionali del Gran Sasso in Italy, a spin-independent WIMP-nucleon cross section sensitivity of $1.6 \cdot 10^{-47}$ cm² for WIMP masses of 50 GeV/c² will be reached in an exposure of two years.

With the goal of improving sensitivity by another order of magnitude, the infrastructure of the experiment has been designed for XENON1T to be rapidly upgraded to XENONnT, a detector already under development, with a 35 % larger photosensor coverage than its predecessor and containing about twice the mass of xenon target. With an improved self-shielding due to a larger TPC, it will be more effective to define a fiducial volume in which the external backgrounds can be reduced to a negligible level.

In order to optimize this volume for the dark matter search, the possibility of developing a liquid scintillator outer detector has been studied via Monte Carlo-based simulations. This thesis describes the design and simulation of a neutron veto around the XENONnT outer cryostat, consisting of acrylic vessels filled with gadolinium-loaded organic liquid scintillator. With help of the GEANT4 toolkit, the efficiency of this neutron veto against radiogenic nuclear recoil background has been evaluated.

CONTENTS

LIST OF FIGURES

LIST OF TABLES

LIST OF ABBREVIATIONS

ALP   Axion-like particle

BBN   Big Bang nucleosynthesis

bis-MSB 1,4-bis(2-methylstyryl)benzol

B-LS   Boron-doped liquid scintillator

CAD   Computer-aided design

CE   Collection efficiency

CMB   Cosmic microwave background

DRU   Differential rate units

ER   Electronic recoil

FV   Fiducial volume

Gd-LS   Gadolinium-doped liquid scintillator

GXe   Gaseous xenon

LAB   Linear alkylbenzene

ΛCDM Λ cold dark matter

LCE   Light collection efficiency

LNGS   Laboratori Nazionali del Gran Sasso (National Gran Sasso Laboratory)

LS   Liquid scintillator

LSP   Lightest supersymmetric particle

LXe   Liquid xenon

LY   Light yield

MACHO Massive, compact, non-luminous object

MC   Monte Carlo

MOND   Modified Newtonian dynamics

NEST   Noble Element Simulation Technique

NR   Nuclear recoil

PE   Photoelectron

PMT   Photomultiplier tube

PPO   2,5-diphenyloxazole

PTFE   Polytetrafluoroethylene

PXE   Phenylxylylethane

QE   Quantum efficiency

SF   Spontaneous fission

SI   Spin independent

SM   Standard Model of particle physics

SS   Stainless steel

SUSY   Supersymmetric model

TeVeS   Tensor–vector–scalar gravity

TMHA   3,5,5-trimethylhexansaeure

TPC   Time projection chamber

UV   Ultraviolet

VUV   Vacuum-ultraviolet

WIMP   Weakly interacting massive particle

WLS   Wavelength shifter

INTRODUCTION

Dark matter is a hypothetical form of matter that interacts neither strongly nor electromagnetically with ordinary baryonic matter. The presence of dark matter is needed to explain the observed large-scale structures and galaxies and, although its existence has been inferred indirectly, its nature remains unknown. Chapter 2 reviews some of the relevant observational evidence and gives an insight into the most promising dark matter candidates and the corresponding detection techniques. Among them, the weakly interacting massive particles (WIMPs) hypothesis is a very plausible one and experiments pursuing its detection are now reaching very high sensitivities.

The XENON Dark Matter Project aims for the detecion of WIMPs via their scattering off xenon nuclei, by deploying ultra-low background dual phase liquid xenon (LXe) time projection chambers (TPCs). The detection principle of this kind of detector and the experiments whitin the XENON collaboration are described in Chapter 3. After the successful operation of the XENON100 experiment at the Laboratori Nazionali del Gran Sasso (LNGS) in Italy, the XENON1T experiment was built and is currently taking data at the same location. With about 2 tonnes of target, it constitutes the largest operational LXe TPC at the time of writing. The unprecedented XENON1T projected sensitivity for the spin-independent WIMP-nucleon elastic scattering cross section is $\sigma \approx 2 \cdot 10^{-47}$ cm², for two years of detector exposure. After that, an upgrade towards the XENONnT experiment is already planned. XENONnT will use ~ 6 tonnes of xenon target, and its relatively rapid development will benefit from most of the existing XENON1T infrastructure.

In the context of this upgrade, preliminary estimates of the electronic (ER) and nuclear recoil (NR) bakgrounds yield that radiogenic NR background in XENONnT is no longer negligible, as for the time of exposure of its predecessor. This thesis presents the conceptual design and simulations of a liquid scintillatior (LS) neutron veto for the XENONnT experiment, with the goal of tagging the bakground events from radiogenic neutrons.

Chapter 4 gives an owerview on the operational principle and the most relevant physical properties of an organic LS, and develops the possibility of metal doping for such materials, to enhance their neutron tagging capabilities. The approach taken here follows the description of the different features of organic LSs while referring to operative neutrino search experiments deploying this technique, which in the last decades has started to be adopted also for veto purposes in dark matter direct searches.

Chapter 5 is devoted to the implementation of the neutron veto model, along with the simulations of the contamination of the components considered to assess the radiogenic NR background in XENONnT.

The results from these simulations are derived in Chapter 6. After a dedicated characterization of the main properties of the implemented neutro veto, the NR background expected for XENONnT is obtained, with and without the activation of this new outer detector, for which multiple configurations have been defined. By comparing both scenarios, values for the tagging efficiency of the neutron veto are calculated.

A summary of the results is presented in Chapter 7, where some important questions regarding the future development of the neutron veto are also addressed.

2

PARTICLE DARK MATTER

2.1 OBSERVATIONAL EVIDENCE

The possible presence of invisible but gravitating matter as an explanation for the *missing mass problem* in Astronomy has been studied for almost one century. First attempts to derive the total density of matter in the solar vicinity were made by Öpik [1], Kapteyn [2], Jeans [3] and Oort [4], with the term *dark matter* already coined, although referring to a wrong or incomplete physical expanation of the observed phenomena.

In 1933 Zwicky presented the first evidence of dark matter in our present understanding [5]. Zwicky measured the radial velocities of galaxies in the Coma Cluster, determined the corresponding mass by applying the virial theorem and discovered that the total mass withing a cluster radius exceeds that of the stars by about 400 times. He attributed the discrepancy to a (dark) non-luminous matter component. This prediction was made before gas radiating X-rays and dust radiating in the infrared could be observed and was not firmly recognized by the astronomical community. Decades later, in the 1970s, Vera Rubin and collaborators studied the rotation curves of spiral galaxies and also found evidences for a missing mass component. Once the techniques to measure the kinematics of galaxies allowed to account for all their massive content, this indication was established as a hint for the existence of dark matter [6].
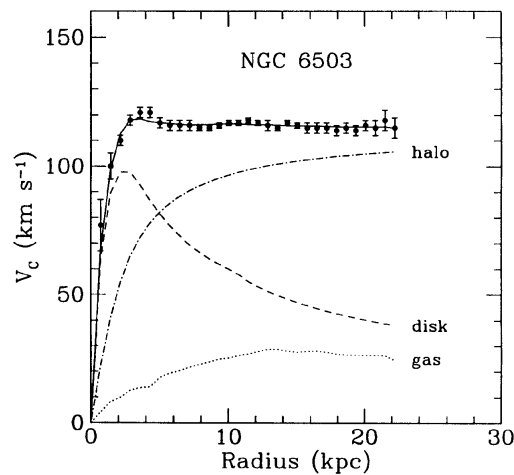
Figure 2.1: Measured rotation curve of the NGC 6503 galaxy, located at the edge of the Local Void. To reproduce the observed behavior, the contribution from the velocity profile of the dark matter halo is introduced [7].

From a measurement of the rotational velocity of stars and gas as a function of the radius r one can compute the mass $M(r)$ of the galaxy enclosed within that radius. In Newtonian dynamics the circular velocity should scale as $v(r) \propto r^{-1/2}$, hence decrease for radii beyond the extent of the stellar disk. Instead, rotation curves of spiral galaxies are flat, as illustrated in Figure 2.1. This indicates the presence of a *halo* of non-luminous matter with mass density profile $\rho(r) \propto r^{1/2}$, superimposed upon the luminous disk.

The existence of dark matter has been since then inferred using many diverse and precise observations. Further evidence for invisible matter in the scale of galactic clusters (as for Zwicky's studies) is the phenomenon of gravitational lensing predicted by Einstein [8], that occurs when a massive foreground object bends light from distant objects behind it. This light is seen as a distorted replica of the background object, that can be pictured multiple times, and measurements of the light deflection provide the possibility to determine the mass of the *lens*. When calculating the corresponding mass-to-light ratio, the presence of a non-luminous, non-baryonic component is also revealed (along with the contribution from X-rays emitting plasma, a non-luminous, baryonic component). A visual example of a gravitational lens is shown in Figure 2.2(a)[1] For cases like this one, in which the lens (usually a galaxy cluster) is in the line of sight between the object and the observer, the distortion appears in form of rings.

(a)   (b)
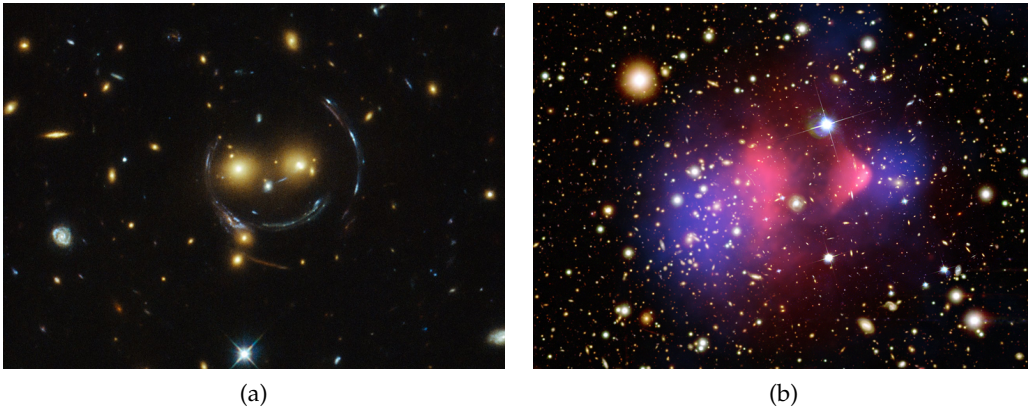
Figure 2.2: Examples of gravitational lensing. (a) Galaxy cluster SDSS J1038+4849, as measured by the NASA/ESA Hubble Space Telescope. (b) The Bullet cluster with two colliding galaxy clusters. Images courtesy of NASA.

Another very strong hint has been obtained by observing the collision of galaxy clusters [9]. An example of such collision for the Bullet cluster (1E 0657-558) is shown in Figure 2.2(b). The distribution of intracluster plasma (pink) is measured from its X-ray signature and the mass distribution (blue) is inferred from gravitational lensing. During the merger of both clusters, the hot baryonic components interact, while the dark matter distributions pass through each other with mini-

---

1 The shape of this particular lens, observed in 2015, is the reason why astronomers have referred to it as the *smiling lens*.

mal interaction, consistent with the expectation of collisionless dark matter.

Evidences on a universal scale are provided by the measurements of the temperature anisotropies in the cosmic microwave background (CMB). When the Universe became cold enough, it allowed for the combination of free electrons with nuclei to form neutral atoms (*recombination*), hence becoming transparent to photons (*photon decoupling*). The resulting CMB allows an insight into the Universe at that time, $\sim 380{,}000$ years after the Big Bang. These measurable anisotropies represent the variations in the density of the gas at the surface of last scatter, as well as variations in the gravitational potential of the Universe, also along the photon path.
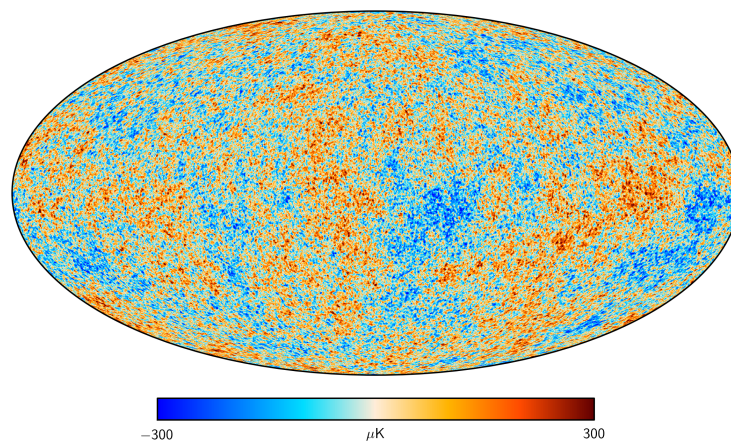
Figure 2.3: CMB temperature map. The primordial temperature fluctuations responsible formation of large-scale structure are shown. Like illustrated in the legend, these anisotropies are at the level of $10\,\mu s$, for an average temperature of $2.725\,K$ [10].

Figure 2.3 shows the microwave sky map, as measured by the Planck satellite mission in 2015. The image reveals the primordial fluctuations that eventually led to the gravitational growth of structures like galaxies. Since the anisotropies are defined on a sphere, they can be expanded in terms of spherical harmonics, where, for a Gaussian distribution of the fluctuations, the variance of the coefficients encodes most of the cosmological information. The power spectrum of these fluctuations can be fitted to a six-parameter model, which describes our present understanding of the cosmos: the Λ cold dark matter model (ΛCDM), where *cold* reads for dark matter with low random velocities and Λ refers to the cosmological constant necessary to explain the present-day accelaration of the expansion of the Universe. Last measurements [11] yield a flat shape of the Universe, with $4.9\,\%$ of its matter-energy content consisting of baryonic matter, $26.5\,\%$ of dark matter and $68.6\,\%$ of dark energy. Numerical simulations based on the ΛCDM model, considered as the *standard* model of Big Bang cosmology, successfully predict the formation of the observed structures and no compelling signs show deviations from it [12].

2.2   THEORETICAL CANDIDATES

Despite its rich phenomenology, the nature of dark matter is yet to be revealed. In order to explain it, some theories estimate that the gravitational laws must be redefined at large scales in order to understand the overall matter in the Universe, assuming that it has properties described by the Standard Model of particle physics (SM).

The modified Newtonian dynamics (MOND) approach [13] and its relativistic extension, the tensor–vector–scalar gravity (TeVeS) [14] sketch the solution for some of the observed phenomena without accounting for the dark matter component. They postulate deviations from the Newtonian laws for high orbiting velocities, which serve to explain the observed behaviors in the rotation of galaxies, but fail when trying to explain evidence at larger scales, such as the grvitational lensing effect [15].

An attempt to explain dark matter in terms of baryonic constituents are the massive, compact, non-luminous objects (MACHOs), which include brown dwarfs, neutron stars or black holes, among others, which rarely emit radiation. Extensive astronomical surveys constrain the possible amount of MACHOs in our galactic dark matter to a maximum value of 20 % [16]. Moreover, results from measurements of the CMB temperature anisotropies agrees with the abundance of elements predicted by Big Bang nucleosynthesis (BBN), therefore ruling out the baryonic nature of dark matter.

Whithin the SM, the neutrino used to be considered as a good candidate for non-baryonic dark matter. However, CMB measurements combined with large-scale structure data suggest that the physical neutrino density is not abundant enough to account for the predicted fraction of dark matter in the Universe. In any case, the neutrino component of dark matter would be a *hot* one, since they travelled at relativistic speeds at the moment of decoupling, hence being unable to reproduce the observed large structures.

From the cosmological evidence previously described it can be concluded that dark matter is massive, since it can be predicted from gravitational lensing, and can only interact weakly, since it does not emit or absorb electromagnetic radiation and a coupling via the strong force has not been observed in the form of interactions with ordinary matter. In addition, a dark matter candidate needs to be stable or very long-lived, since otherwise it would have decayed by now, and because its predicted abundance has not changed during the evolution of the Universe.

Among the variety of hypothetical candidate particles that could make up dark matter, WIMP is a well motivated one, naturally arising in several extensions of the SM like, e.g., the lightest supersymmetric particle (LSP) in supersymmetry

models (SUSY). Since no dark matter constituent has been found yet, WIMP is a general term reading for a kind or particle featuring the behavior described in the previous paragraph. If these kind of new elementary particles were in thermal equilibrium in the hot early Universe, their abundance today can be approximated by [17]:

$$\Omega_\chi h^2 \sim \frac{3 \cdot 10^{-27} cm^3 s^{-1}}{\langle \sigma_{ann} v \rangle} \tag{2.1}$$

where the index χ refers to the dark matter particle, σ_{ann} is the annihilation cross section of dark matter, v is the velocity and the brakets stand for thermally averaged variables. For a flat Universe in which the relic density of dark matter is a predicted variable, the corresponding interaction cross section of dark matter particles can be calculated. For the (small) resulting cross section, WIMPs are expected to have a mass in the range of a few GeV to ~ 10 TeV, in order to reproduce the observed gravitational effects.

Another good motivated dark matter candidates are the *axions* or axion-like particles (ALPs), but their small mass requires that they are produced out of thermal equilibrium, hence Equation (2.1) does not apply. See [15] for a review on these and other candidates and the corresponding detection techniques.

2.3 DIRECT DARK MATTER SEARCHES

For the framework of this thesis, only direct detection techniques of dark matter particles are introduced. However, indirect detection and collider search experiments aiming for the discovery of dark matter components are also running at the moment. For a detailed state of the art of dark matter searches see [18, 19].

A WIMP flux onto the Earth of $\sim 10^5$ cm^{-2}s^{-1} for a particle mass of ~ 100 GeV is predicted according to the local density of dark matter [19]. WIMPs may be directly detected by scattering off heavy nuclei in a very sensitive detector. The expected differential rate for elastic WIMP-nucleous scattering can be expressed as

$$\frac{dR}{dE_{nr}} = N_T \frac{\rho_{dm}}{m_\chi} \int_{v_{min}}^{v_{esc}} d\mathbf{v} \, f(\mathbf{v}) \, v \, \frac{d\sigma}{dE_{nr}} \tag{2.2}$$

where N_T is the number of target nuclei, ρ_{dm} is the local dark matter density in the galactic halo, m_χ is the WIMP mass, $f(\mathbf{v})$ is the WIMP velocity distribution function in the Earth frame and $d\sigma/dE_{nr}$ is the WIMP-nucleous differential cross section. The upper integration limit is the escape velocity in the Earth frame, while the lower limit is set by the minimum recoil energy required to produce a detection signal in a dark mater detector. For an elastic scattering, the nuclear recoil energy is

$$E_{nr} = \frac{\mu_N^2 v^2}{m_N} \left(1 - cos\,\theta\right) \tag{2.3}$$

where m_N is the mass of the target nucleus, μ_N the reduced WIMP-nucleous mass and θ the scattering angle in the center of mass frame. The lower integration limit is directly derived from this equation, like

$$v_{min} = \sqrt{\frac{m_N\, E_{nr}^{th}}{2\mu_N^2}}\ . \tag{2.4}$$

In case of spin-independent (SI) WIMP-nucleous interaction, the differential WIMP-nucleous cross section from Equation (2.2) is given by

$$\frac{d\sigma}{dE_{nr}} = \frac{m_N\, \sigma_{SI}\, F_{E_{nr}}^2}{2\,\mu_N^2\, v^2} \tag{2.5}$$

where $F_{E_{nr}}^2$ stands for the nuclear form factor and σ_{SI} is the integrated SI WIMP-nucleous cross section,

$$\sigma_{SI} = A^2\, \frac{\mu_\chi^2}{\mu_p^2}\, \sigma_p^{SI}\ . \tag{2.6}$$

In Equation (2.6), σ_p^{SI} reads for the SI WIMP-proton cross section and μ_p is the reduced WIMP-proton mass. Inserting it into Equation 2.2, the proportionality of the differential event rate with A^2 is revealed. As a consequence, for SI dark matter search, target nuclei with high mass are preferred. Figure 2.4 shows the event rate (Equation 2.2) in differential rate units (DRU) for SI interactions in different target materials, for WIMPs with $m_\chi = 100\,\mathrm{GeV/c^2}$ and $\sigma_{SI} \sim 10^{-45}\,\mathrm{cm^2}$.
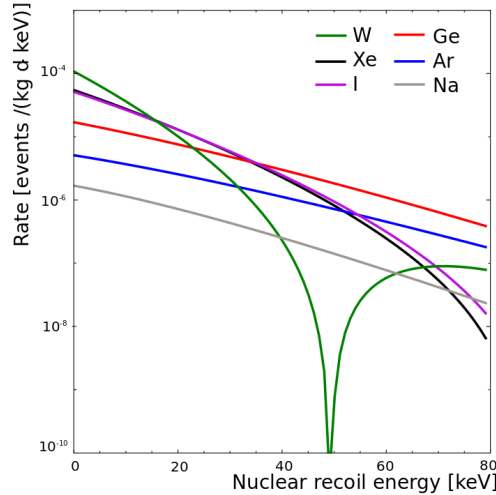
Figure 2.4: Differential event rate as a function of the recoil energy for a $100\,\mathrm{GeV/c^2}$ WIMP and a cross section $\sim 10^{-45}\,\mathrm{cm^2}$ for various target nuclei (W, Xe, I, Ge, Ar, Na) [18].

Considering $v_{esc} \approx 544\,\mathrm{km\cdot s^{-1}}$ in the galactic rest frame and inserting this value into Equation (2.3), the resulting energy trasferred to the atomic nucleous via

elastic collisions is $E_{nr} < 50\,\text{keV}$, which sets a benchmark for direct dark matter search. On the other side, by evaluating Equation (2.2) for the proper limits, the total event rate can be calculated. Expected event rates range from 10 to less than 1 event per tonne of detector material and year, depending on the WIMP-nucleous cross section.

XENON DARK MATTER PROJECT

The XENON Dark Matter Project aims to directly detect dark matter in the form of WIMPs with dual-phase TPCs filled with liquid xenon (LXe). In this chapter, the framework of the XENONnT detector is presented, after a description of the operational principle of a dual-phase LXe TPC and a brief introduction on past and present experiments of the XENON collaboration.

3.1 DETECTION PRINCIPLE

In the XENON TPCs, ultra pure LXe is used as a detector medium, with the advantage of combining a high WIMP sensitivity (see Figure 2.4) with excellent self-shielding capabilities for background reduction.

When a particle interacts with the LXe, the recoiling electrons (from interactions with β- or γ-rays) or nuclei (neutrons or WIMPs) excite and ionize the xenon atoms [20]. The excited xenon atom combines with another atom and produces an excited diatomic molecule (3.1), the de-excitation of which (3.2) releases scintillation light at 178 nm, in the vacuum-ultraviolet (VUV) region. The target is also ionized, creating free electrons and Xe^+ ions that form ionized molecules Xe_2^+ with neutral atoms (3.3). In the absence of an electric field, ionization electrons and ions can recombine (3.4), generating again excited xenon atoms. These atoms will eventually produce another excimer state (3.6), with the corresponding decay and emission of VUV photons (3.7).

$$Xe^* + Xe \rightarrow Xe_2^* \tag{3.1}$$
$$Xe_2^* \rightarrow 2Xe + h\nu \tag{3.2}$$
$$Xe^+ + Xe \rightarrow Xe_2^+ \tag{3.3}$$
$$Xe_2^+ + e^- \rightarrow Xe^{**} + Xe \tag{3.4}$$
$$Xe^{**} \rightarrow Xe^* + \text{heat} \tag{3.5}$$
$$Xe^* + Xe \rightarrow Xe_2^* \tag{3.6}$$
$$Xe_2^* \rightarrow 2Xe + h\nu \tag{3.7}$$

The detection principle in a dual-phase xenon TPC (Figure 3.1) makes use of an electric field across the target volume to remove the ionization electrons, such that electron-ion recombination is not possible and both scintillation light and charge signal can be measured. If the separate detection of the two signals is achieved, LXe becomes a detector with very high resolution, given that, for a given energy deposit, the total number of quanta, photons and electrons is constant.

A schematic description of the detection principle in a double-phase xenon detector is shown in Figure 3.1. The prompt scintillation light (S1) is detected by photomultiplier tubes PMTs top and bottom of the target volume. Thanks to the electric field applied accross the LXe target, ionization electrons do not recombine and drift upwards to the gaseous xenon GXe phase, where a stronger electric field extracts them into the GXe, where the excite xenon atoms, producing a secondary scintillation signal (S2). The simultaneous detection of both signals allows for a three-dimensional reconstruction of the event vertex and the ratio between the S1 and the S2 signals provides the possibility of to distinguish electronic ER from nuclear recoils NR.
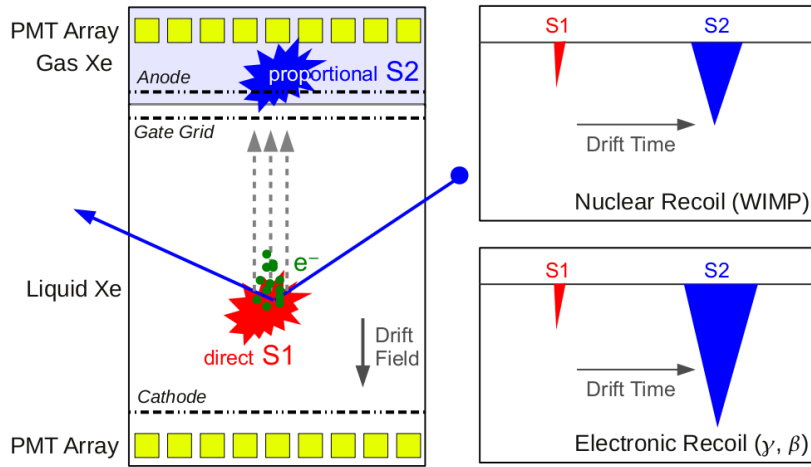
Figure 3.1: Schematic description of the detection principle in a double-phase xenon detector. Right figure illustrates how the energy partitions between ER and NR differ from each other.

The WIMP elastic scattering off xenon nuclei is expected to produce low energy NRs recoils with extremely low interaction rates (see Section 2.3). An ideal detector should therefore consist on a large target with low energy threshold, able to operate at ultra-low background conditions. Due to the low cross section of the interaction, it is virtually impossible that WIMPs interact more than once in the detector. Therefore via the S2 signal is it possible to identify and reject multiple scatter events for the dark matter search analysis.

3.2   THE XENON1T AND XENONnT DETECTORS

First WIMP search by the XENON Project was perfomed with the XENON10 experiment, featuring a target mass of 14 kg [21] and located at the Laboratori Nazionali del Gran Sasso (LNGS) in Italy. It was followed by the XENON100 experiment, with a target of 62 kg [22], operating stably since 2009 and under decommissioning at the time of writing. XENON100 published from 2010 to 2013 the most sensitive results on SI WIMP-nucleon scattering [23], later on confirmed and improved by the LUX experiment [24], also using a dual-phase LXe TPC. The SI

WIMP-nucleon scattering cross section reached by the XENON100 operation, in a combination of 477 live days, is $\sigma_{SI} = 1.1 \cdot 10^{-45}$ cm² for WIMP masses of 50 GeV/c² [25], with no evidence for dark matter.

The XENON1T experiment, also located at LNGS and currently taking data, is the first WIMP dark matter detector with a target mass above the ton-scale [26, 27]. An approximately cylindrical TPC of 96 cm length contains an active LXe target of 2.0 t, constained laterally by a structure of interlocking polytetrafluoroethylene (PTFE) panels. Two arrays 127 and 121 Hamamatsu R1410-21 VUV-sensitive PMTs are placed at top and bottom of the TPC, respectively, and the whole detector is encapsulated in a double-wall cryostat made of 5 mm thick stainless stell SS (see Figure 3.2(a)).

(a)   (b)
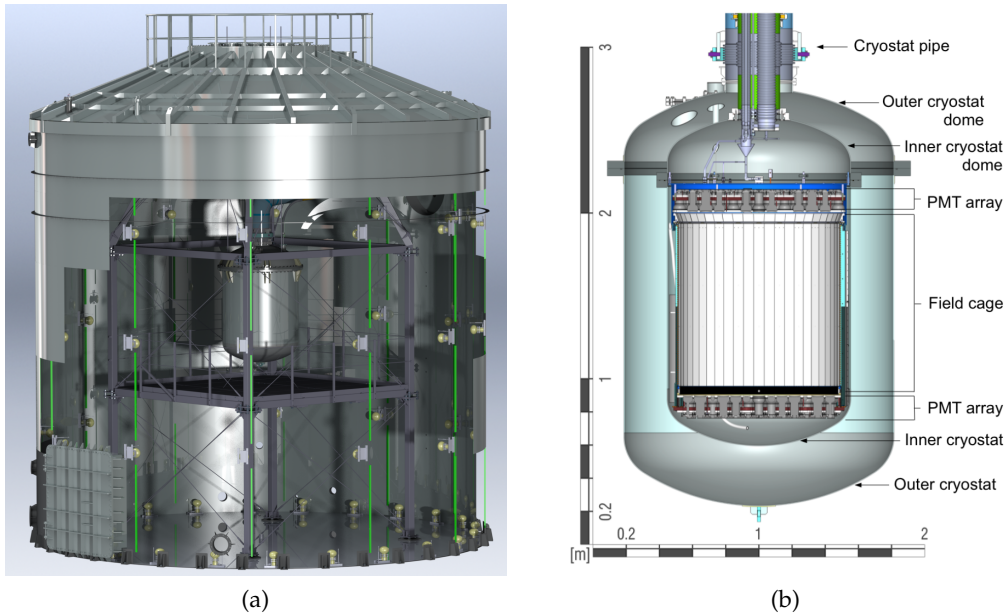
Figure 3.2: (a) Artistic view of the XENON1T outer cryostat inside the water tank. The PMTs of the muon veto system, the support structure and the main pipe connecting to the cryogenics room are also shown. (b) Section view of the XENON1T TPC with cryostat.

Its projected sensitivity is $\sigma_{SI} = 1.6 \cdot 10^{-47}$ cm², for SI WIMP-nucleon scattering. In order to reach it, background in XENON1T needs to be reduced by two orders of magnitude with respect to its predecessor. This is achieved by operating the detector inside a water tank equipped with PMTs and acting as a muon veto [28], like illustrated in Figure 3.2(b). Moreover, a dedicated radioassay of the detector components has been performed [29, 30] and a total amount of about 3.5 t of LXe is contained inside the cryostat, making use of the high density ($\rho = 2.827$ g/cm³) and γ-rays absorption properties of the material to reduce the background of the inner target (*fiducialization*).
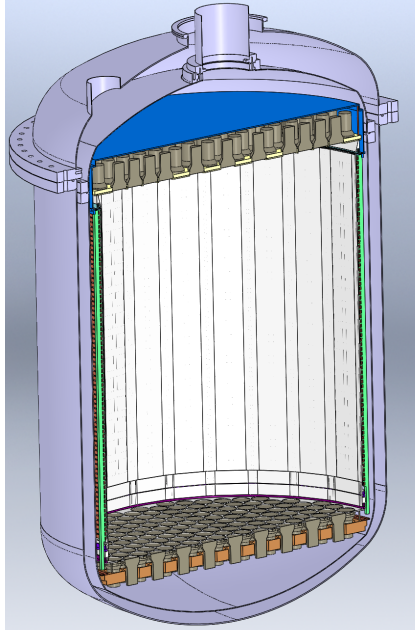
Figure 3.3: CAD view of the XENONnT TPC inside the cryostat. Optimized size of the inner cryostat with respect to XENON1T can be noticed, considering that for both cases the outer cryostat does not change.

Most of the infrastructure developed to host the XENON1T detector has been designed such that it can be used for an ungraded, larger phase of the experiment, after two years of XENON1T exposure. These components include the water tank, the Cherenkov muon veto, the outer cryostat, and the LXe storage and purification systems, among others. The design of the new larger TPC is completed (see Figure 3.3), while most of the needed components for its development are being built in parallel to the XENON1T dark matter search[1].

XENONnT is designed to achieve a factor of ~ 10 increase in the SI WIMP-nucleon scattering sensitivity with respect to its predecessor; and, while for an improved TPC self-fiducialization becomes more effective, in order to optimize the sensitive volume for dark matter search new studies on the different backgrounds need to be performed.

Dedicated studies on the ER and NR backgrounds in XENON1T [31] yield, for a fiducial volume (FV) of 1 t, a radiogenic NR background of $(0.6 \pm 0.1)\,(\text{t} \cdot \text{y})^{-1}$, considering the (4, 50) keV NR equivalent region of the dark matter search energy range. When compared to other channels of NR background, this source is the primordial one and with multi-ton scale its detection is now possible. Neutrons can produce NRs via elastic scattering off xenon nuclei and generate a signal indistinguishable from that of WIMPs in the detector. Moreover, fast neutrons can

---

1 Details on the up-to-date design of the TPC relevant in the scope of this thesis are given in Section 5.2.

penetrate inside the LXe, therefore their probability to hava a single scatter in the sensitive volume is higher than for γ-rays.

Based on the studies perfomed for XENON1T, this thesis aims for the characterization of the total radiogenic NR background in XENONnT, along with the conceptualization of an organic liquid scintillator neutron veto capable of effectively reducing the NR rate in the TPC FV. To set the framework of the developed outer detector characteristics, next chapter gives an overview on organic scintillator techniques.

4

ORGANIC LIQUID SCINTILLATORS

Scintillation detection makes use of the fact that the molecules of certain materials, when hit by a nuclear particle or radiation, absorb some of their kinetic energy and de-excite in the form of a flash of light, usually in the ultraviolet (UV) or visible range. Gadolinium-loaded linear alkylbenzene (LAB) has been chosen as the detector medium for the neutron veto implemented in this study. LAB is an organic LS solvent that has become very popular in the past years, mainly due to its superior safety features, good material compatibility and high transparency. In this chapter, some key properties of organic liquid scintillators are introduced.

4.1 SCINTILLATION MECHANISM

To understand how the conversion of energy into light works, one needs to look at the smallest relevant molecular substructure of an organic liquid scintillator, which consists of hydrocarbon molecules containing benzene-ring structures. A benzene ring (C_6H_6) is made up of hydrogen (valence electron configuration: $1s^1$) and carbon atoms ($1s^2 2s^2 2p^2$).

Sigma Bonds
sp^2 Hybridized orbitals

6 p_z orbitals

delocalized pi system
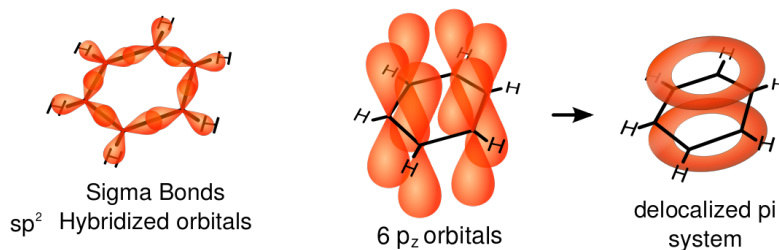
Figure 4.1: Illustration of the orbital structure of a benzene ring [32].

Each of the carbon atoms at the six corners of the ring has three bonds, one to the hydrogen atom and two to the neighboring carbon atoms. Since carbon in the ground state only has two valence electrons available for bonding, it needs to promote one of the 2s electrons into the 2p orbital, resulting in four unpaired electrons ($2s$, $2p_x$, $2p_y$ and $2p_z$). Atoms always strive for maximum bonding strength, which in the case of the benzene ring is achieved with three σ-bonds separated by 120°. These covalent bonds are shown in the left part of Figure 4.1. The *hybridization* process, by which the atom superimposes its orbitals to form the desired optical geometry, only affects the $2s$, $2p_x$, $2p_y$ orbitals in this case. When the main structure has been formed, the $2p_z$ orbitals arrange symmetrically with respect to the molecular plane, as illustrated in the center of Figure 4.1, and the so-called π-electrons associated combine to a single delocalized orbital (right part of Figure

4.1). In organic molecules containing benzene, luminescence is mainly caused by radiationless transitions from the excited states of these π-orbitals to the ground state. A Jabłoński diagram[1] illustrating these processes is shown in Figure 4.2.
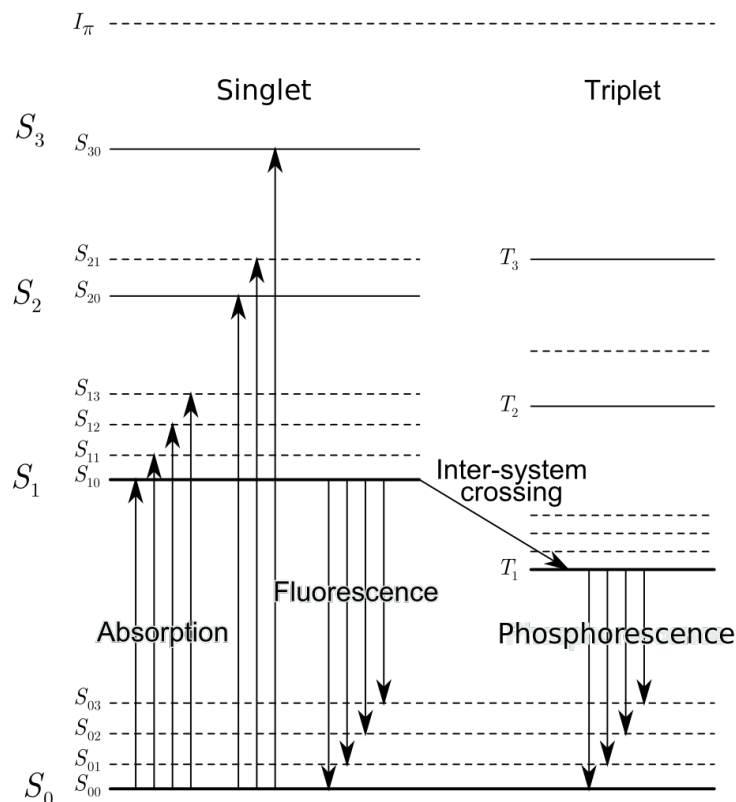
Figure 4.2: Electron energy levels in the π-system of an organic scintillator. S_0 is the ground state; S_1, S_2, S_3 are excited singlet states; T_1, T_2, T_3 are excited triplet states; S_{00}, S_{01}, S_{10}, S_{11}, etc. are vibrational sublevels and I is the ionization energy of the π-orbital [34].

The energy difference between electronic levels (S_0, S_1)...) is about 3-4 eV in organic scintillators, and typical spacing of the vibrational sublevels (S_{00}, S_{01}...) is of the order of 0.15 eV, a large value with respect to the average thermal energies (0.025 eV). This is the reason why nearly all molecules at room temperature are in the S_{00} state.

When some excitation energy brings the molecule from the ground state to some excited state S_i ($i \geqslant 1$), it rapidly dissipates its energy through collisions with neighboring molecules until it reaches the S_1 level. The time scale of these processes is in the order of 10^{-12}-10^{-11} s [34]. As shown in Figure 4.2, the principal scintillation light (fluorescence) is emitted in the transition from the S_{10} state to

---

1 Named after its creator [33].

one of the vibrational states of the ground electronic state to S_0 and follows an exponential decay

$$I(t) = I_0 e^{-\frac{t}{\tau}} \tag{4.1}$$

where the fluorescence decay time τ is a few nanoseconds [35]. On the other side, triplet states can be indirectly populated through a transition called *intersystem crossing* or by recombination of ionized molecules with electrons. The lifetime for the first triplet state is much longer than the lifetime of the first singlet state, therefore the light emission is delayed. Because T_1 lies below S_1, the emitted phosphorescence wavelength is longer than that of the fluorescence spectrum. In adition, delayed fluorescence can olso occur, when molecules are thermally excited back from the T_1 to the S_1, with the subsequent decay $S_1 \rightarrow S_0$.
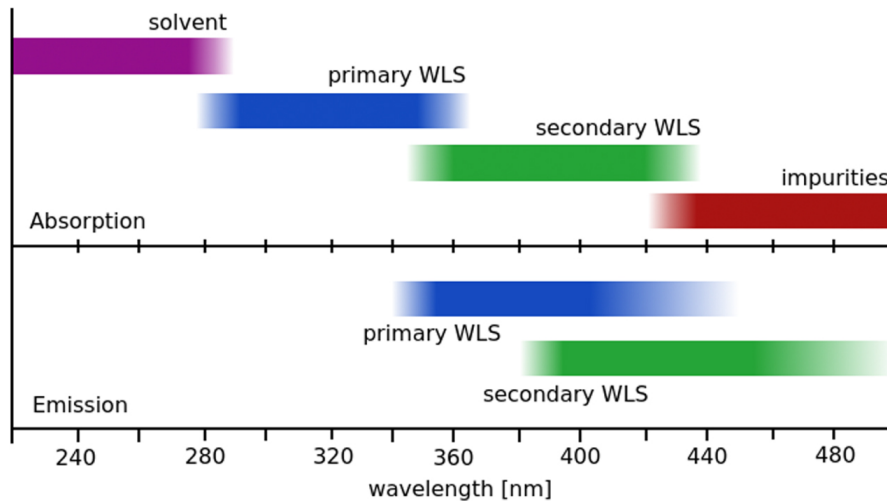
Figure 4.3: Absorption and emission wavelength ranges for each scintillator component [36].

In an organic liquid with just one aromatic solvent molecule most of the fluorescence radiation is self-absorbed after a short distance, due to the overlap between its absorption and its emission spectra[2]. To effectively detect scintillation photons in an organic liquid system, a second (and even a third) organic component must be added, called *fluor* or *wavelength shifter* (WLS). Energy transfer from the solvent to the fluors is mainly radiationless. Figure 4.3 shows, for a ternary LS system, the regions for which the absorbance for every component is dominating in the liquid, as well as the typical ranges of emission for both fluors. In the optical region above 430 nm, self-absorption of the mixture due to chemical impurities becomes dominant, overlapping with the emission spectra of the secondary fluor. Reducing this contamination is therefore a key step in the developement of such systems.

---

2 This is different for scintillator detectors using liquid noble gases. As described in Section 3.1, scintillation light in LXe is produced via the formation of excited dimers, where the excitation levels do not correspond to the levels of the single atoms in the noble gas. Losses due to self-absorption are therefore reduced in this case.

4.2   LIGHT YIELD AND PROPAGATION

An important characteristic of a scintillator is its light yield (LY), directly linked to the energy resolution of the detector. In Figure 4.4, the LY for two different scintillator solvents is given as a function of the primary WLS proportion. The shift in the emission spectra induced by the fluor increases the yield up to a saturation point, in which it starts to fall off due to *self-quenching*, an effect related to interactions between unexcited and excited fluor molecules in which the excitation energy can be lost by collision.
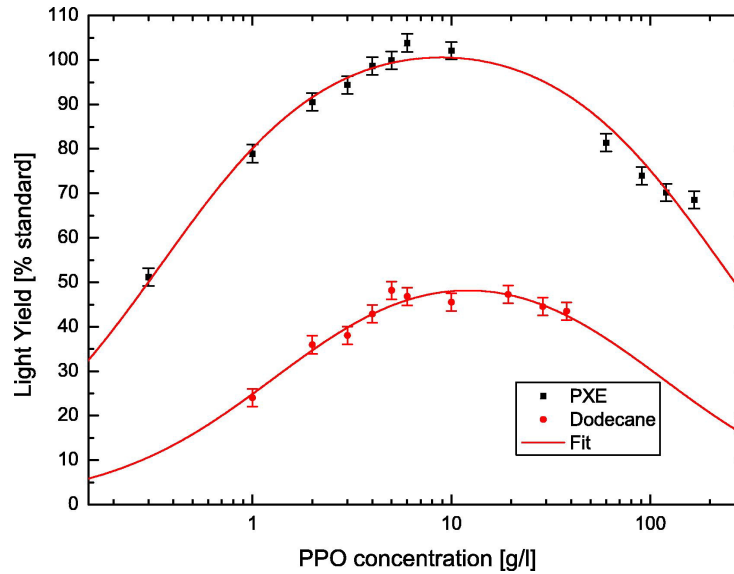
Figure 4.4: Light yield for PXE- and dodecane-based scintillators as a function of the primary fluor PPO concentration [37].

The amount of light emitted by a scintillating material is not strictly proportional to the energy deposited by the ionizing particle. These losses of linearity in the scintillation reponse are called *quenching* and can be particle and energy dependent. The most prominent form of this effect is known as *ionization quenching* and happens when an ionizing particle travels through a scintillator ionizing the molecules in its path. These ionized particles are considered as 'damaged' and do not participate in the fluorescence process, although there can be light emission when the molecular ion recombines with an electron. Quenching effect is high for large energy deposition per unit length, characteristic of slow electrons or heavier particles in general.

The semi-empirical Birks' law is commonly used for a phenomenological parameterization of the energy deposition per unit length dE/dx as a function of the ionization density [38],

$$L(E) = L_0 \cdot \int_0^E \frac{dE}{1 + kB \cdot \frac{dE}{dx}} \tag{4.2}$$

where $L(E)$ is the light output produced within a distance dx, L_0 is the LY constant and kB denotes the Birks' quenching parameter, which varies for different particles and scintillator materials. For fast electrons, in which the coefficient dE/dx is very small, Equation (4.2) approximates to

$$L_e(E) \approx L_0 \cdot E \ . \tag{4.3}$$

Besides the quenching effect, which affects the energy deposition directly available for light production, some other interference processes occur as the generated light travels through the scintillator, also relevant to characterize the detector response. Two interactions of the traveling photon must be taken into account: *absorption* and *scattering*, both of them dependent on the emitted wavelength. Whereas absorption takes place when the energy of the photon is transformed into heat during the interaction (and thus lost for signal detection), scattered light changes its propagation direction and/or energy and can still be detected in a large-scale scintillator.

Considering the propagation of a one-dimensional beam, the intensity of the light travelling can be written as

$$I(x) = I_0 \cdot e^{-\frac{x}{\lambda_{abs}}} \cdot e^{-\frac{x}{\lambda_{sct}}} = I_0 \cdot e^{-\frac{x}{\lambda_{att}}} \tag{4.4}$$

where I_0 corresponds to the original intensity and λ_{abs} and λ_{sct} are the absorption and scattering lengths of the scintillator, respectively. The combination of both processes is the *attenuation* effect, and the relation

$$\frac{1}{\lambda_{att}} = \frac{1}{\lambda_{abs}} + \frac{1}{\lambda_{sct}} \tag{4.5}$$

defines the associated attenuation length λ_{att}, which also accounts for chemical impurities of the scintillating mixture and ultimately determines its transparency.

4.3 METAL LOADING AND NEUTRON DETECTION

In the scope of this study, research on different metal loading options has been carried out, benefiting from the knowledge aquired in already operative experiments. This investigation led to the comparison between gadolinium-loaded (Gd-LS) and boron-loaded liquid scintillator (B-LS) as detector materials for the simulated XENOnT neutron veto (see Chapter 5).

Organic LS has been the preferred detection medium for neutrinos since they were measured by Reines and Cowan [39], who searched for interactions in a cadmium-loaded LS. For the delayed neutron capture signal, the advantages of adding a metallic element are significant[3], with the associated challenge of reach-

---

3 In, e. g., the Daya Bay reactor experiment [40], antineutrinos are detected via the inverse β decay reaction in the scintillator, $\overline{\nu}_e + p \rightarrow n + e^+$, in a delayed coincidence between the prompt signal of the positron and the following neutron capture on hydrogen ($\tau \sim 200\,\mu$s). By enhancing their LS with 0.1 % of gadolinium by weight, the neutron capture time is shortened to $\sim 28\,\mu$s, reducing the accidental background rate by a factor of seven.

ing the desired solubility without degradating the optical properties of the liquid. Moreover, the mixture has to be optically and chemically stable over the timescales for neutrino searches, in the order of several years, and has to meet the radiopurity requirements fur such experiments.

The aimed outer detector must have a size allowing for the moderation or *thermalization* of the neutrons via elastic scatterings on H or C, before its capture. These scatterings result in a prompt light signal in the order of ns which can already be used for veto purposes. After a diffusion time of few μs, the neutrons reach room temperature energies and can be captured on a nucleus ^{A}X via an excited compound ($^{A+1}X^{*}$) or direct capture. In the case of boron and gadolinium, the capture results in the transmutation of the nucleus and the subsequent decay via the emission of photons and/or charged particles. Thermal neutron capture cross sections and corresponding binding energies for gadolinium and boron are given in Table 4.1, along with the information for the most relevant isotopes of an undoped organic LS.

Isotope	Natural abundance [%]	σ_{capture} [b]	S_{n} [keV]
^{1}H	99.9885(70)	$3.326(7) \cdot 10^{-1}$	2224.576(19)
^{2}H	0.0115(70)	$4.92(25) \cdot 10^{-4}$	6257.2482(24)
^{12}C	98.93(8)	$3.89(6) \cdot 10^{-3}$	4946.311(3)
^{13}C	1.07(8)	$1.22(6) \cdot 10^{-3}$	8176.61(18)
^{10}B	19.9(7)	$3.820(135) \cdot 10^{3}$	11454.15(14)
^{11}B	80.1(7)	$6(3) \cdot 10^{-3}$	3370.4(14)
^{152}Gd	0.20(1)	$7.35(20) \cdot 10^{2}$	6247.48(17)
^{154}Gd	2.18(3)	85(12)	6435.29(19)
^{155}Gd	14.80(12)	$5.17(18) \cdot 10^{4}$	8536.04(9)
^{156}Gd	20.47(9)	1.8(7)	6360.05(15)
^{157}Gd	15.65(2)	$2.15(5) \cdot 10^{5}$	7937.39(5)
^{158}Gd	24.84(7)	2.2(2)	5943.29(15)
^{160}Gd	21.86(19)	1.4(3)	5635.4(10)

Table 4.1: Neutron capture cross section, natural abundance and neutron binding energy for the nuclei of Gd- and B-doped LS. Data extracted from [41].

^{10}B, with a natural abundance of about 20 %, captures thermal neutrons with a very high cross section via one of the two channels [42]:

$$
\begin{aligned}
^{10}\text{B} + \text{n} \;\rightarrow\; & ^{7}\text{Li}^{*} + \alpha \;(1471\,\text{keV}) && (\text{BR } 93.7\,\%) \\
& ^{7}\text{Li}^{*} \rightarrow\; ^{7}\text{Li} \;(839\,\text{keV}) + \gamma \;(478\,\text{keV}) && (4.6) \\
\rightarrow\; & ^{7}\text{Li} \;(1015\,\text{keV}) + \alpha \;(1775\,\text{keV}) && (\text{BR } 6.4\,\%)
\end{aligned}
$$
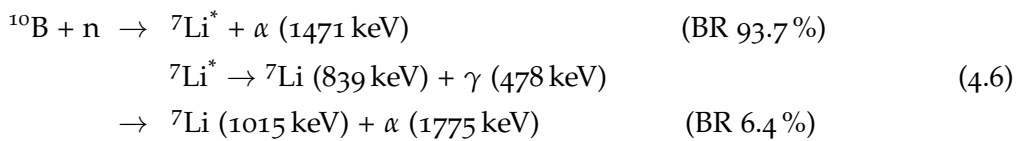
The second of which provides a significantly smaller signal, since there is no γ emission and the recoils from the α and the ^{7}Li nucleus are heavily quenched in the scintillator. On the other hand, the capture cross sections in ^{155}Gd and ^{157}Gd are among the highest nuclear cross sections found in any material. The process follows the reaction

$$^A\text{Gd} + \text{n} \; \rightarrow \; ^{A+1}\text{Gd} + \gamma\text{'s (7-8 MeV)} \tag{4.7}$$

in a cascade of three to four γ-rays in most of the cases, besides the emission of conversion electrons in 39 % of the capture reactions [35].

A comparative advantage of B-LS is that, although it generates less energetic deposits, the extremely short mean free path of the nuclei following the neutron capture ensures that they almost never escape the detector, while γ-rays may escape the veto without leaving any detectable signal. This means that a B-LS detector with an effective threshold low enough to reliably detect α particles can perform at efficiencies of almost 100% [43]. The direct advantage of this feature is the possibility of building a highly efficient neutron veto with a relatively small size; whereas, to set such a threshold, very challenging requirements must be fulfilled regarding the PMT coverage and the radiopurity of the scintillating mixture. A B-LS neutron veto for direct WIMP searches has already been developed by the DarkSide-50 experiment located at LNGS, with a reported PE yield of 0.54 $\pm$ 0.04 PE/keV [44]. In this case, radiopurity requirements of the undoped solvent meet those of the Borexino neutrino experiment, thanks to a shared fluid handling plant, and the high photocoverage is achieved through a spherical design of the vessel hosting the B-LS, which contains dedicated veto PMTs and is internally covered with a reflector foil operative in the LS environment.

Since the product of a neutron capture on Gd is a γ cascade (and sometimes a conversion electron), the quenching effect is significantly reduced with respect to the capture on B and therefore light coverage requirements become more flexible for this loading option. Furthermore, the high cross section of some of the Gd isotopes ensures a large fraction of captures on Gd, even with a scintillating mixture with reduced metal content. This allows for the synthesis of an efficient doped organic scintillator able to preserve the chemical stability and the transparency of the bulk solvent. Given the ~ 8 MeV energy spectrum of the capture on Gd, discrimination against environmental γ-rays[4] also becomes more efficient for this loading option, even if under the assumption of not confining all the products from the cascade in the Gd-LS container. Recent reactor neutrino experiments have demonstrated that Gd-LS with LAB as a solvent can be used under stable conditions even after five years of LS production and beyond [36].

In the field of dark matter searches there are also examples of the use of Gd as a vetoing material against NR background. The multi-ton LXe TPC experiment LZ,

---

4 The most dangerous source of naturally occuring gamma background is of about 2.6 MeV and corresponds to ^{208}Tl decay, in the lower part of the thorium chain.

currently under construction, plans to use a neutron veto based on Gd-LS consisting on multiple transparent vessels; where, unlike in the DarkSide-50 approach, the scintillating mixture is neither in contact with the outer detector cryostat, nor with the dedicated veto PMTs [45].

SIMULATIONS OF A NEUTRON VETO

Considering the geometry of the XENON1T detector, along with the need for a relatively rapid upgrade to XENONnT, this study now focuses on designing a simulation of a practical neutron veto for the future operation in the experiment.

This implemented neutron veto is based on Gd-LS. As illustrated in the previous chapter, the major advantage of this loading option is, given the higher capture cross section and energy yield with reduced quenching, the non-necessity of a full solid angle photosensor coverage. This gives the opportunity of reusing the water PMTs dedicated for the muon veto, which are already installed and operative. The main disadvantage to B-LS, i.e. the actual possibility that some γ-ray products escape the outer detector, has a minor impact on the results of this study[1]. The conceptualization of the simulated XENONnT neutron veto mixture has followed the information on currently operative neutrino experiments employing Gd-LS with LAB as a solvent, like, e. g., Daya Bay [46] and RENO [47].

The studies which constitute the bulk of this thesis have been carried out using GEANT4 (*GEometry And Tracking*) version 9.5-patch01, a toolkit to simulate the passage of particles through matter with help of Monte Carlo (MC) methods [48]. Components of the framework relevant in the scope of this work are summarized in the next section. In the following sections, the changes and additions performed on the XENONnT MC code are briefly described, as well as the creation, properties and tracking of the particles generated in order to evaluate the neutron veto capabilities of the implemented outer detector.

5.1 THE GEANT4 FRAMEWORK

GEANT4 is a C++ based object-oriented framework, the classes of which are designed to create stand-alone simulations. This package provides a set of methods to generate geometrical structures and define the properties of all the involved materials, as well as the option to use many, sometimes competing, physical interaction models to simulate the creation and tracking of all fundamental particles in a wide energy range. To illustrate the working structure of a program designed with GEANT4, some implementation details are discussed here.

A *run* in GEANT4 represents one simulation procedure with a specified number of identical or different *events*, where a single event contains all the physical processes that an initial particle and its subsequent secondaries undergo. A *track* is always a momentary representation of the state of a particle, while a *step* car-

---

1 As will be shown in Section 6.1, for a large set of simulated statistics.

ries the key information between two track points.

There are interfaces for eight user classes provided by the framework, three of which are mandatory:

- G4VUserDetectorConstruction: In a derivation of this class the user has to provide information about the geometry of the detector that shall be simulated, including details about the chemical composition and the optical properties. A specific volume can be declared as a *SensitiveDetector* in order to create *hits*, or collections of the particle properties at every track.

- G4VPhysicsList: Here the user defines the physics process classes to be used. Relevant processes can be activated and also production cuts can be set to decide whether a secondary particle, e.g., an optical photon, shall be generated or not.

- G4VUserPrimaryGeneratorAction: The user has to set the number and the starting properties of the primary particles, such as position, direction, momentum, type and charge.

Classes that are not mandatory but necessary to perform the simulations are:

- G4UserRunAction: Here the user can specify actions that shall be executed at the start and the end of every run.

- G4UserEventAction: Same function as the G4UserRunAction class, this time for every event.

- G4UserStackingAction: Mainly used for optimisation, this class offers the possibility to suspend or postpone tracks with low priority, e.g., long-living generated isotopes of no relevance in the study.

- G4UserTrackingAction: Specifies actions at the creation and completition of every *track*.

- G4UserSteppingAction: Customises the behavior while going through the different steps in the simulation. Detailed information from every interaction can be obtained here, as an alternative for (or in combination with) the SensitiveDetector.

Besides some other features that GEANT4 offers, such as the three-dimensional visualization of the implemented geometry or interactions, there is also the possibility to call for the initialization of a *geantino*, a virtual particle which does not interact with materials and only undertakes transportation processes, what makes the corresponding runs very 'light' in terms of computing power. Moreover, by confining their generation whithin a preset volume (as can be done for every particle), it it possible to browse through details in the detector geometry and precisely determine distances between volumes. They have been used in this work to illustrate the simulated veto PMTs geometry.

5.2 DETECTOR IMPLEMENTATION

At the completition of this thesis, the design of the XENONnT TPC was finalized [49] and most of the needed components for its development have been ordered or are already available for construction, as indicated in Section 3.2. One of the main tasks of this study has been to update and test this final design in GEANT4. Some of the implemented details are:

TPC diameter [i]	$\sim 1368\,$mm
TPC drift length	$1446\,$mm
Target mass	$5.983\,$t
PMTs	476 (223 top and 253 bottom)

[i] Structure does not exactly form a a cylinder, but a polygon.

Table 5.1: Details on the XENONnT TPC implemented.

Other pertinent inputs regard the mass/quantity of all the relevant materials in the performed NR background simulations. The total masses have been rescaled with respect to XENON1T. These results are also cross-checked by computing the mass from the detector CAD files and from GEANT4, since the density of every material has been defined in the code. A complete relation of simulated materials and their quantity is given in Section 5.4.

5.2.1 *Neutron veto geometry*

The designed layout of the neutron veto containing the Gd-LS consists of seven acrylic vessels. Four side vessels conform a segmented cylinder around the outer cryostat and two other vessels enclose the cylindrical outer detector on top, allowing for the penetration of the main pipe connected to the cryostat. An additional cylindrical bottom vessel completes the full structure, this last one also containing a feedthrough aimed for the operation of the anti-buoyancy system attaching the outer cryostat to the bottom of the water tank. The position of the simulated vessels inside the detector water tank is shown in Figure 5.1, where the support structure, the door of the tank and the main pipe are also shown for reference.

Acrylic vessels are the preferred option for scintillator containers in the reviewed references for the veto design. Their main advantages are a high UV transparency and an excellent compatibility with LAB. To ensure pressure stability between them and the surrounding water volume [50], they have been designed with a conservative width of 2.54 cm (1 ") in all their walls, except for the lateral ones in the side vessels, where it is halved (such that the acrylic interface between the vessels is also 2.54 cm). Positioning of the veto is made with a positive offset of 34 mm along the vertical axis with respect to the TPC placement, in order to avoid overlaps between the upper vessels and the flanges on top of the cryostat,

(a)   (b)
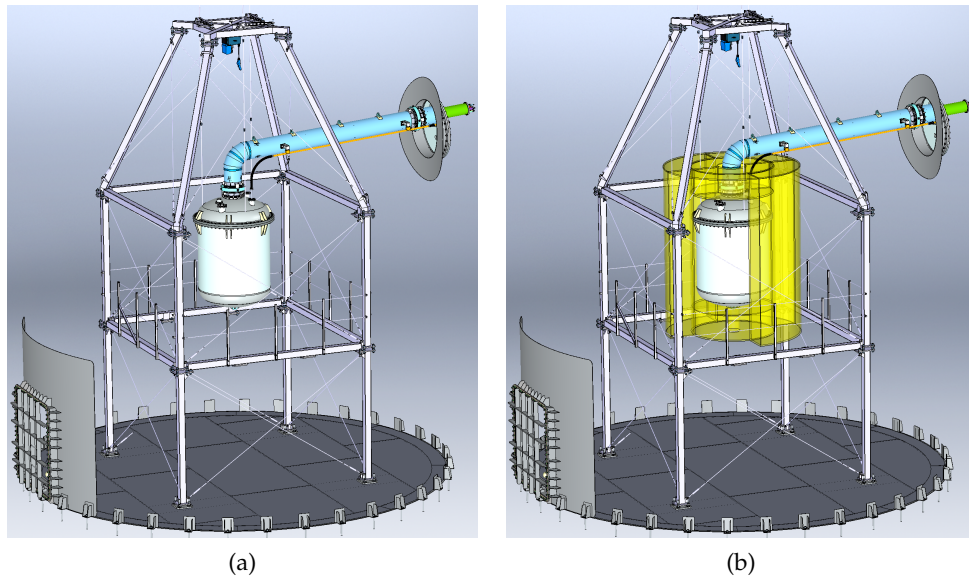
Figure 5.1: XENON1T/nT water tank (a) as it is now and (b) with the neutron veto vessels. For a better view, a lateral vessel and one of the horizontal bars from the support structure are also suppressed. The main pipe coming from the cryogenics room overlaps with the upper vessels if their thickness is greater than 721 mm.
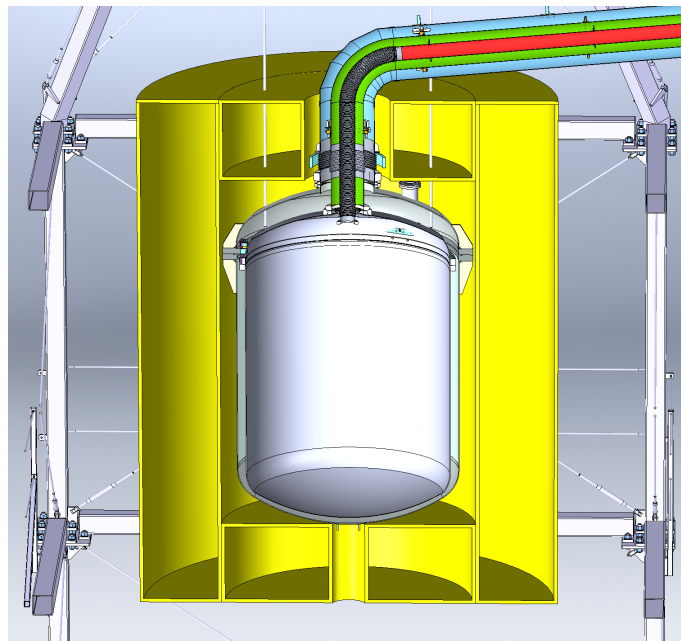
Figure 5.2: Cut view of the outer detector vessels and the XENONnT cryostat. The design corresponds to a thickness of the top, bottom and side vessels equal to 60 cm, with a distance of 1 cm between the outer flange and the side vessels. The insides of the inner cryostat are not drawn (see Figure 3.3 for details on the XENONnT TPC).

as shown in Figure 5.2.

Four different vessel total thicknesses have been tested, ranging from 30 to 60 cm (including the width of the acrylic walls), determined by the γ scattering length (~ 25 cm) and the mechanical constraints of the already existing structure. For example, Figure 5.3 shows how a 120°-segmented cylinder for the considered veto inner radius and 60 cm thick would fit through the water tank door (drawn in Figure 5.1), only allowing for a few cm of operation. It has therefore been decided to use 90°-segmented side vessels, also for thicknesses smaller than 60 cm. The resulting mass of the filled and unfilled vessels is shown in Table 5.2 for these four cases.

Veto thickness [cm]	LS mass [t]	Acrylic mass [t]	Total mass [t]
30	5.49	1.90	7.39
40	8.40	2.18	10.58
50	11.79	2.48	14.27
60	15.66	2.80	18.46

Table 5.2: Total mass of the seven outer detector acrylic vessels, assuming a LS density equal to that of LAB. *Veto thickness* reads for a same thickness of the top, bottom and side vessels. Displacer mass not accounted.
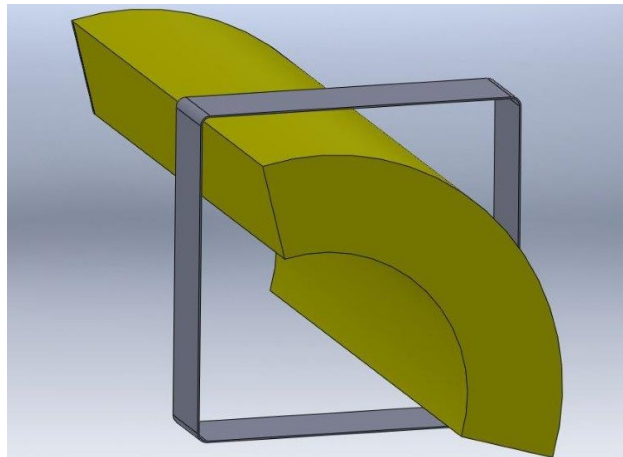
Figure 5.3: View of the passage of a 60 cm 120°-section side vessel through the door of the XENON1T water tank.

In order to achieve a conceptually hermetic outer detector, the buffer between the outer cryostat and the veto containers (~ 3.5 m^3 including the connection feedthroughs), has been filled with closed-cell polyurethane ($C_{25}H_{42}N_2O_6$) foam. For comparison, studies have been also performed with water as *displacer* material (see Chapter 6), being concluded that this choice has a non-negligible impact

on the veto performance.

For the operation of the LS volume as a sensitive detector in the simulations (together with the LXe), dedicated GEANT4 classes have been created. Every track in a sensitive detector is recorded in the simulation output tree, hence for a single event variables such as the energy deposit and the position of every interaction are recorded and correlations between the sensitive volume of the TPC and the neutron veto can be established.

5.2.2 *Scintillating mixture*

LAB has been chosen as the solvent for the Gd-LS mixture, with a proportion of 3 g/l of 2,5-diphenyloxazole (PPO) as a primary WLS and 15 mg/l of 1,4-bis(2-methylstyryl)benzol (bis-MSB) as the secondary one, mimicking the exact concentrations from the already operative experiments referenced at the beginning of this chapter[2].

The emission maximum of LAB, at ~ 283 nm, is whithin the absorption range of PPO, which extends up to ~ 303 nm. Likewise, the absorption range of bis-MSB overlaps with PPOs emission (with its maximum at ~ 365 nm) and has its maximum emission peak at ~ 430 nm, far from the absorption ranges of LAB and PPO.

(a) LAB ($C_6H_5C_nH_{2n+1}$, typically n = 10 - 13)

(b) PPO ($C_{15}H_{11}NO$)

(c) bis-MSB ($C_{24}H_{22}$)
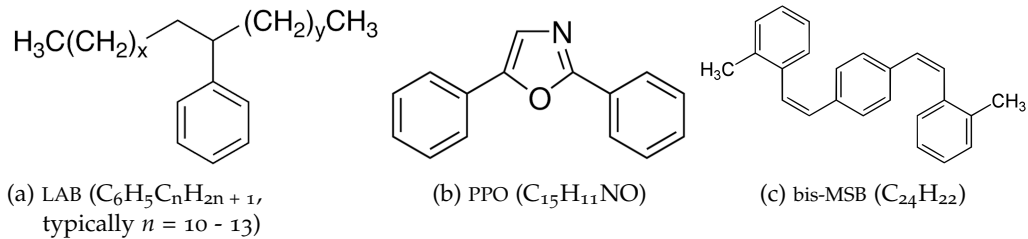
Figure 5.4: Structural formulas for the organic components of the implemented LS mixture.

For simulation purposes, the impact of the fluors (especially bis-MSB) on the total LS mass is negligible. The undoped mixture has been defined following the GEANT4 procedures, i.e. providing the density, the number of materials with the corresponding massic proportion and the state of the compound in natural conditions. The density of the mixture has been defined as that of raw LAB (0.863 g/cm³) and the proportion by mass of the different components as 99.654 % of LAB and 0.346 % of PPO, which corresponds to the above stated 3 g/l. The fact of not adding the secondary WLS does not shift the fluorescence spectrum, since in GEANT4 this is defined when activating the scintillation of the material[3], such

---

2 References [51] and [52] provide with more detailed information on the emission and absorption properties of ternary LS systems using these two fluors.

3 Included in the `G4OpticalPhysics` physics list.

that the emission spectrum of bis-MSB can be set as the one for the total compound.

Gadolinium is not found as a free element in nature, but it is contained in many rare minerals. It reacts slowly with water and dissolves in acids, and can form stable organometallic complexes. The main challenge when adding an inorganic salt to organic LS is to find the appropiate ligand to ensure a good and stable binding[4]. As reported by the Daya Bay and RENO experiments among others, 3,5,5-trimethylhexansaeure (TMHA) is a very favoured candidate to enhance LAB with Gd, with proven stability of the doped mixture for several years. The synthesis, making use of a solution of $GdCl_3$[5], proceeds as [53]:

$$RCOOH + NH_3 \cdot H_2O \rightarrow RCOONH_4 + H_2O \tag{5.1}$$

$$3RCOONH_4 \text{ (aq.) } + GdCl_3 \text{ (aq.) } \rightarrow Gd(RCOO)_3 + 3NH_4Cl \tag{5.2}$$
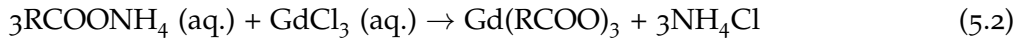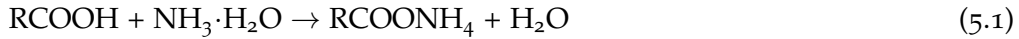
where the $Gd(RCOO)_3$ precipitate (so-called *Gd-TMHA*) is the complex to be mixed with LAB, implemented in GEANT4 and added to the undoped mixture in the following massic proportions:

LS (LAB + fluors) [%]	Gd-TMHA [%]	Resulting Gd [%]
99.6006	0.3994	0.1
99.2011	0.7989	0.2
98.4023	1.5977	0.4
96.8046	3.1954	0.8

Table 5.3: Simulated proportions of Gd-TMHA in the LS and resulting Gd fraction.

The baseline mixture in this study is the one corresponding to a Gd concentration of 0.1 % by weight. Likewise, the thickness of the vessels is assumed to be 60 cm and the buffer between cryostat and acrylic vessels (see Figure 5.2) to be filled with closed-cell foam ($\rho \sim 0.04\,g/cm^3$). The performance of a hypotetical Gd-LS with higher metal content (or no Gd at all) is also evaluated, in order to set some conclusions on whether it is worthwhile to aim for this or even a more complex mixture. At 0.1 % concentration by weight, capture on Gd is already about one order of magnitude more probable than on H, given the exceptionally large capture cross section of the ^{155}Gd and ^{157}Gd isotopes.

In the detector class created in GEANT4, a variation of Birks' semi-empirical law (Equation (4.2)) has been implemented for every particle track,

$$\Delta E_{quenched} = \frac{\Delta E}{1 + kB \cdot \frac{\Delta E}{\Delta x}} \tag{5.3}$$

---

4 See [36] for an extended up-to-date review on the different techniques for LS metal loading.
5 This solution can be either directly purchased or synthesized in the laboratory from Gd_2O_3, a much cheaper product.

where ΔE is the recorded energy for a track of length Δx and $\Delta E_{quenched}$ corresponds to the real deposit after accounting for the quenching effect. kB in LAB and 0.1 % Gd-LS[6] for electrons is taken from [47]. Protons and alpha particles are treated separately and their Birks' constant is taken from [54] and [55], respectively. For higher Gd contents the quenching factors for 0.1 % Gd-LS have been fixed, although the reasonable expectation is for the quenching effect to be slightly stronger, due to the increasing opacity induced in the liquid. Since the change from LAB to Gd-LS is already minor and some other conservative constraints are applied when evaluating the energy deposit for veto events (Section 6.3), these approximations are considered as valid.

5.2.3 *Photomultiplier tubes*

To complete the conceptual design of the neutron veto, some extra PMTs (yet without a defined support structure) have been implemented inside the water volume. They complement the 84 already existing, placed at the edges of the tank and dedicated to the XENON1T muon veto [28]. The use of Gd-LS ensures that some of the capture signals will reach these edges, although more photosensors might be needed closer to the detector, in order to set a reliable threshold above natural contamination. The type of PMT simulated is exactly that of the muon veto: the high quantum efficiency (QE) 8 ″ Hamamatsu R5912 model, which includes a water-proof enclosure [56] and is already succesfully operating in the XENON1T muon veto.
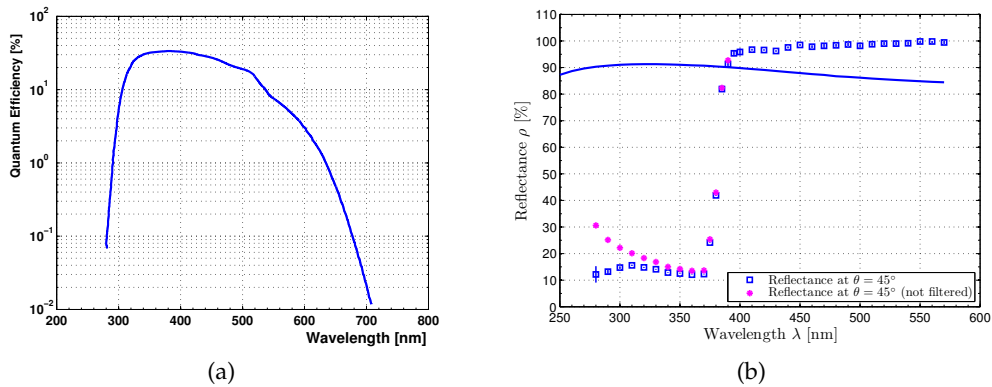
Figure 5.5: (a) QE of the Hamamatsu R5912 PMTs. QE is about 30 % averaged over the bis-MSB emission spectrum [56]. (b) Reflectance curve of the DF2000MA foil measured for an angle of incidence of 45°, as provided by the manufacturer of the reflectance standard used for comparison (blue line). Purple dots and an indication of the WLS capabilities of the foil for this region (which have not been implemented in the code). Details on this measurement can be found in [57, 58].

---

6 In the following, the number prior to the mixture defines the percentage by weight of the metal.

In addition, the acrylic surfaces in contact with the displacer or the water volumes, except for the ones facing the PMTs, have been defined as cladded with the DF2000MA daylighting film [59]. This foil is already present on the inner walls of the water tank and its full reflectance curve, shown in Figure 5.6(b), has been implemented in GEANT4 for the case.

5.3   OPTICAL PHOTON SIMULATIONS

The understanding of the photoelectron (PE) yield of the veto has been done through a two-step process, deriving separately the light collection efficiency (LCE) and the energy deposition maps, for the posterior merging during the analysis (see Chapter 6.2.1). It has been verified that the impact of evaluating the time of energy deposit in LS instead of the one for light detection in the veto PMTs is minor. The time to record enough energy to veto a background event is in the order of $100\,\mu$s, hence at least three orders of magnitude larger than that of the produced optical photons to travel through the outer detector and reach the PMT photocathode.

Based on that, scintillation has been deactivated for the neutron simulations[7]. The amount of statistics initilized in every run, in combination with the different tested configurations, make computing time prohibitive when activating optical processes.

Different arrangements of the added veto PMTs have been tested with the goal of enhancing the photocoverage of the outer detector, but only on the sides of the vessels, considering that the XENON1T support structure will remain for XENONnT. After some preliminary verifications, the chosen configuration corresponds to an array of veto PMTs in twelve columns, covering a vertical distance of an 85 % of the total lentgh of the veto along the vertical axis (adapting the spacing between PMT rows accordingly for every case).

The configurations explored for the LCE simulations are the combination of the four defined thicknesses of the veto vessels (30 to 60 cm), the addition of 0, 72, 96 or 120 PMTs along with the existing muon veto ones, and the distances for this new cylindrical PMT array of 60, 70 or 80 cm to the outer acrylic walls.

In Figure 5.6, obtained by generating geantinos from the represented volumes in GEANT4, the xy placement of the muon veto PMTs in the tank is shown (light blue), along with a planar section of the LS (green) and the acrylic vessels (red) at around $z = 0$ (center of the TPC). The position of an extra veto PMT array (dark blue) 60 cm away from the veto vessels is also shown as an example.

---

7 By deactivating the scintillation, the code only forbids the generation and track of the optical photons, but the ionization processes leading to the production of these photons are still recorded along with their corresponding energy deposit.
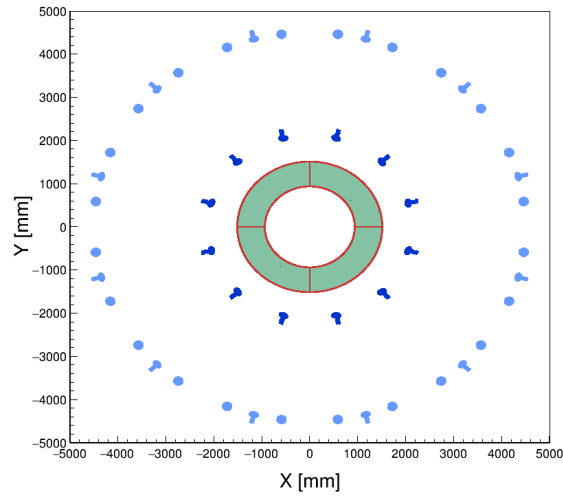
Figure 5.6: Planar view of the *xy* position of the simulated acrylic vessels and water PMTs in GEANT4.

For all the cases 10^7 optical photons have been simulated, following the energy distribution of the fluorescence emission curve of bis-MSB after 1 cm of propagation through the ternary liquid system, represented in Figure 5.7.
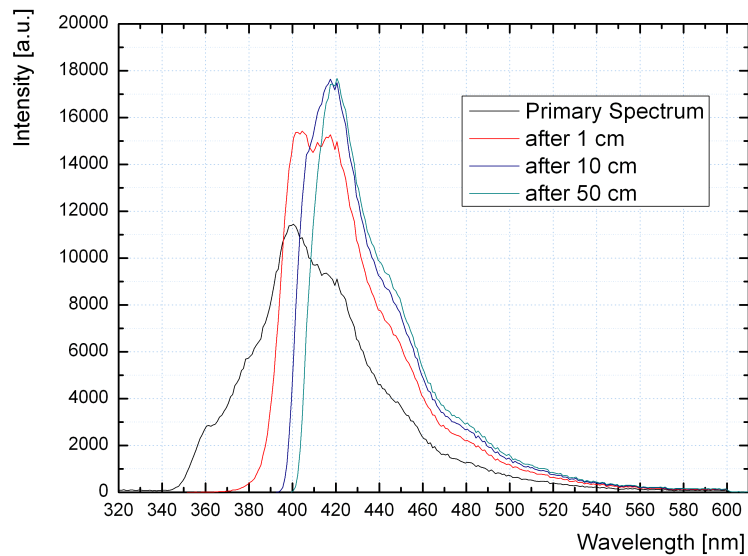
Figure 5.7: Differential emission spectra for LS enhanced with PPO and bis-MSB. In the primary spectrum (after non-radiative energy transfer) part of the emission still corresponds to that of PPO, while after 1 cm propagation through liquid the one of bis-MSB is already dominant, and almost exclusive after 10 cm. In this work, the 1 cm curve has conservatively been set as the simulated spectrum over the whole LS volume. Data extracted from [60].

To enable the various processes that the optical photons can undergo one needs to assign values for the absorption length, the Rayleigh scattering length and the refractive index of all the involved materials at different wavelengths. Since the code adapted in this work has been used to study the existing muon veto system, the water properties are already well defined. For the acrylic, optical properties values from [61] have been taken, as well as for the refractive index for Gd-LS.

Regarding the light propagation in Gd-LS, experiments like Daya Bay have reported the attenuation length for the LS to only suffer a slight decrease after the addition of Gd, resulting in values of ~ 15 m at 430 nm and with an observed slow degradation (~ 1.3 % per year) in the PE yield [62]. Recent improvements on purification techniques can allow for values $\geqslant 20$ m, e.g., as indicated in the JUNO experiment technical report [63] for undoped LS with the same fluor concentrations as Daya Bay. For the simulated Gd-LS, an attenuation length of 14.5 m has been implemented, corresponding to (see Equation (4.5)) absorption and scattering lengths of 30 m and 27 m, respectively.

Component	Material	Quantity	Unit	Contamination [mBq/unit]				
				^{238}U	^{235}U	^{226}Ra	^{232}Th	^{228}Th
Cryostat shells	SS	1060	kg	2.4 (7)	1.1 (3) $\cdot$ 10^{-1}	< 6.4 $\cdot$ 10^{-1}	2.1 (6) $\cdot$ 10^{-1}	< 3.6 $\cdot$ 10^{-1}
Cryostat flanges	SS	540	kg	1.4 (4)	6 (2) $\cdot$ 10^{-2}	< 4.0	2.1 (6) $\cdot$ 10^{-1}	4.5 (6)
TPC panels [i]	PTFE	170	kg	< 2.5 $\cdot$ 10^{-1}	< 1.1 $\cdot$ 10^{-2}	< 1.2 $\cdot$ 10^{-1}	< 4.1 $\cdot$ 10^{-2}	< 6.5 $\cdot$ 10^{-2}
TPC plates	Cu	448	kg	< 1.2	< 5.5 $\cdot$ 10^{-1}	< 3.3 $\cdot$ 10^{-2}	< 4.3 $\cdot$ 10^{-2}	< 3.4 $\cdot$ 10^{-2}
PMT stem	Al$_2$O$_3$	476	PMT	2.4 (4)	1.1 (2) $\cdot$ 10^{-1}	2.6 (2) $\cdot$ 10^{-1}	2.3 (3) $\cdot$ 10^{-1}	1.1 (2) $\cdot$ 10^{-1}
PMT window	Quartz	476	PMT	< 1.2	< 2.4 $\cdot$ 10^{-2}	6.5 (7) $\cdot$ 10^{-2}	< 2.9 $\cdot$ 10^{-2}	< 2.5 $\cdot$ 10^{-2}
PMT SS	SS	476	PMT	2.6 (8) $\cdot$ 10^{-1}	1.1 (4) $\cdot$ 10^{-2}	< 6.5 $\cdot$ 10^{-2}	< 3.9 $\cdot$ 10^{-2}	< 5.0 $\cdot$ 10^{-2}
PMT body	Kovar	476	PMT	< 1.4 $\cdot$ 10^{-1}	< 6.4 $\cdot$ 10^{-3}	< 3.1 $\cdot$ 10^{-1}	< 4.9 $\cdot$ 10^{-2}	< 3.7 $\cdot$ 10^{-1}
PMT bases	Cirlex	476	PMT	8.2 (3) $\cdot$ 10^{-1}	7.1 (16) $\cdot$ 10^{-2}	3.2 (2) $\cdot$ 10^{-1}	2.0 (3) $\cdot$ 10^{-1}	1.53 (13) $\cdot$ 10^{-1}

[i] PTFE in TPC walls, rings and pillars and in the plates of the two PMTs support structures.

Table 5.4: Contamination of the materials considered in this work for the XENONnT NR background simulations.

5.4 RADIOGENIC NEUTRON SIMULATIONS

The contamination of the materials considered in the MC model for the prediction of the NR radiogenic background is itemized in Table 5.4, where the ^{238}U and ^{232}Th chains are separated into two branches to account for an observed disequilibrium in the decay chain. Since the neutron yield varies for the different PMT constituents, the contamination for each of them is accounted separately. When only upper limits are available, they have been conservatively treated as true contamination values.

The neutron production rates and their energy spectra for every decay chain of the materials have been calculated via the SOURCES-4A code [64], with the same approach also used for XENON100 [65, 66] and XENON1T [31]. SOURCES-4A takes as an input the number of source nuclides (i.e. the different alpha emitters from the chain we are interested in), the number of target nuclides (the fractional composition of every atom in the detector materials), the minimum and maximum neutron energy to be evaluated, 0 to 10 MeV in this case, and the number of bins for this evaluation. The neutron production rate calculation is scaled to a 1 kg of target material and for contaminations of 1 Bq/kg of the alpha emitters, and it takes into account the (α,n) cross sections and Q-values for the target nuclides, the particle stopping cross section for the elemental constituents and the SF branching for each source nuclide.

The total neutron production rate is derived by rescaling the SOURCES-4A output to the mass of the different materials and the radioactive contamination as given in Table 5.4. The results for every material simulated as a neutron source are detailed in Table 5.5. They are expressed in units of neutrons per decay and without error, although the 17% systematics in the neutron yield from the SOURCES-4A code [64] has been taken into account in the posterior analysis.

The energy spectra obtained for PTFE, the material with the highest neutron production, is shown in Figure 5.8, where the contribution from (α,n) and SF reactions is merged. For heavy materials the neutron production is almost exclusively due to SF. The complete derived set of differential neutron yield spectra for all the involved materials is presented in Figure A.1.

For each of the components listed in Table 5.4, a run of 10^7 neutrons has been simulated with the energy spectra obtained for the neutron sources in Table 5.5. For low energy neutrons (< 20 MeV) the *High Precision* GEANT4 physics list has been used, where the neutron transport and interaction is described via the neutron data files with thermal cross sections G4NDL 3.13, based on the ENDF/B-VI/B-VII databases [67].
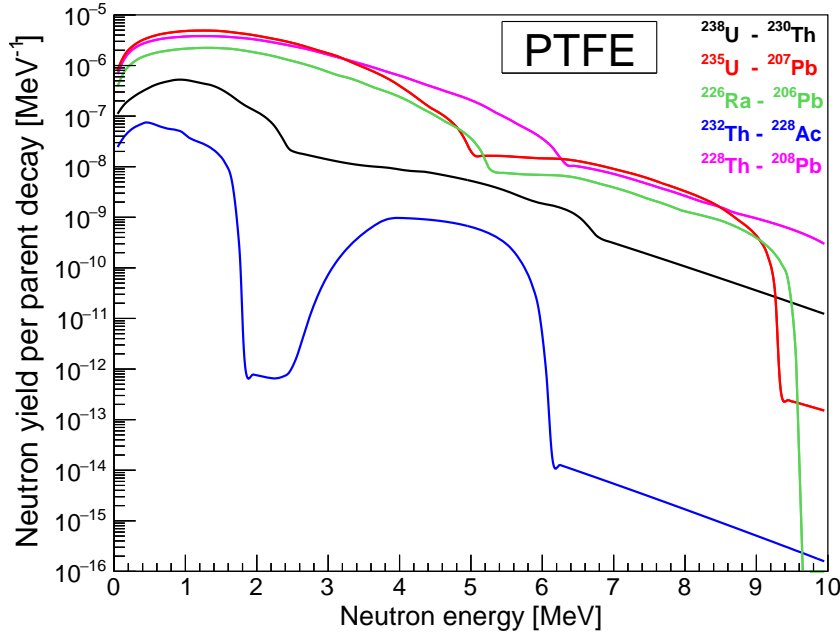
Figure 5.8: Differential neutron production rate from (α,n) and SF reactions in PTFE due to contamination from the ^{238}U, ^{235}U, ^{226}Ra, ^{232}Th and ^{228}Th decay chains.

Material	Neutron yield [neutrons/decay]				
	^{238}U	^{235}U	^{226}Ra	^{232}Th	^{228}Th
Stainless steel	$1.1 \cdot 10^{-6}$	$4.1 \cdot 10^{-7}$	$3.1 \cdot 10^{-7}$	$1.8 \cdot 10^{-9}$	$2.0 \cdot 10^{-6}$
PTFE	$7.4 \cdot 10^{-6}$	$1.3 \cdot 10^{-4}$	$5.5 \cdot 10^{-5}$	$7.3 \cdot 10^{-7}$	$1.0 \cdot 10^{-4}$
Copper	$1.1 \cdot 10^{-6}$	$3.3 \cdot 10^{-8}$	$2.5 \cdot 10^{-8}$	$3.0 \cdot 10^{-11}$	$3.6 \cdot 10^{-7}$
Ceramic	$1.2 \cdot 10^{-6}$	$1.3 \cdot 10^{-5}$	$6.0 \cdot 10^{-6}$	$9.2 \cdot 10^{-9}$	$1.4 \cdot 10^{-5}$
Quartz	$1.2 \cdot 10^{-6}$	$1.9 \cdot 10^{-6}$	$8.8 \cdot 10^{-7}$	$6.8 \cdot 10^{-9}$	$1.9 \cdot 10^{-6}$
Kovar	$1.1 \cdot 10^{-6}$	$1.3 \cdot 10^{-7}$	$1.2 \cdot 10^{-7}$	$3.0 \cdot 10^{-11}$	$1.0 \cdot 10^{-6}$
Cirlex	$1.3 \cdot 10^{-6}$	$2.2 \cdot 10^{-6}$	$3.5 \cdot 10^{-6}$	$4.1 \cdot 10^{-8}$	$2.4 \cdot 10^{-6}$

Table 5.5: Neutron production rates for the materials of the XENONnT experiment involved in the NR background simulations.

5.4.1 *Gadolinium de-excitation in GEANT4*

As reported in [68], for the default *final state* model of GEANT4, the MC modeling of the multiplicity and the energy of Gd de-excitation gamma rays does not match the data available on the measured process. When a ^{155}Gd or a ^{157}Gd absorb a neutron they are excited into the continuum energy levels of the nucleus, and the decay from there to the discrete energy levels seems difficult to model.

For the final state model Gd de-excitations is inadequate, since they often liberate an amount of energy far from the expected Q-value. As an alternative to solve this issue GEANT4 offers the *evaporation model*, which does conserve energy and can be enabled by simply activating a particularhe flag before initializing the run.

In order to compare the performance of both models, for each of them a set of 10^7 neutrons has been generated from the PMTs of the TPC, distributed in a flat energy spetrum from 0 to 10 MeV. With a displacer made out of foam, most of these neutrons, regardless of the number of interactions in LXe, get captured on Gd in the LS volume filled with 0.1 % Gd-LS[8]. The summed energy of the Gd de-excitation products for both models is shown in Figure 5.9, where is shown that the evaporation model correctly predicts the Q-value of the reaction.

For the same set of events also the gamma multiplicity and the energy of these single gammas for a neutron capture on Gd have been visualized (Figures 5.10 and 5.11, respectively).

While the final state model predicts an excess of gamma rays in some cases, the prediction for the evaporation model also seems slightly incorrect, since more
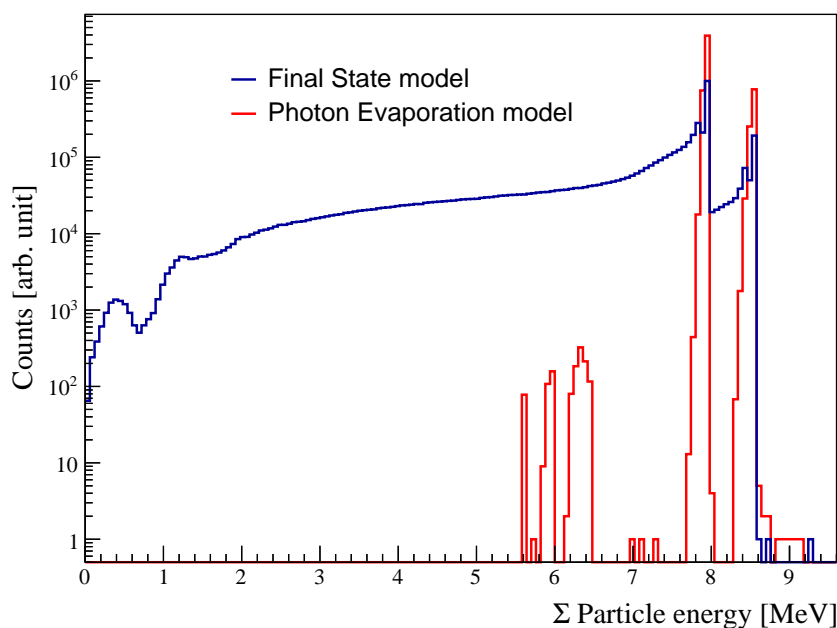
Figure 5.9: Total kinetic energy of all particles produced in a Gd de-excitation for the final state and the evaporation model. In both cases, although only the evaporation model correctly predicts the energy released in the process, the ^{155}Gd and ^{157}Gd de-excitations are clearly distinguishable (information on the binding energy for both isotopes is given in Table 4.1).

---

8 Before event discrimination in the TPC, this already gives a hint on the good neutron veto capabilities of the outer detector
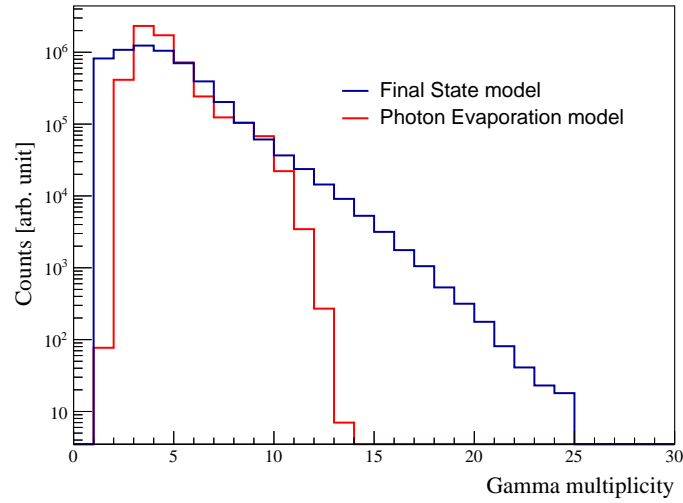
Figure 5.10: Gamma multiplicity comparison between the final state and the evaporation models for Gd de-excitations after capturing a thermalized neutron.
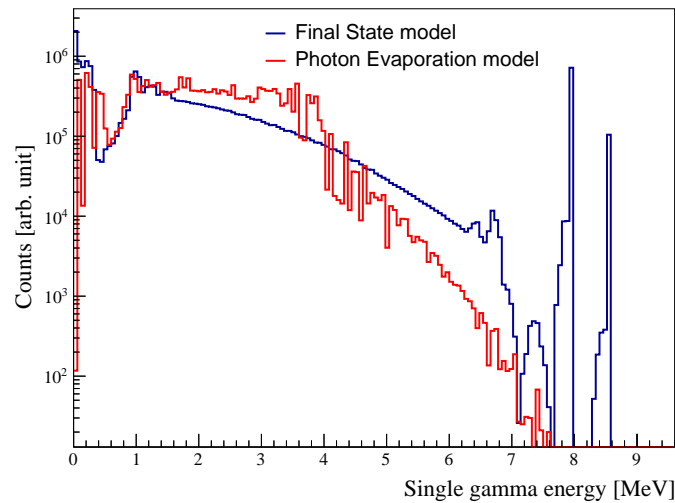
Figure 5.11: Energy of the single gammas produced in Gd de-excitations after capturing a thermalized neutron.

single gamma ray de-excitations are expected [68]. However, there are no further corrections for the the evaporation model for the used neutron data files in this work. After testing both models for a lower set of statistics of real NR background events, and verifying that the impact on the veto efficiency is not major, the evaporation model has been chosen. This way of proceeding agrees with what is done in similar works, e.g. in [69]. Moreover, only via this model conversion electrons could be seen in the simulation, as also reported in [70].

DATA ANALYSIS AND RESULTS

In this chapter, the effectiveness of the neutron veto in XENONnT is determined.

In Section 6.1, the neutron tagging capabilities of the veto are evaluated without taking into account interactions in the TPC. This rough approximation is used to get a feel for the behaviour of the system before a more detailed, computationally heavier, simulation is performed. In Section 6.2, making use of the results from the LCE simulations, the PE yield in the LS for every event is derived. Section 6.3 describes in detail the estimation of the radiogenic NR background in the XENONnT experiment. Corrections to these results with an operative neutron veto are presented in Section 6.4 for the different simulated configurations, and the efficiency of the veto is evaluated for preset energy thresholds and acquisition windows.

For the analysis of the veto response, the list of all energy depositions in the LS is filtered, such that only those processes that are expected to cause light emission are considered. These are the ionization processes from electrons, hadrons and alpha particles. In GEANT4, ionization is responsible for scintillation and the ionization energy is converted into optical photons through the scintillation process.

6.1 NEUTRON THERMALIZATION AND CAPTURE DISTRIBUTION

As a first approach to understand the properties of the implemented veto, a set of 10^6 neutrons has been generated from the TPC PMTs with a flat energy distribution up to 10 MeV, following the procedure of the verifications presented in Section 5.4.1. For this preliminary investigation, a veto thickness[1] of 60 cm has been chosen.

6.1.1 *Energy deposit in the LS*

The total event distribution versus energy deposited in the LS is shown in Figure 6.1 for a mixture of 0.1 % Gd-LS with polyurethane foam filling the buffer between acrylic vessels and outer cryostat. The energy contribution in LS from neutrons captured elsewhere is also accounted[2].

---

1 When referring to the *veto thickness* in this work, the same thickness for all seven vessels is assumed.
2 The contribution from neutrons captured in LXe, computed in the captures in the detector, disappears when evaluating the veto efficiency for NR background events, since a neutron captured on LXe is self-vetoed, due to the distinctive signature of this reaction.
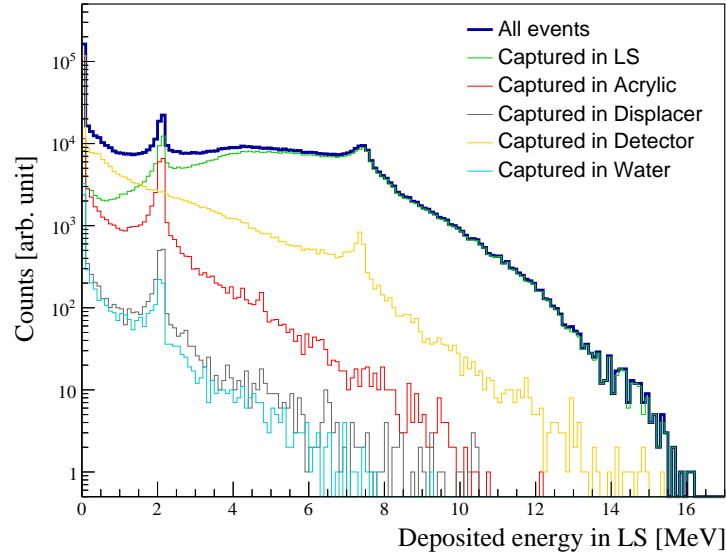
Figure 6.1: Energy distribution in LS for a 0.1 % Gd-LS mixture and foam as displacer material. Corresponding to an energetically flat spectrum of neutrons generated in the TPC PMTs. The thicker blue line is the sum of all the contributions and *captured in detector* stands for neutrons captured in materials inside the volume enclosed by the outer cryostat, e.g., the cyostat itself, the PMTs or the LXe.

The ~ 2.2 MeV peak is due to neutrons capturing on H in the LS, foam, water and acrylic. The relatively high abundance of H and neutron capture cross section lead the peak to be significant. The ~ 8 MeV peak is due to captures on Gd. Events depositing zero energy in the LS are also included in the first bin of the distribution and an enery tale beyond 8 MeV is observed, accounting for elastic scatterings during thermalization or Compton scattered gamma rays.

It is remarkable that for the ~ 8 MeV peak there is a clearly visible contribution from events capturing on detector materials, although one order of magnitude below that of Gd. By setting some specific flags in the simulations, this behavior is found to be mainly due to captures on the nuclei from the cryostat SS, the products of which are highly energetic and can partially reach the LS[3]. For the same volume, (n,p) and (n,α) reactions for fast neutrons can also be observed, although in a very minor proportion with respect to thermal neutron captures. Despite not constituting a capture, their contribution is also summed up for the yellow spectrum in Figure 6.1, as in a real scenario they are sensitive to trigger a potential veto signal.

Given the large capture cross sections for H and Gd, the contribution from events in which the neutron does traverse the LS volume and gets captured in the

---

3 See [41] for specific values of the binding energies.

water is the most insignificant.

Aiming for a better understanding of the performance of different veto configurations, the energy distribution in LS for various of them are displayed together in Figure 6.2, where the standard case for comparison (the spectrum for all events in Figure 6.1) is represented in both plots and corresponds to the pink line. Like in the previous case, all spectra correspond to a run of 10^6 neutrons.

(a) Foam displacer   (b) 0.1 % Gd-LS

Figure 6.2: Comparison of the distribution of energy deposits in the LS, for neutrons generated from the TPC PMTs; (a) for the same polyurethane foam displacer and different Gd loadings in LS and (b) for a volume filled with 0.1 % Gd-LS and different displacer materials. Pink line represents in both figures the spectrum corresponding to a 0.1 % Gd-LS mixture with foam as displacer.

Without Gd loading, the peak at $\sim 8\,\mathrm{MeV}$ falls off (blue spectrum in Figure 6.2(a)) and the contribution from events 'captured' in the detector becomes predominant in that region. Spectra for differently doped mixtures behaves similarly. For increasing Gd loading, the $\sim 2.2\,\mathrm{MeV}$ and the $\sim 8\,\mathrm{MeV}$ contributions become less and more predominant, respectively. On the other hand, by keeping the standard 0.1 % Gd-LS mixture but using water as displacer material (the case of a not hermetically sealed neutron veto), the signal acquisition of the veto severely decreases (6.2(b)).

6.1.2 *Time of veto threshold crossing*

For the same data sets, the time of neutron capture in the sensitive LS volume has been represented in Figure 6.3; also with the same color legend as the one previously used, alowing for direct comparison on how both characteristics are affected depending on the configuration. Two particular features can already be pointed out from Figure 6.3(a):

- For an undoped mixture the time of neutron capture falls exponentially and this behavior becomes the sum of two exponentials when loading Gd into
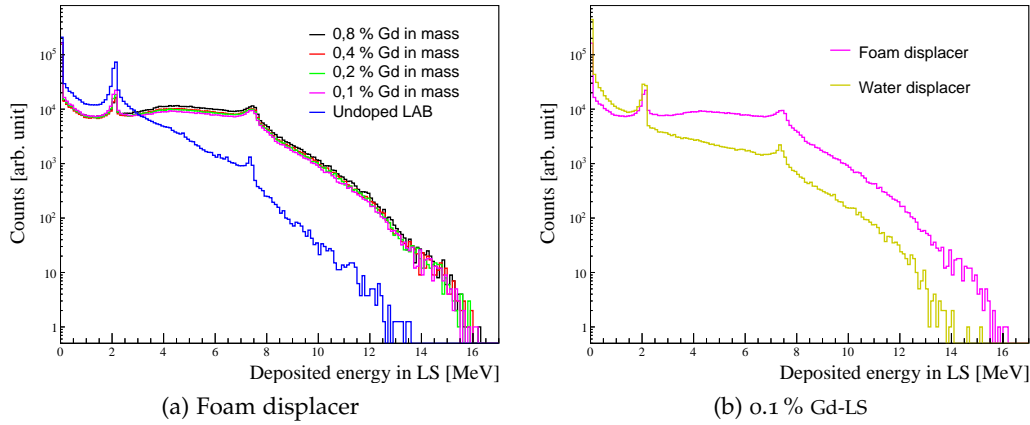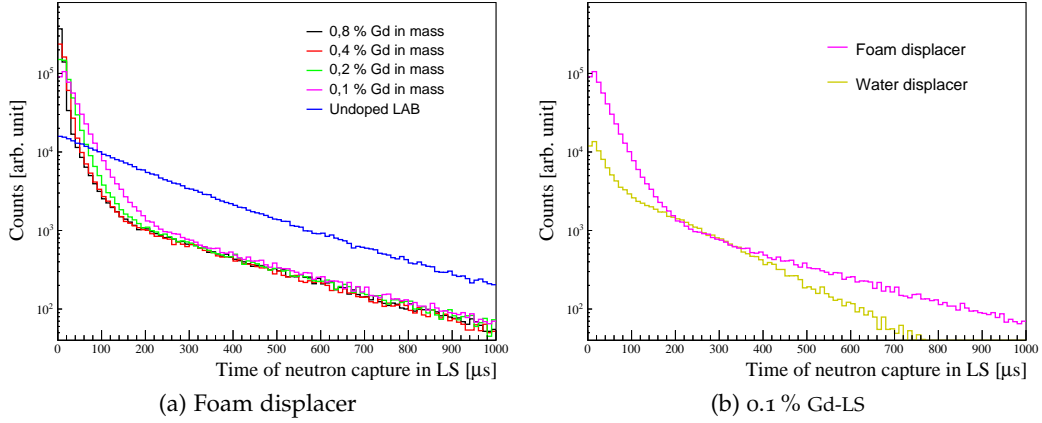
Figure 6.3: Comparison of the distribution of the time of neutron capture in the LS, for neutrons generated from the TPC PMTs; (a) for the same polyurethane foam displacer and different Gd loadings in LS and (b) for a volume filled with 0.1 % Gd-LS and different displacer materials. Pink line represents in both figures the spectrum corresponding to a 0.1 % Gd-LS mixture with foam displacer.

the LS. For small capture times, with an increasing steepness for higher proportions of the metal. This can be explained by the rapid captures induced by the high cross section of Gd. For larger capture times (above $\sim 200\,\mu$s), the second exponential dominates, which shows the same behavior as the one for the undoped mixture.

- The first bin, which does not completely adjust to the inferred exponential behavior, accounts for an insufficient time for the fastest neutrons reaching the LS to become thermal and get captured. This thermalization time directly competes with the high cross section of Gd, hence the contribution from the first bin slowly overcomes that of the second one when increasing the Gd concentratrion.

Although the time distribution of captures offers a good approximation of the neutron veto efficiency for different time windows, the real input that must be considered is the time for veto signal deposition. The difference between these two times is almost insignificant when dealing with actual captures in the LS, but becomes relevant when the vetoed event has been captured elsewhere. One of the main channels for this process is the backscatter of neutrons from the LS into other volumes, which produces a delay in the subsequent capture and the ionization of the products reaching the LS.

For 400 keV, the most conservative energy deposit threshold set in the veto analysis, the vetoing time versus the time of neutron capture (single spectra from Figure 6.3(a)) in the LS is shown in Figure 6.4, for a configuration with foam as displacer material.
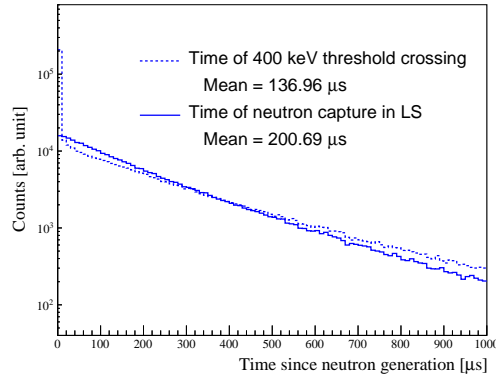
(a) LAB + fluors
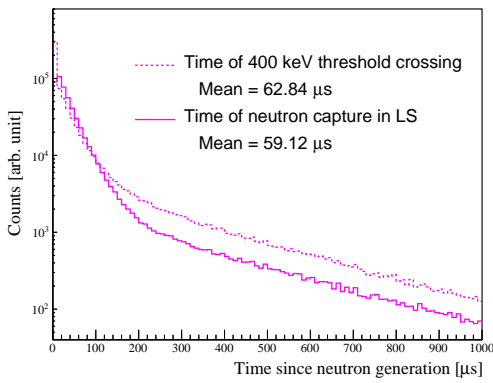
(b) 0.1 % Gd-LS
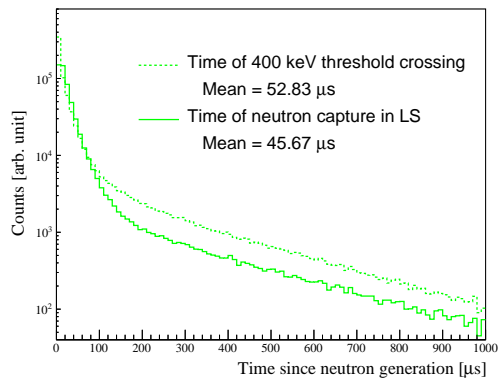
(c) 0.2 % Gd-LS
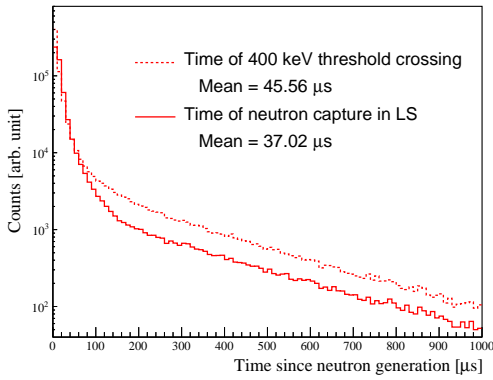
(d) 0.4 % Gd-LS
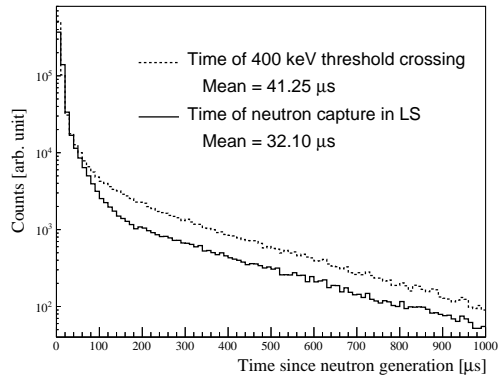
(e) 0.8 % Gd-LS

Figure 6.4: Distribution of times of first threshold crossing and neutron capture in LS for different veto mixtures and foam as displacer material.

The variable for this and the subsequent studies is, as depicted on the *x* axes from these plots, the time since the neutron is generated in the XENONnT components. This conservative approximation has been set after studying the time of interaction in the TPC for NR background events. Its value is in most of the cases in the order of a few nanoseconds after neutron production, therefore negligible when considering deposit times as the ones sketched in Figure 6.4.

Given that the same data set has been used to produce both spectra for each plot, the main conclusions extracted from here are:

- For any of the loading options, the amount of vetoed events for a large time window is always higher than the number of captured neutrons, even for the a conservative vetoing threshold. It is proven that secondaries from neutron captures in other volumes frequently deposit sufficient energy in the LS, while products from captures in LS rarely escape this volume (as could already be pictured from Figure 6.1).

- Most of this excess arises from prompt deposits by protons following the elastic scatterings that neutrons undergo during thermalization. This can be seen in the first 10 μs bin of the spectra in Figure 6.4, where the amount of vetoed events is far above that of captured neutrons.

- Gd loading appears to allow for smaller veto windows and overcomes the delay between the time of fast vetoed events and captures in LS.

Following this rough understanding, the features of the veto against neutrons are fully characterized and the framework of this chapter is defined. In the following, the study is restricted to simulations of the real NR background.6.3.

6.2 LIGHT COLLECTION EFFICIENCY

LCE constitutes one of the two building blocks of estimating the detector efficiency, since will define the goodness to effectively detect the different vetoing energies assumed for the LS.

Runs of 10^7 optical photons isotropically distributed in the LS volume have been initialized for each of the veto PMT arrangements specified in Section 5.3, and following the energy distribution of the bis-MSB emission after 1 cm of propagation (see Figure 5.7). The LCE is calculated over the whole volume,

$$LCE = \frac{N_{det}}{N_{gen}} \tag{6.1}$$

where N_{gen} and N_{det} stands for generated and detected photons, respectively; and for each individual (R²,Z) pixel, using the axial symmetry of the acrylic vessels around the cryostat:

$$LCE(R^2, Z) = \frac{N_{det}(R^2, Z)}{N_{gen}(R^2, Z)} \tag{6.2}$$

Examples of the LCE maps derived in this investigation are shown in Figures 6.5, for a veto thickness of 60 cm, and in 6.6 for a thickness of 30 cm. Results for the averaged LCE in the LS volume for all the inspected configurations are presented in Table 6.1, where the error is assumed to be binomial:

$$\sigma_{LCE} = \frac{\sqrt{N_{det} \cdot (1 - LCE)}}{N_{gen}} \tag{6.3}$$

	LCE [%]									
		72 extra PMTs			96 extra PMTs			120 extra PMTs		
Veto thickness	No extra PMTs	80 cm	70 cm	60 cm	80 cm	70 cm	60 cm	80 cm	70 cm	60 cm
30 cm	1.08(3)	4.37(6)	4.61(7)	4.84(7)	5.42(7)	5.70(7)	6.00(8)	6.42(8)	6.77(8)	7.13(8)
40 cm	1.10(3)	4.28(6)	4.47(7)	4.70(7)	5.27(7)	5.54(7)	5.83(7)	6.24(8)	6.58(8)	6.92(8)
50 cm	1.13(3)	4.13(6)	4.33(6)	4.51(7)	5.08(7)	5.35(7)	5.59(7)	6.00(8)	6.32(8)	6.60(8)
60 cm	1.14(3)	3.99(6)	4.15(6)	4.34(6)	4.90(7)	5.12(7)	5.33(7)	5.78(7)	6.05(8)	6.30(8)

Table 6.1: LCE as a function of the veto thickness, the number of side veto PMTs and their distance to the outer part of the acrylic vessels. For the configuration with no extra PMTs only the ones already present in the water tank are active. For this case, it makes sense that the LCE over the full volume increases for increasing thickness, since the distance from the center of mass of the individual vessels to the water tank walls decreases. On the other side, for an array at a fixed distance to the acrylic vessels, light collection is higher for decreasing thicknesses, since the solid angle covered by photodetectors increases.

(a) No extra PMTs.

(b) 72 extra PMTs at 60 cm.

(c) 96 extra PMTs at 60 cm.

(d) 120 extra PMTs at 60 cm.

Figure 6.5: LCE maps for a veto 60 cm thick and extra PMT arrays at 60 cm. Color scale has been kept constant for every map, for direct comparison.

(a) No extra PMTs.

(b) 72 extra PMTs at 60 cm.

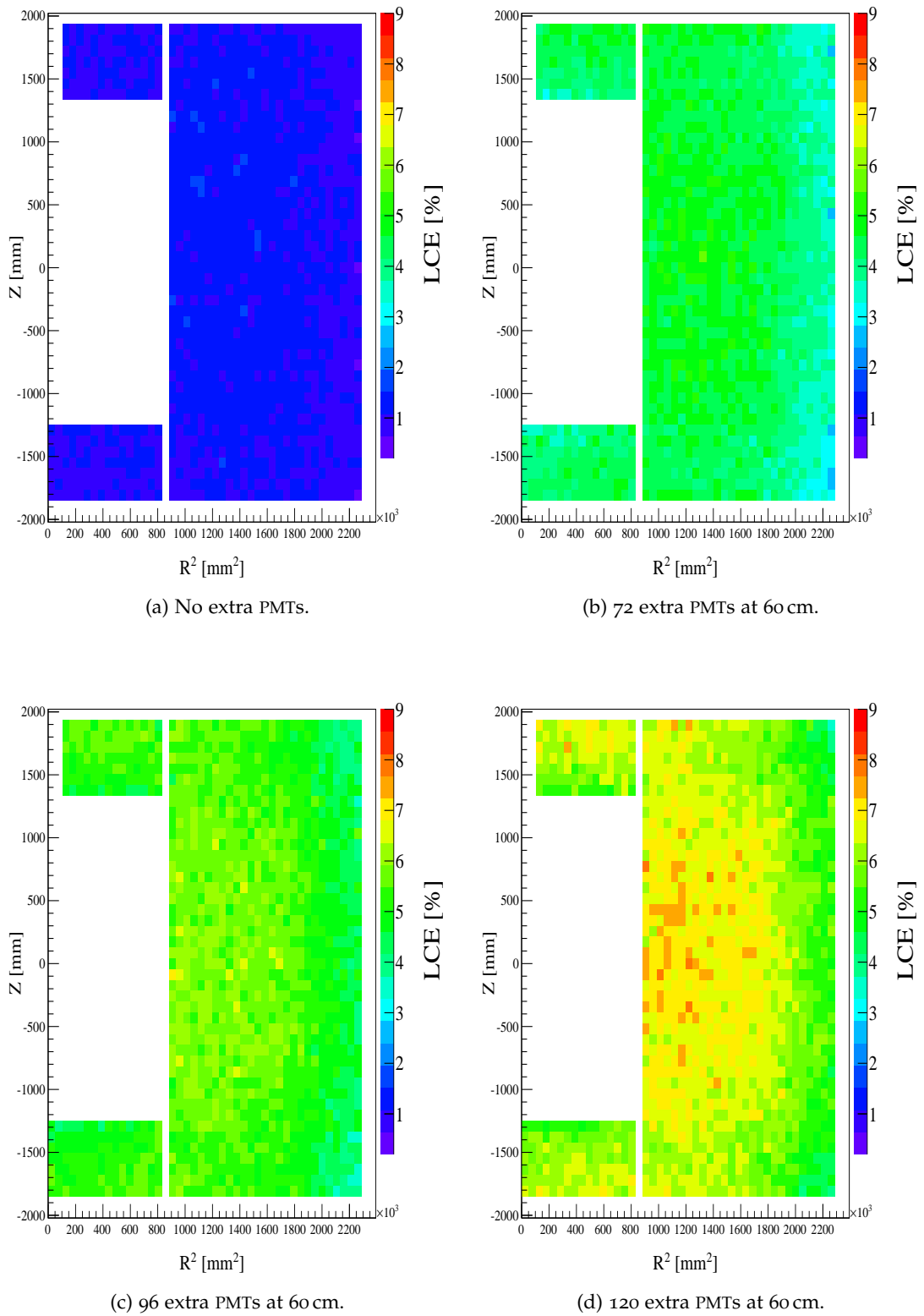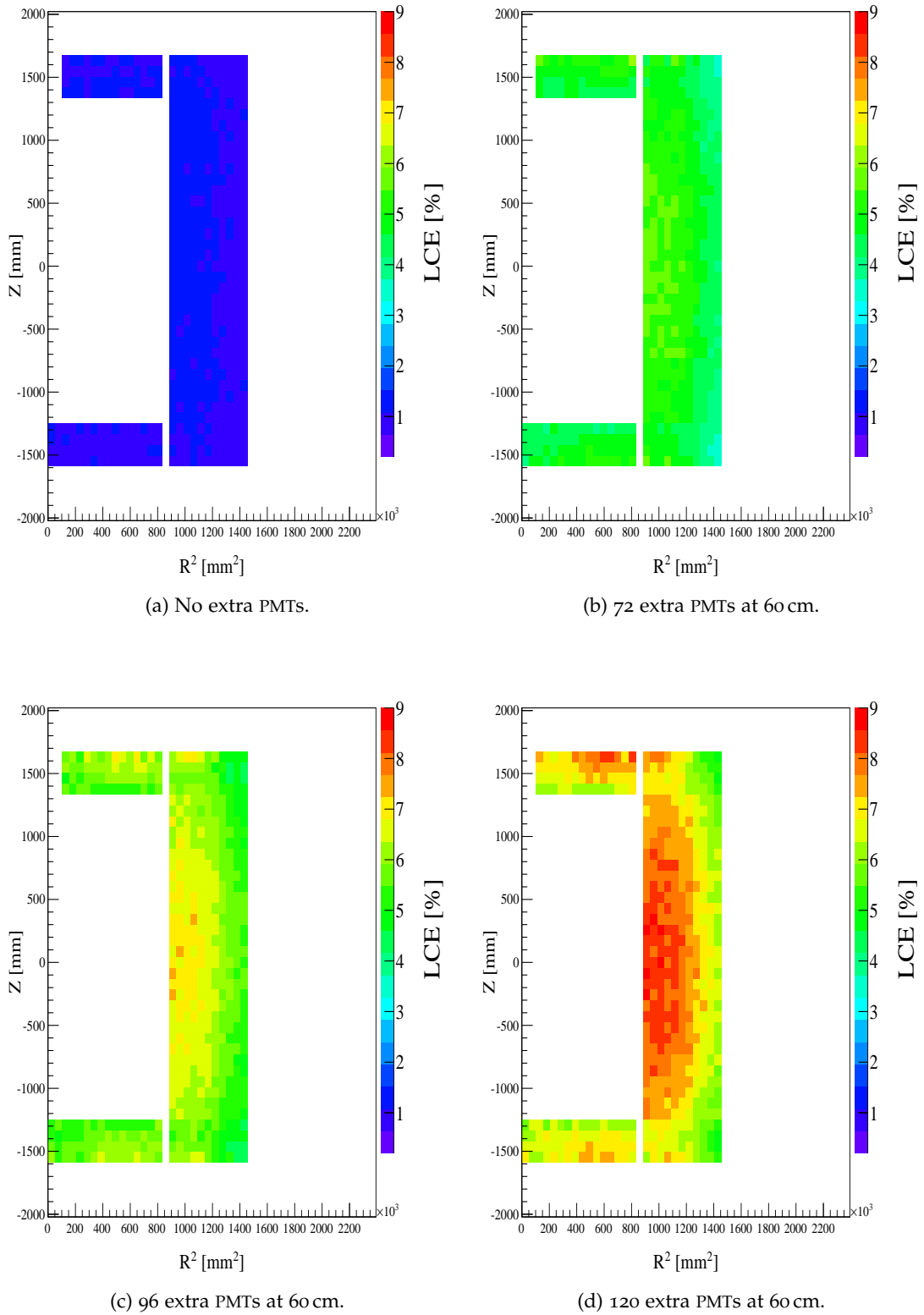(c) 96 extra PMTs at 60 cm.

(d) 120 extra PMTs at 60 cm.

Figure 6.6: LCE maps for a veto 30 cm thick and extra PMT arrays at 60 cm. Color scale has been kept constant for every map, for direct comparison.

6.2.1   *Calculation of the photoelectron yield*

The specific number of detected PEs or PE yield can be calculated from the previous results by rescaling the light collection efficiency (LCE) with the light yield (LY) of the mixture and the quantum efficiency (QE) and collection efficiency (CE) of the PMTs; i.e.:

$$PE_y(\mathbf{r}) = f_{PE}(\mathbf{r}) \cdot LY = LCE(\mathbf{r}) \cdot QE \cdot CE \cdot LY \tag{6.4}$$

where f_{PE} is the probability for a photon to be detected (to produce a photoelectron).

In this work, the values have been fixed to:

- LY = 9 photons/keV

- QE = 25 %

- CE = 85 %

where the LY is equal to the one argued by Daya Bay [46] and the QE is a rather conservative approximation of what has been described in Figure 5.6(a), since the fluorescence emission spectra for bis-MSB only after 1 cm of propagation in the LS has been considered for these simulations (Figure 5.7). CE value is given as provided by the manufacturer for the range (300, 600) nm [56].

With these values together with the results in Table 6.1, the average PE yield in the scintillator volume can be estimated. E.g., for a 30 cm outer detector with 120 side veto PMTs placed 60 cm away from the acrylic, the LCE in Table 6.1 is equal to 7.13(8) %, which corresponds to a PE yield of $\sim$ 136 PE/MeV, according to Equation (6.4). On the other hand, for the lowest LCE obtained, that of the arrangement with only the current water PMTs and also a thickness of 30 cm, an average value of 1.08(3) % LCE yields only $\sim$ 21 PE/MeV.

For the derivation of the real PE yield per generated neutron, each of the individual tracks in LS has been evaluated as follows:

1. Hits are sorted according to their type, as already described: only ionization processes from electrons, protons and alpha particles are accounted as sources for the scintillation light.

2. The mean value of the generated optical photon distribution is obtained from the quenched energy deposit Ed of the hit

$$\langle N_{ph} \rangle = Ed \cdot LY \tag{6.5}$$

and the observed photon yield is calculated by drawing random values of the function:

a) If $N_{ph} \leqslant 10$:

$$N_{ph}^{gen} = \text{Poisson}(\langle N_{ph} \rangle) \tag{6.6}$$

b) If $N_{ph} > 10$:

$$N_{ph}^{gen} = \text{Gauss}(\langle N_{ph} \rangle, \sqrt{\langle N_{ph} \rangle}) + 0.5 \tag{6.7}$$

following the procedure implemented in GEANT4 when the scintillation process is active (see [71]).

3. For the position of the interaction, $LCE(R^2, Z)$ is obtained from the LCE maps for all the evaluated configurations[4]. With this value, the $f_{PE}(R^2, Z)$ is directly obtained as indicated in Equation (6.4).

4. Finally, to obtain the detected PEs there is a binomial process involved, of actually releasing an electron from the PMT cathode when hitting it with a photon:

$$PE_y = \text{Binomial}(N_{ph}^{gen}, f_{PE}(R^2, Z)) \tag{6.8}$$

The output from this loop over every track is the total PE yield of a single event for an unlimited acquisition window[5].

6.3 NUCLEAR RECOIL BACKGROUND CALCULATION

The materials used for the NR background simulations, their radioactive contamination and the considered neutron yield for the different decay chains are listed in Section 5.4. With 10^7 events simulated for every source, the corresponding statistical uncertainty is $< 1\,\%$, therefore the error on the detected/vetoed events is dominated by the $17\,\%$ SOURCES-4A systematic uncertainty.

At the time of writing, although the main decisions towards the ugprade to XENONnT have been taken and assembly and test of the different components are ongoing, the question on whether using a bell or not is still under discussion, in the context of pursuing the best method to succesfully stabilize the LXe level. In any case, and as shown in Figure 3.3, the current XENONnT TPC design foresees the placement of this volume, and the implementation of the detector in GEANT4 has been done accordingly. In order to assess the potential NR background induced by the bell, neutron simulations (without veto) have been performed for a calculated mass of 125 kg and a contamination equal to that specified for the

---

4 Since every NR background simulation is done for a precise veto thickness, this step is repeated for every of the studied PMT arrangements (a single row in Table 6.1) Therefore for an interaction in LS ten values for the PE yield are derived.

5 As described in Section 5.3, considerations on the time of signal detection have been done for the analysis on the ionization deposits in the LS

cryostat shells in Table 5.4 [30]. These simulations yielded a result for the contamination from the bell of $\sim 1.53\,\%$ of the total NR background for a LXe fiducial mass of 5 tonnes and $\sim 1.62\,\%$ for 4 tonnes. With this issue already addressed, results for the bell are not accounted in the following.

6.3.1 *Event selection in the TPC*

Neutrons often undergo multiple scatters in the TPC due to their short path lengths, which is a method to flag them as not WIMP-like signature events. Background events are classified by selecting a single elastic scatter interaction in the FV of the TPC and in the dark matter search energy range, being the capability to distinguish two scatters dependent on the width of the charge signal (S2) in the time domain and on the efficiency to sort the individual peaks.

Based on the XENON100 detector resolution [72], the condition originally set in XENON1T simulations to *clusterize* (to consider as single scatter) a multiple scatter event was for the interactions to be confined within 3 mm in the vertical direction. With XENON1T already operative, this condition has been verified to be rather optimistic for a drift length much longer than that of XENON100. The details on the development of this study [73], still under revision, are beyond the scope of this thesis.

The new clusterization algorithm derived from it, however, has been implemented in the NR analysis developed in this work for all the simulation data sets. This parameterisation yields a new vertical resolution between 4 and 10 mm, with an average value of 6 mm. To interpret the impact of this new condition, an inspection with the old and the new algorithm has been performed. The results indicate that the new updated resolution to multiple scatters causes an increase of $\sim 11\,\%$ in the total predicted NR background from the detector materials[6].

For a simulated event to be considered reponsible for a single elastic scattering in LXe, one of the two following conditions have to be fulfilled:

- Only a single elastic scatter is recorded in the FV (after possible clusterization).

- More than one of these interactions is recorded, with the second largest S2 signal being smaller than 100 PE (about 5 drifted electrons).

The second case is based on the actual performance of the XENON100 and XENON1T detectors. When, for example, two scatters with very low energy (< 1 keV) take place, their probability to generate an S2 is rather small, hence this case might appear as a single scatter in the readout signal. To separate these events from those in which two suffiently energetic scatters happen, an upper

---

6 An increase of the same order is also induced for XENON1T[74], which still does not endanger the NR background-free operation expected over two years of data taking.

limit is set on the second largest signal generated.

In this work, the XENON collaboration ER- and NR-sorting script, used to convert the deposited energy in LXe into light (S1) and charge (S2) signals, has been adapted for the XENONnT geometry. This tool is based on measured detector conditions and uses the approach of the Noble Element Simulation Technique (NEST) for scintillation yield in LXe [75]. For details on how this conversion takes place see Reference [31].

6.3.2 *Background prediction for XENONnT*

Under the conditions specified, neutrons from the different radioactive sources have been processed. For a set of $N_{generated}$ events with a differential energy distribution following that of a specific decay chain in a specific component (see Figures 5.8 and A.1), the time needed for this amount of events to occur in real detector conditions is equal to

$$t_{run} = \frac{N_{generated}}{n_{yield} \cdot (A_{screened} \cdot 10^3) \cdot mass_{source}} \tag{6.9}$$

where n_{yield} is the neutron yield for the corresponding decay chain and material, as itemized in Table 5.5; $A_{screened}$, the corresponding activity, given in Table 5.4 and $mass_{source}$ the kg (or units, in the case of PMTs) in XENONnT for the evaluated component. When considering the values as they are shown in the respective Tables, t_{run} has units of seconds.

For this study, the properties of the interactions constituting a NR event in the TPC are used to fill three different one-dimensional distributions:

1. Background events as a function of the energy deposited in LXe.

2. Background events as a function of the primary energy of the emitted neutron.

3. Background events as a function of the S1 signal detected.

The NR background rate has been calculated as

$$Rate_{NR} = \frac{N_{selected}}{t_{run}/86400 \cdot Mass_{fiducial}} \tag{6.10}$$

in DRU, where $N_{selected}$ corresponds to the sorted NR background events, t_{run} is rescaled such that the time unit is the day, and $Mass_{fiducial}$ corresponds to the considered fiducial mass of LXe, also set as a filter to sort events.

Rescaled distributions are summed up for all the decay chains and materials. The resulting total XENONnT NR background spectra are shown in Figures 6.7, 6.8 and 6.9 for FVs of 4 and 5 tonnes.

Figure 6.7: Energy spectra of the NR background rate from material radioactivity in XENONnT. Dashed red lines confine the 4-50 keV range, lower and upper limits for dark matter analysis.

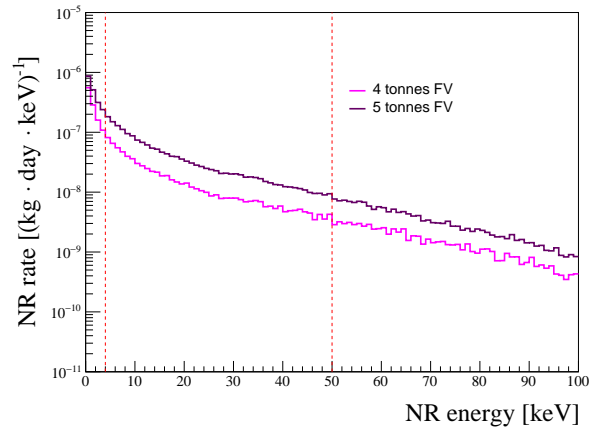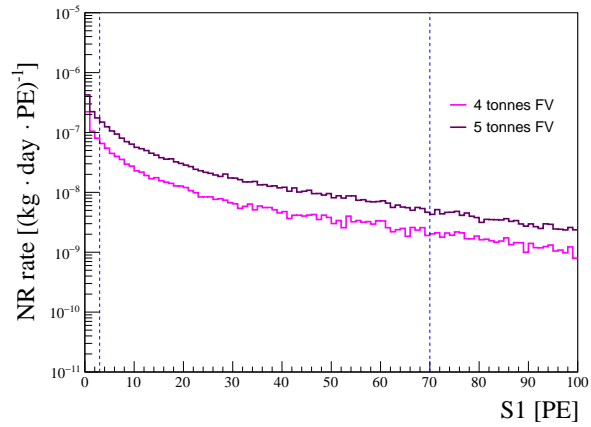

Figure 6.8: S1 spectra of the NR background rate from material radioactivity in XENONnT. Dashed blue lines confine the 3-70 PE range.
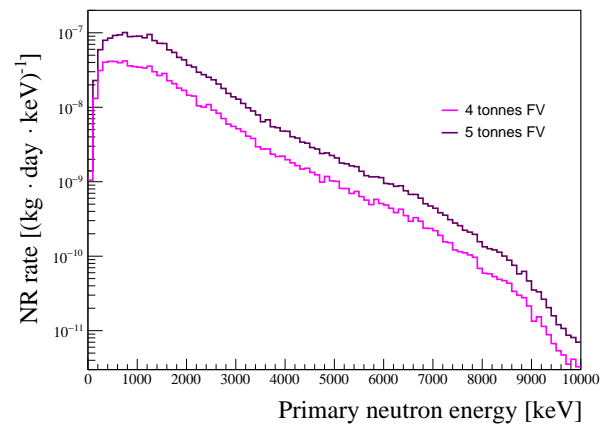

Figure 6.9: Initial neutron energy spectra of the NR background rate from material radioactivity in XENONnT.

In Figures 6.7 and 6.8, equivalent deposits are represented by the dashed red and blue lines, respectively. Lower and upper thresholds for dark matter analysis, and approximations of the corresponding S1 signal for given detector conditions, respectively. For a specific FV, by integrating over these energy and PE ranges, the obtained NR background rate in units of $(kg \cdot day)^{-1}$ in the same for both distributions. Hence for the case of NR radiogenic background the analysis can be directly performed on the real energy deposit of the scatters (Figure 6.7).
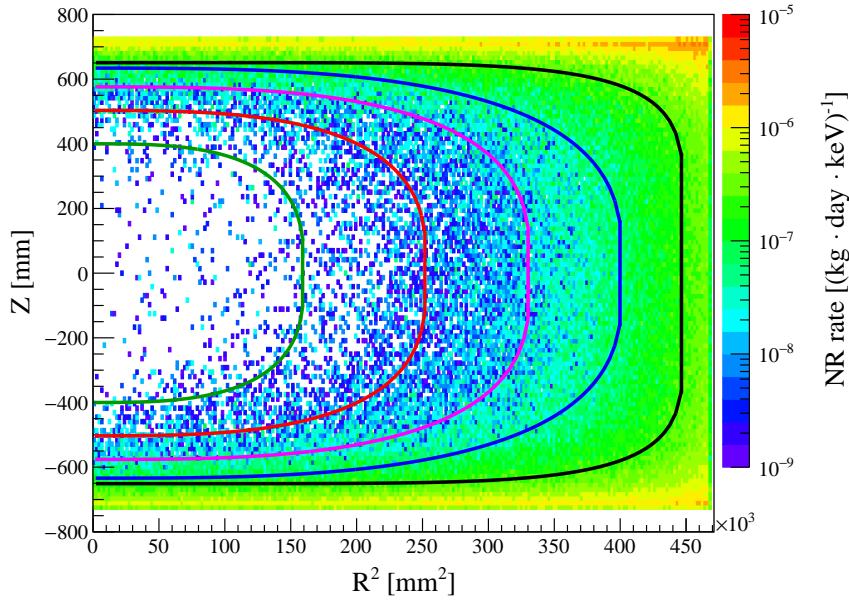
Figure 6.10: Spatial distribution of the NR background events from radiogenic neutrons inside the LXe in the (4,50) keV energy range. White regions are indicative of a background rate smaller than 10^{-9} $(kg \cdot day \cdot keV)^{-1}$. The green, red, pink, blue and black curves represent fiducial volumes of 1, 2, 3, 4 and 5 t, respectively.

The two-dimensional distribution of background events over the whole sensitive LXe volume has also been produced. For this case, unlike in the three previous figures, the full volume of the sensitive region (~ 6 t) is displayed and the cut has been performed on the energy range of dark matter search (4 to 50 keV deposit), instead of on the mass. The resulting histogram is represented in Figure 6.10. The 1 to 5 t FVs are drawn as enclosed by a superellipsoid, described in the z-R^2 plane by

$$\left| \frac{R^2}{a_r} \right|^{n_r} + \left| \frac{z - z_0}{a_z} \right|^{n_z} = 1 \tag{6.11}$$

with $a_r = a_z{}^2$ and z_0 = -9 mm, accounting for the offset of the center of the LXe sensitive volume with respect to that of the TPC[7]. For the first four FVs, $n_r = n_z = 3$, whereas for 5 t FV a power of five superellipsoid is employed, as a more suitable

---

7 Offset corrected for the figure, in which the center of the LXe volume is placed at $z = 0$

geometry in terms of NR background rejection due to self-fiducialization of the LXe[8].

For the NR differential rate representation in the two-dimensional display, the background events are rescaled as

$$Rate_{NR} = \frac{N_{selected}}{t_{run}/86400 \cdot Mass_{bin} \cdot (50 - 4)} \tag{6.12}$$

where the factor $(50 - 4)$ is simply the energy range of interest (equivalent to integrating between these two values in Figure 6.7) and $Mass_{bin}$ accounts for the mass of a single bin in the plot, calculated by knowing the exact size of the full sensitive region, the binning applied to the histogram and the density of LXe.

To compute the NR background rate for various FVs, a loop in Figure 6.10 is performed, to sum up the rates in each bin for increasing $|z|$ and R^2 and following the geometrical shapes of the FVs defined by Equation (6.11). This constitutes, in addition, another verification for the results obtained by integrating for the range of interest in Figures 6.7 and 6.8, therefore the production and comparison of these three different distributions has been included in the methodology for analyzing every data set. The results of this evaluation, rescaled for a year of activity, are shown in Figure 6.11 for three different energy ranges of recoiling deposits, to get a feel on how the lower energy threshold affects the amount of background events.
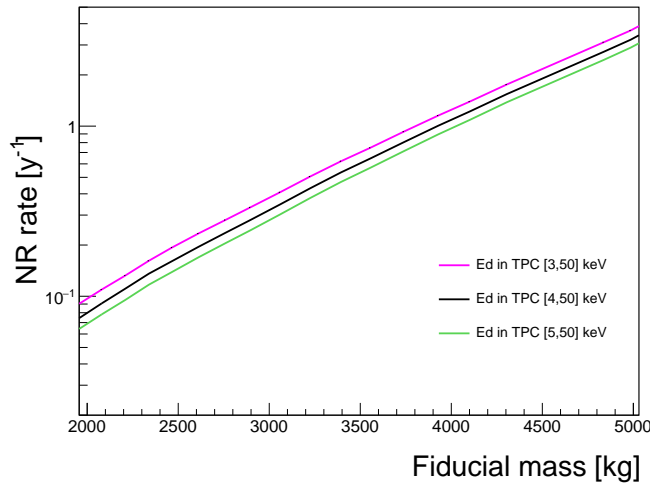
Figure 6.11: NR background rate from radiogenic neutrons as a function of the fiducial mass. The black line accounts for the backgroun events detected in the energy range of dark matter search, while the pink and the green contributions are shown for orientation on the impact of changing these limits.

---

8 The FV geometries displayed have also been implemented in the analysis, to sort the different events depending on the volume in which they scatter, as previously done in Figures 6.7, 6.8 and 6.9 for 4 and 5 tonnes.

The total XENONnT NR radiogenic background from the curves is:

Fiducial mass [t]	NR background rate [y⁻¹]		
	(3,50) keV	(4,50) keV	(5,50) keV
3	0.38(6)	0.32(5)	0.28(5)
4	1.3(2)	1.1(2)	1.0(2)
4.2	1.6(3)	1.4(2)	1.2(2)
4.4	2.0(3)	1.8(3)	1.6(3)
4.6	2.5(4)	2.2(4)	2.0(3)
4.8	3.0(5)	2.7(5)	2.4(4)
5	3.7(6)	3.3(6)	3.0(5)

Table 6.2: NR background rate as a function of the fiducial LXe mass and the energy range of interest.

In the following, studies concentrate on the elastic scattering energy range of interest. For this range, the contributions from the different simulated components to the NR background is detailed in Table 6.3.

Component	Material	NR background generated [%]	
		4 tonnes fiducial	5 tonnes fiducial
Cryostat shells	SS	20.4	20.7
Cryostat flanges	SS	8.3	8.7
TPC panels	PTFE	30.2	34.3
TPC plates	Cu	6.3	6.6
PMT stem	Al_2O_3	20.9	18.0
PMT window	Quartz	4.4	3.8
PMT SS	SS	1.2	1.0
PMT body	Kovar	1.7	1.4
PMT bases	Cirlex	6.6	5.5

Table 6.3: Generated proportion of NR background events by the considered detector components. Single elastic scatter in the LXe FV depositing from 4 to 50 keV is required.

For increasing FVs, the relative contribution from cryostats, PTFE panels and copper plates also increases, since the sensitive detector edges get closer to them. For the total target (∼6 t), the spatial distribution of the initial positions of radiogenic neutrons produce a background is depicted in Figure 6.12, where the features deduced from Table 6.3 can be observed.

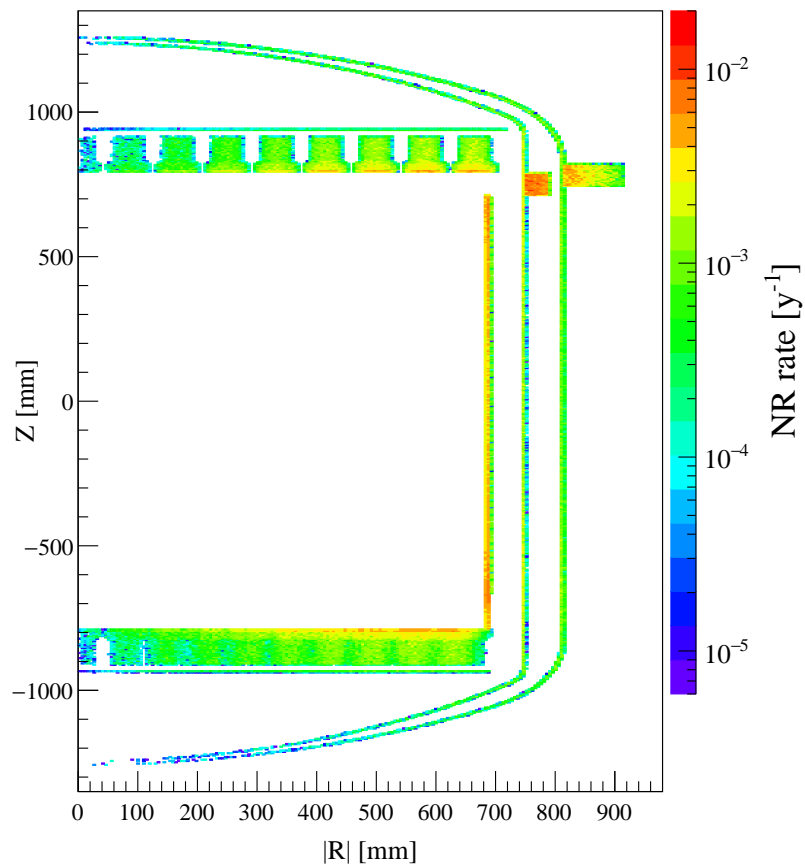Figure 6.12: Axial view of the primary position distribution of the radiogenic neutrons that constitute a NR background event in the full LXe target. The sources components employed to characterize this background can be distinguished: inner and outer cryostat, PMTs, PTFE panels and copper plates. The integral over the full distribution yields the NR background in the whole target: $13 \pm 2\,y^{-1}$.

6.4 PERFORMANCE OF THE NEUTRON VETO

In this chapter, the performance of three neutron veto configurations is explored for every of the derived steps. The first of these is the baseline configuration, while the other two correspond to possible non-geometric changes for the veto. These configurations are:

1. 0.1 % Gd-LS mixture, 60 cm thick vessels and foam as displacer. Chosen based on the need for:

   - An optimized veto size, i.e. vessels large enough to contain gamma rays following capture reactions, but accounting for the limiting mechanical factors for operation inside the water tank.

   - A stabe metal-loaded mixture, since undoped LAB seems inadequate in terms of acquisition time of the veto signal, and loadings greater than 0.1 % by weight might entail a significant increase in the complexity of the mixture production and degradation in the optical properties.

   - A material of low density to fill the gaps between the veto structure and the cryostat, to enhance energy deposits in the LS.

2. 0.1 % Gd-LS mixture, 60 cm thick vessels and water as displacer.

3. Undoped LS mixture, 60 cm thick vessels and foam as displacer.

6.4.1 *Veto on the energy in the LS*

Following the same procedure as in the prevous section, the background rate has been derived for the case of an operative neutron veto. For a single event, after sorting whether it does or does not constitute a single NR in the TPC, a coincidence in the LS is searched for. Namely, four different energy thresholds have been defined in this study as necessary to veto a NR: 50, 100, 200 and 400 keV.

For the three veto configurations selected, the resulting NR spatial distribution for the considered threshold is drawn, where the color scale of the z axis has been fixed to that of Figure 6.10, for direct comparison. One can already ratify the background decrease with respect to the radiogenic background derived for a XENONnT detector without veto. The corresponding rate versus fiducial mass plot is also derived for every case, where the solid black curve always matches the one from Figure 6.11.

(a) 50 keV veto threshold

(b) 100 keV veto threshold

(c) 200 keV veto threshold

(d) 400 keV veto threshold

Figure 6.13: Spatial distribution of NR background events in the (4,50) keV energy range with a 0.1 % Gd-LS, 60 cm thick veto with foam as displacer.

Figure 6.14: NR background rate from radiogenic neutrons as a function of the fiducial mass for a 0.1 % Gd-LS veto 60 cm thick with foam displacer. Solid back line represents the NR background without neutron veto. Results correspond to an ideal acquisition window.

(a) 50 keV veto threshold

(b) 100 keV veto threshold

(c) 200 keV veto threshold

(d) 400 keV veto threshold

Figure 6.15: Spatial distribution of NR background events in the (4,50) keV energy range with a 0.1 % Gd-LS, 60 cm thick veto with water as displacer.
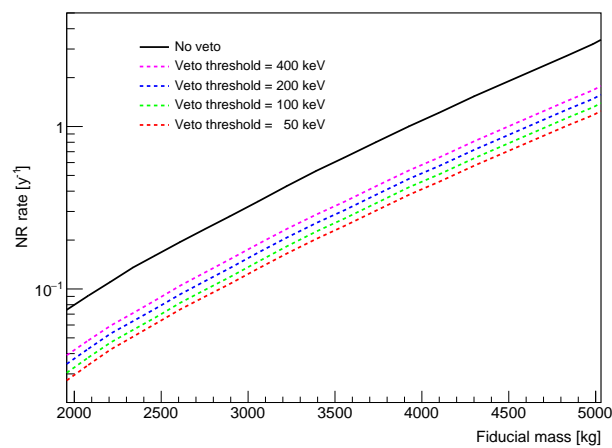
Figure 6.16: NR background rate from radiogenic neutrons as a function of the fiducial mass for a 0.1 % Gd-LS veto 60 cm thick with water displacer. Solid back line represents the NR background without neutron veto. Results correspond to an ideal acquisition window.

(a) 50 keV veto threshold

(b) 100 keV veto threshold
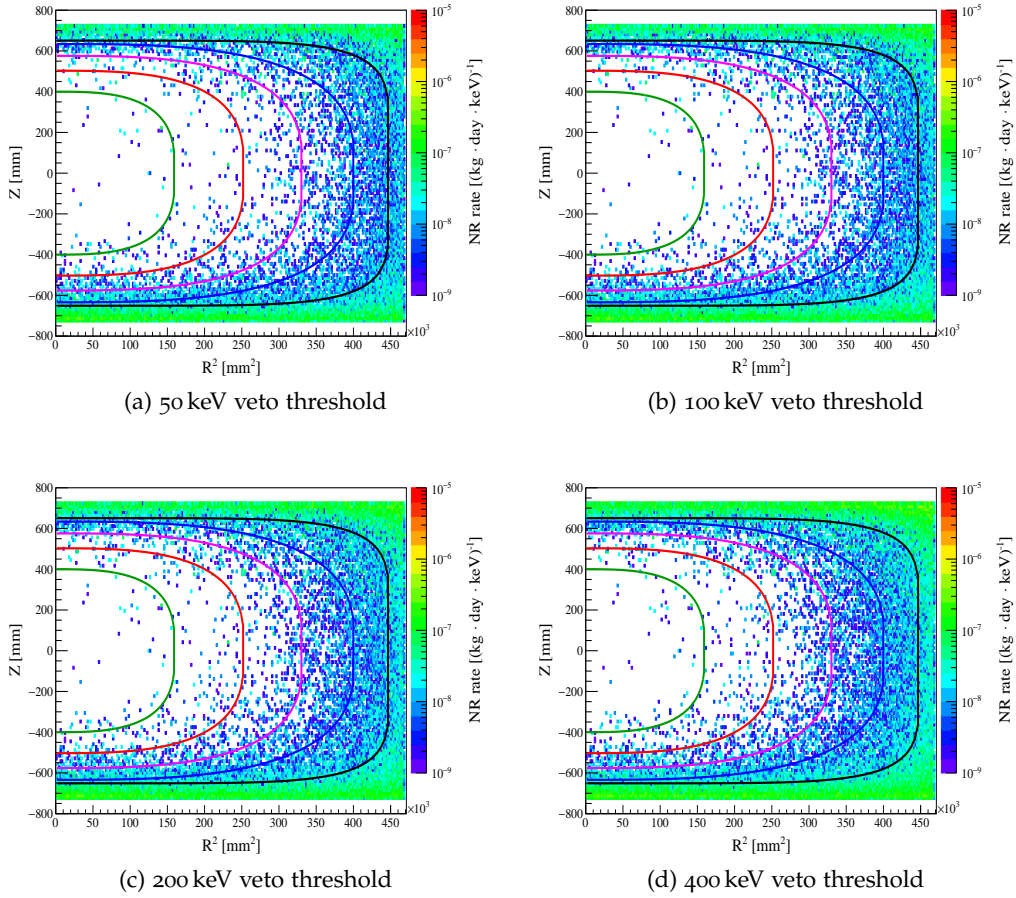
(c) 200 keV veto threshold

(d) 400 keV veto threshold

Figure 6.17: Spatial distribution of NR background events in the (4,50) keV energy range with an undoped LS, 60 cm thick veto with foam as displacer.
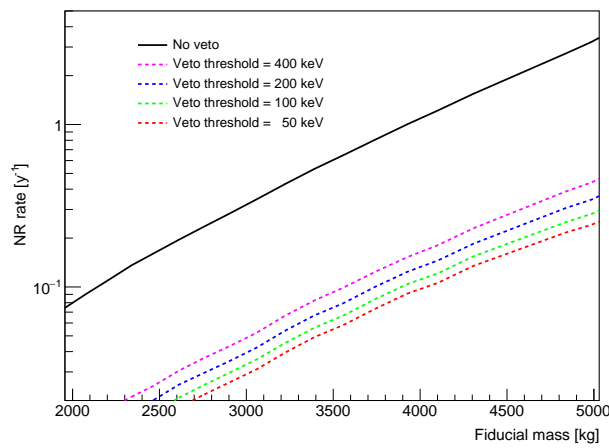

Figure 6.18: NR background rate from radiogenic neutrons as a function of the fiducial mass for an undoped LS veto 60 cm thick with foam displacer. Solid back line represents the NR background without neutron veto. Results correspond to an ideal acquisition window.
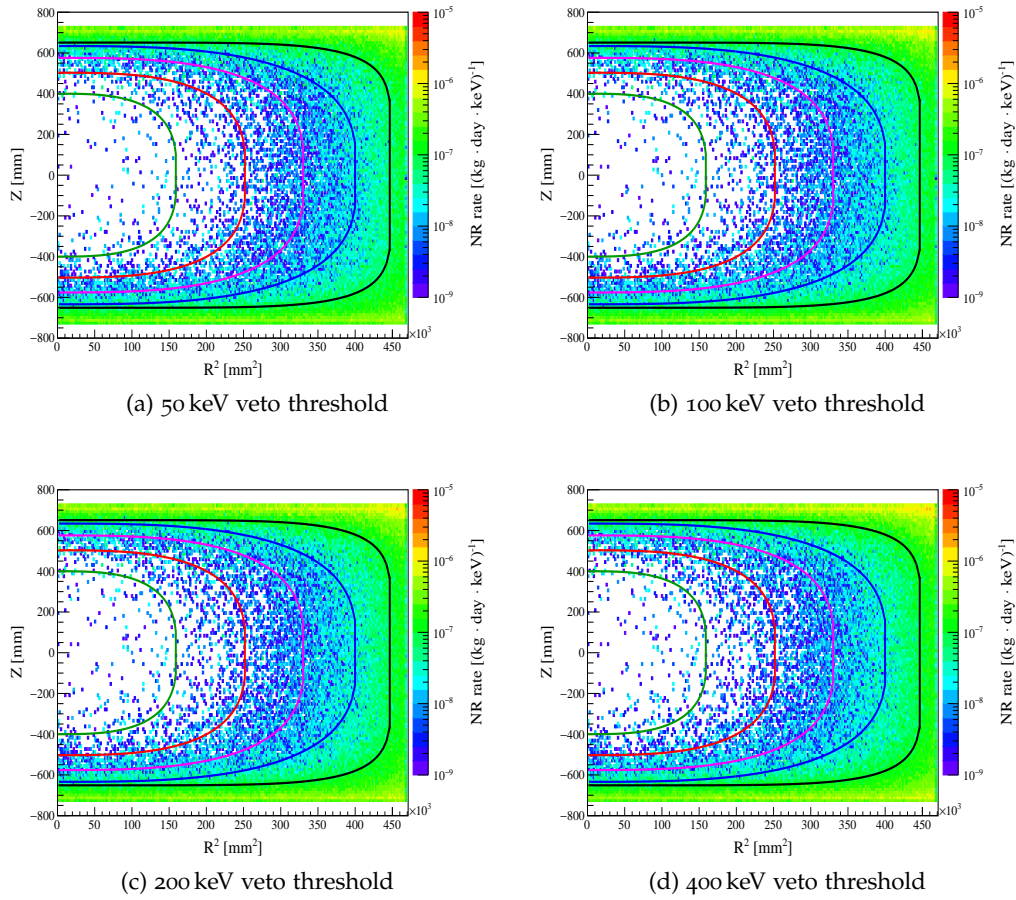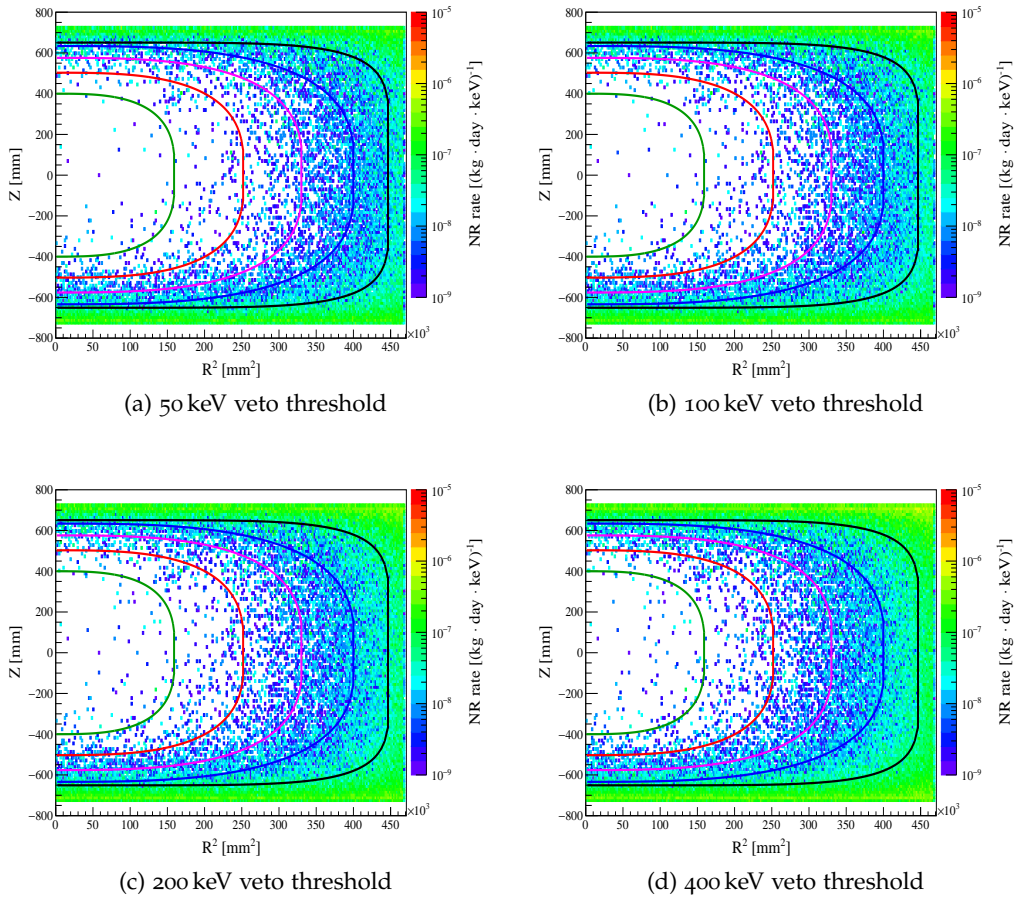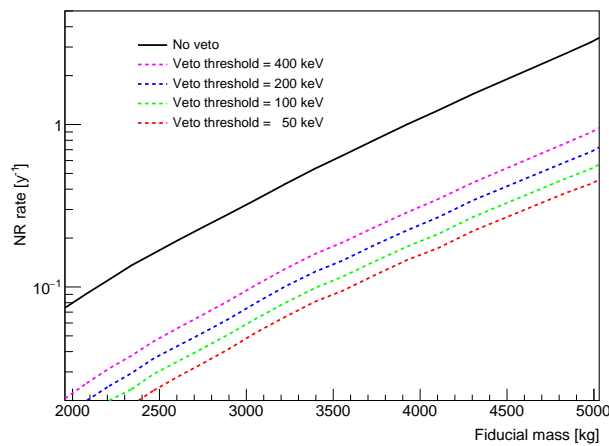
The representations of the background rate as a function of the fiducial mass confirms that the veto performance for the different energy thresholds is very similar, i.e. it is likely that a neutron event depositing 50 keV in the LS will also deposit 400 keV. Like already inferred from Figure 6.1, this time for real NR background events. It can also be concluded that the choice of material to fill the buffer between cryostat and acrylic is not trivial.

However, these results do not account for the time in which the threshold deposit is produced[9], although they give an insight into the expected performance of the veto. For example, from Figures 6.14, 6.16 and 6.18, the efficiency to veto the NR background for a 400 keV threshold is equal to $\sim 85\,\%$ for the baseline veto configuration (0.1 % Gd-LS with foam displacer), while it drops to $\sim 47\,\%$, when changing the displacer volume to water, and to $\sim 72\,\%$, when using an undoped LS mixture.

Time discrimination will show that the actual efficiency drop in both alternative configurations is larger (see also Figure 6.4).

6.4.2 *Volumes of neutron capture for NR background events*

For the three neutron veto configurations investigated in the previous section, the spatial distribution of captures in LS has also been computed. Figure 6.19 represents the actual rate of NR background events (over the entire LXe sensitive volume) which capture in LS after the recoiling signature (analogously to what Figure 6.12 shows for the initial position of these events).

The comparison between Figures 6.19(a) and 6.19(c) yields the effect that adding Gd has in terms of effectiveness for neutron capture, since for the first case there is a higher concentration of these events in the proximities of the inner edges of the vessels. The fact that most of these interactions happen after few cm of propagation through the LS has triggered the study of the neutron veto efficiency for lower thicknesses of the vessels, the results of which are presented at the end of the chapter. However, the ability to tag the neutron does not ultimately depend on confinement of this capture, but on the confinement of the deposit from the produced gamma rays, with scattering lengths of ~ 25 cm in the liquid. Figure 6.19(b) again confirms the inconvenience of a buffer filled with water, able to capture most of the neutrons generating a background event before they reach the LS volume.

---

9 For the high amount of analyzed statistics, it has been convenient to first process the energy deposit and assess the veto efficiency for an unlimited acquisition window, to afterwards compute the cuts on this window.

(a) 0.1 % Gd-LS - Foam displacer

(b) 0.1 % Gd-LS - Water displacer

(c) Undoped LS - Foam displacer
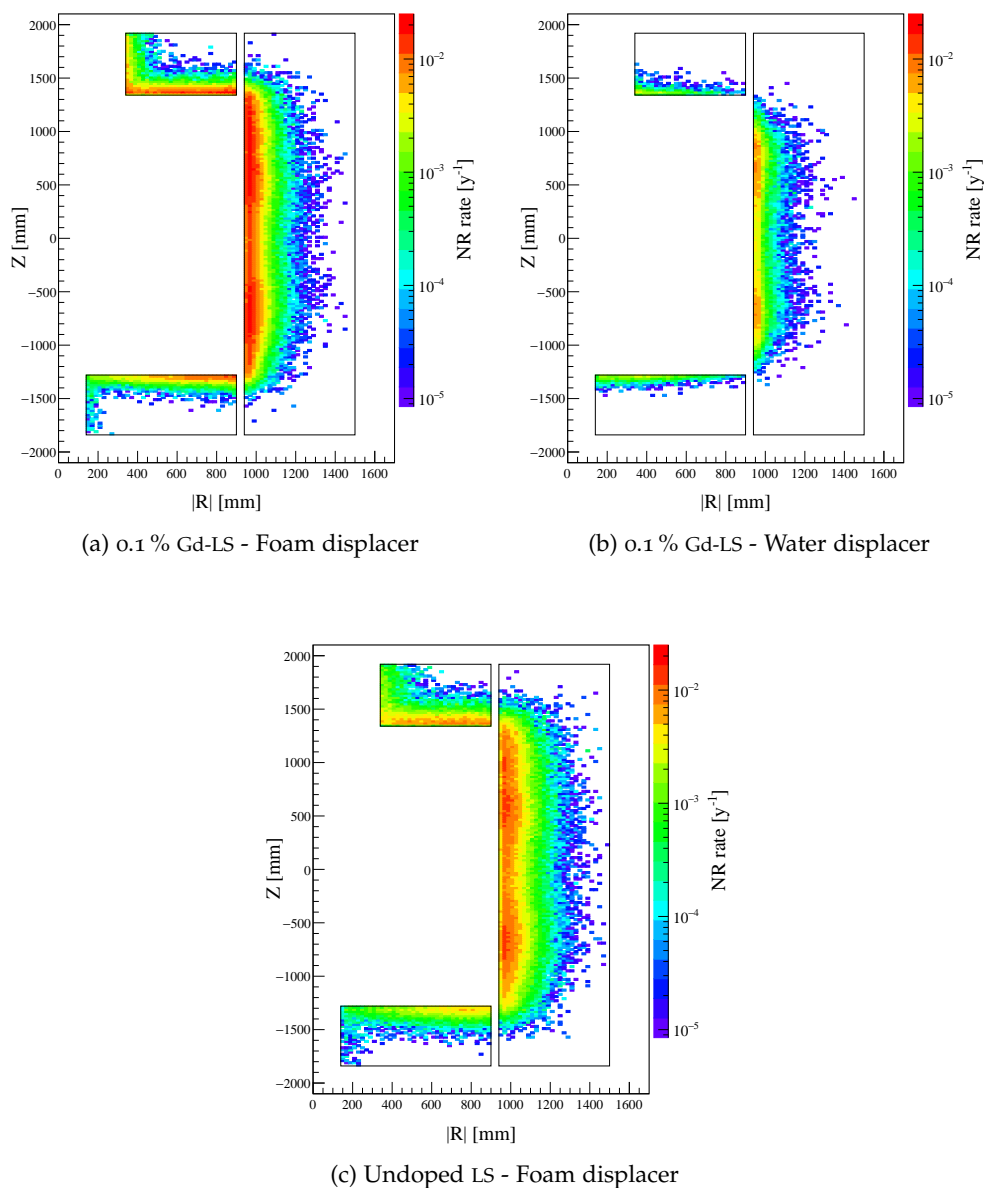
Figure 6.19: Spatial distribution of neutron captures in the LS volume for NR backgound events in the LXe sensitive detector volume. Black boxes confine the LS placed inside the acrylic vessels.

By producing such distributions for every material, one can compute the amount of captures that take place in every volume[10] for the events sorted as NR background in the LXe target. The result for the three developed veto configurations is given in Table 6.4.

---

10 Like explained in Section 6.1, for the analysis of neutron captures in detector materials the extinction of the fast neutron via inelastic scatterings is also taken into account. These cases, however, are minor and the thermal capture in the detector is the dominant contribution for this volume.

	Proportion of captures for NR background events [%]		
Volume	0.1 % Gd-LS - Foam	0.1 % Gd-LS - Water	LS - Foam
LS	71.4	11.4	57.5
(on Gd)	(61.4)	(9.9)	(-)
(on H)	(9.9)	(1.4)	(56.9)
Acrylic	9.2	4.4	16.5
Displacer[i]	0.9	55.5	1.3
Water	0.6	< 0.001	0.7
Detector	17.9	28.7	24.0

[i] When filled with water, do not confuse with the *water volume*, that accounts for what is placed between the outer acrylic and the walls of the water tank.

Table 6.4: Proportion of neutron captures in every volume for NR radiogenic background events.

6.4.3 *PE yield in the LS for NR background events*

PE yield calculation results of Section 6.2.1 are here combined with the evaluated scatter position results in LS, of Section 6.4.1, to simulate the final spectra seen in the veto detector.

Preset energy thresholds have been converted into PEs and results on the efficiency of the veto for an infinite acquisition window have been cross-checked[11]. To avoid redundancies these efficiency values are not presented in this thesis, since the final derivation of the efficiency of the neutron veto, considering the time of signal deposit, has been developed directly from the analysis of the energy deposited in the LS[12].

For illustration, the PE yield for the three explored veto arrangements is given in Figure 6.20. The raise of the PE yield for increasing number of veto PMTs and reduction of their distance to the vessels can be noticed, although for the latter variation spectra are very similar and almost fully overlapping. After the statistical treatment on the energy conversion, the PE spectra are smeared out with respect to the energy spectra, with the peak equivalent to ~ 2.2 MeV still being noticeable.

---

11 Valid only for undoped LAB and Gd-LS, given the optical properties defined for the mixture in Section 5.3.

12 This method is analogous to that employed when sorting the NR background events in the TPC (Section 6.3.2), where the corresponding S1 signal has been used as a cross-check for the results derived directly taking into account the recoiling energy in LXe.
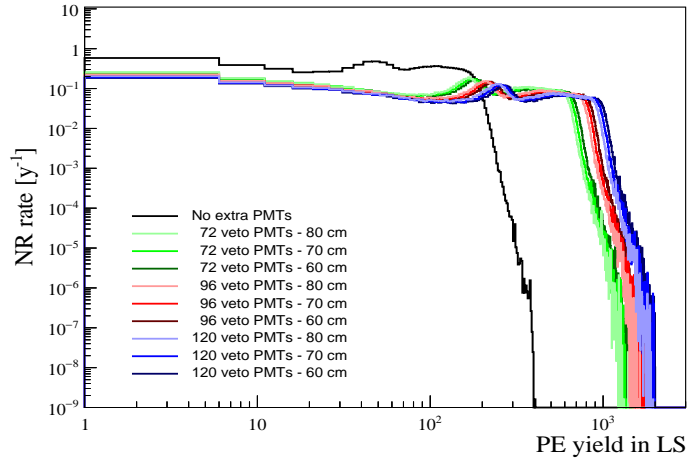
(a) 0.1 % Gd-LS - Foam displacer
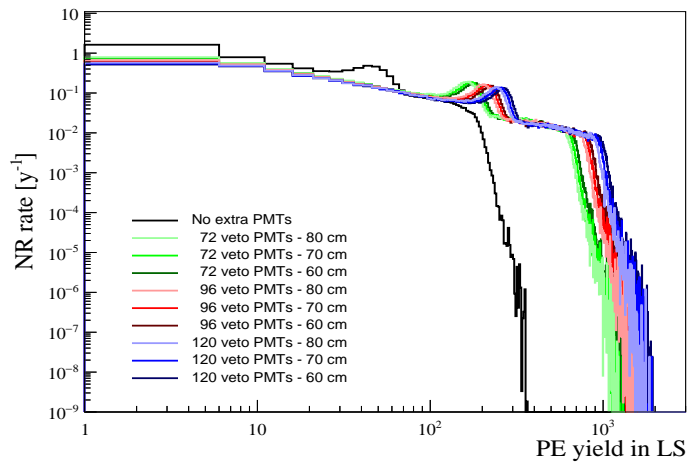
(b) 0.1 % Gd-LS - Water displacer
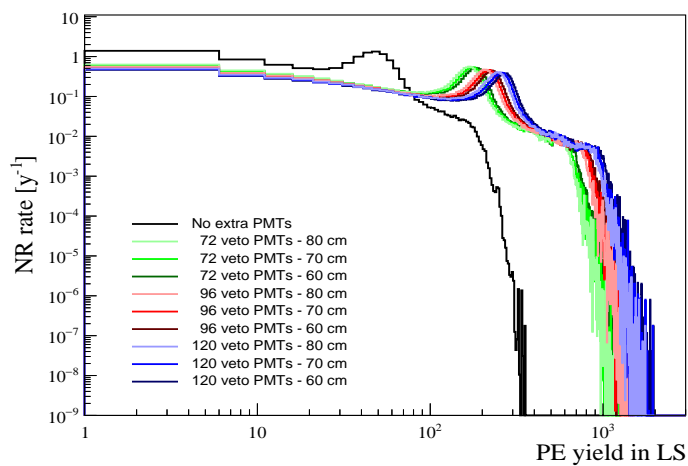
(c) Undoped LS - Foam displacer

Figure 6.20: PE yield distribution in the LS for NR backgound events. The integral of every spectra yields the NR background in the whole LXe target: $13 \pm 2 \ \mathrm{y}^{-1}$.

6.4.4 *Veto acquisition window*

Finally, the effects of varying the veto time window on the observed vetoing rate in LS is estimated. This will ultimately have an effect on overall detector lifetime and is an important component of the final dark matter analysis. These effects are applied to each of the three designs developed in the previous sections and final results on the expected NR rate are provided.

Based on the performance versus time properties (first investigated in Section 6.1.2), along with some basic studies (still under development) on the dead-time properties that the neutron veto should fulfil, four different veto acquisition windows τ have been set and applied on the events previously sorted as vetoed ones: 100, 150, 200 and 250 μs, the latter of them corresponding to roughly five capture times for a 0.1 % Gd-LS veto and neutrons produced inside the XENONnT detector.

Although the main output is the actual efficiency of the veto after setting finite acquisition times, calculated in the next section, the spectra corresponding to the results for the developed configurations are shown for completeness in Figures 6.21 to 6.23; where the black solid line represents the NR background rate witout veto for every spectra and the dashed lines correspond to the results for an infinite acquisition window, derived in Section 6.4.1.

Following the set of figures, Table 6.5 presents a complete relation of the NR radiogenic background results for every of the tested veto arrangements, considering veto time windows equal to 100 and 250 μs, as well as the ideal case of unlimited aquisition time.

(a) $E_{th} = 50\,keV$

(b) $E_{th} = 100\,keV$

(c) $E_{th} = 200\,keV$

(d) $E_{th} = 400\,keV$

Figure 6.21: NR radiogenic background as a function of the fiducial mass for a 0.1 % Gd-LS veto 60 cm thick with foam displacer. Dashed lines correspond to an infinite acquisition time (graphs from Figure 6.14).

(a) $E_{th} = 50 \, keV$

(b) $E_{th} = 100 \, keV$

(c) $E_{th} = 200 \, keV$

(d) $E_{th} = 400 \, keV$
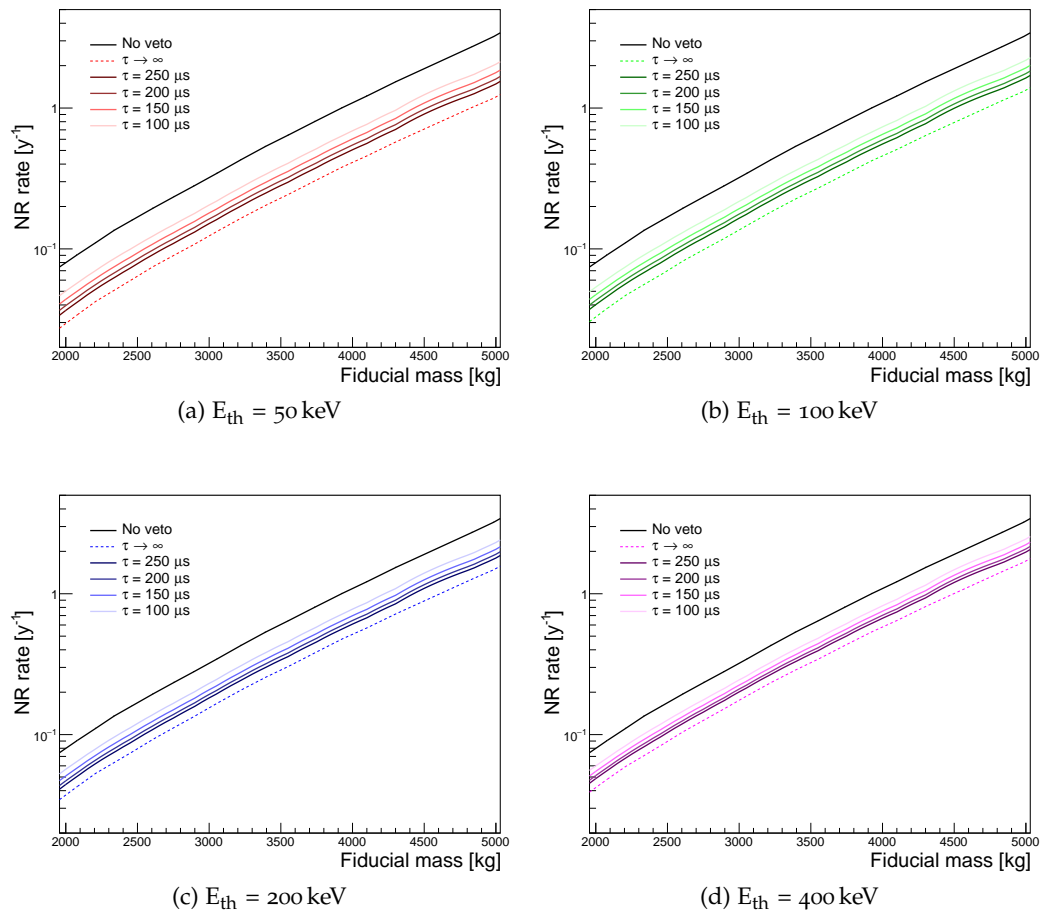
Figure 6.22: NR radiogenic background as a function of the fiducial mass for a 0.1 % Gd-LS veto 60 cm thick with water displacer. Dashed lines correspond to an infinite acquisition time (graphs from Figure 6.16).
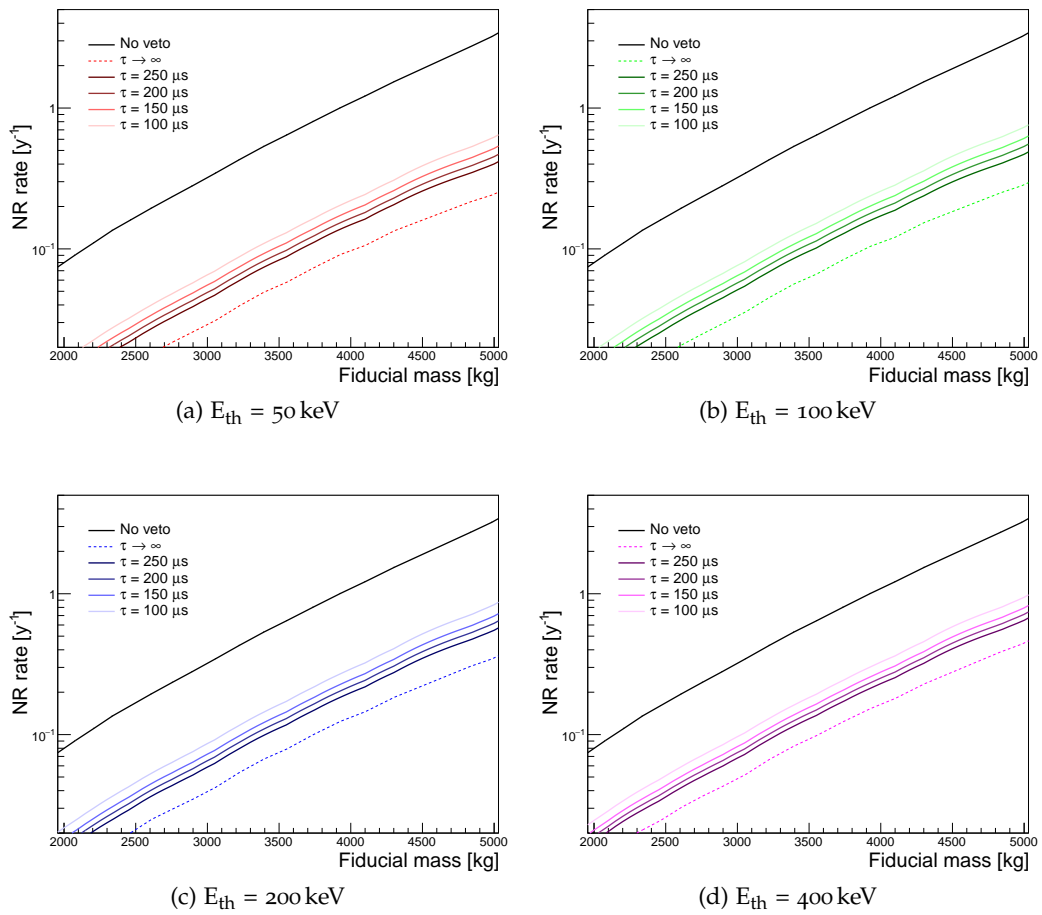
Figure 6.23: NR radiogenic background as a function of the fiducial mass for an undoped LS veto 60 cm thick with foam displacer. Dashed lines correspond to an infinite acquisition time (graphs from Figure 6.18).
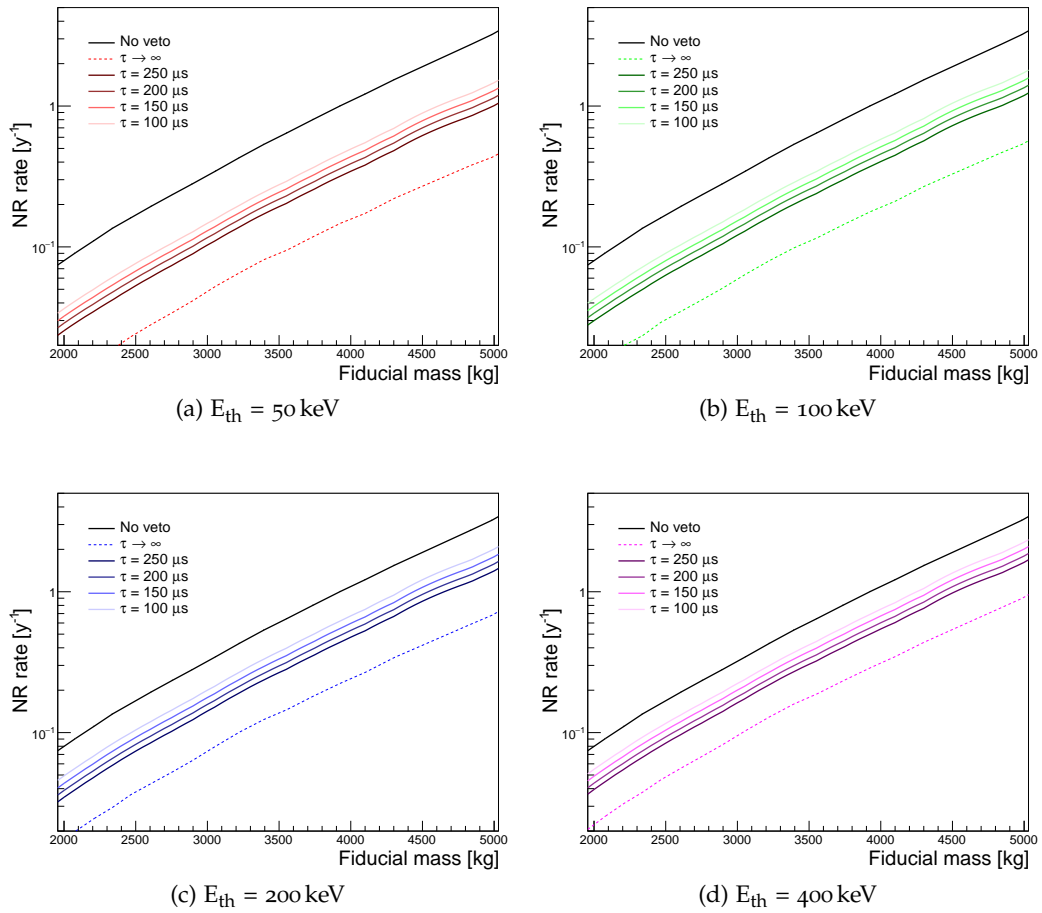
			0.1 Gd-LS - Foam				0.1 Gd-LS - Water				Undoped LS - Foam			
			NR radiogenic background rate [y⁻¹]											

NR radiogenic background rate [y^{-1}]

τ [μs]	FV [t]	No veto	0.1 Gd-LS - Foam				0.1 Gd-LS - Water				Undoped LS - Foam			
			50 keV	100 keV	200 keV	400 keV	50 keV	100 keV	200 keV	400 keV	50 keV	100 keV	200 keV	400 keV
100 μs	4	**1.1(2)**	0.22(4)	0.26(4)	0.29(5)	0.33(6)	0.68(12)	0.74(12)	0.78(13)	0.82(14)	0.49(8)	0.58(10)	0.67(11)	0.75(13)
	4.2	**1.4(2)**	0.28(5)	0.35(5)	0.36(6)	0.41(7)	0.87(15)	0.9(2)	1.0(2)	1.0(2)	0.62(11)	0.73(12)	0.85(14)	0.9(2)
	4.4	**1.8(3)**	0.35(6)	0.41(7)	0.46(8)	0.52(9)	1.1(2)	1.2(2)	1.2(2)	1.3(2)	0.79(13)	0.9(2)	1.1(2)	1.2(2)
	4.6	**2.2(4)**	0.43(7)	0.50(9))	0.57(10)	0.65(11)	1.4(2)	1.5(3)	1.6(3)	1.6(3)	1.0(2)	1.2(2)	1.4(2)	1.5(3)
	4.8	**2.7(5)**	0.51(8)	0.60(10)	0.69(12)	0.77(13)	1.7(3)	1.8(3)	1.9(3)	2.0(3)	1.2(2)	1.4(2)	1.6(3)	1.8(3)
	5	**3.3(6)**	0.62(11)	0.73(12)	0.84(14)	0.9(2)	2.0(3)	2.2(4)	2.3(4)	2.4(4)	1.5(2)	1.7(3)	2.0(3)	2.2(4)
250 μs	4	**1.1(2)**	0.14(3)	0.17(3)	0.20(3)	0.23(4)	0.51(9)	0.56(10)	0.61(10)	0.67(11)	0.34(6)	0.40(7)	0.48(8)	0.54(9)
	4.2	**1.4(2)**	0.18(3)	0.21(4)	0.25(4)	0.29(5)	0.63(11)	0.69(12)	0.76(13)	0.84(14)	0.43(7)	0.51(8)	0.60(10)	0.68(12)
	4.4	**1.8(3)**	0.23(4)	0.27(5)	0.31(5)	0.36(6)	0.80(14)	0.9(2)	1.0(2)	1.1(2)	0.55(9)	0.65(11)	0.76(13)	0.87(15)
	4.6	**2.2(4)**	0.28(5)	0.33(6)	0.38(7)	0.45(8)	1.1(2)	1.1(2)	1.2(2)	1.3(2)	0.69(12)	0.81(14)	1.0(2)	1.1(2)
	4.8	**2.7(5)**	0.34(6)	0.39(7)	0.46(8)	0.54(9)	1.2(2)	1.3(2)	1.5(2)	1.6(3)	0.82(14)	0.97(2)	1.1(2)	1.3(2)
	5	**3.3(6)**	0.40(7)	0.47(8)	0.55(10)	0.65(11)	1.5(3)	1.6(3)	1.8(3)	2.0(3)	1.0(2)	1.2(2)	1.4(2)	1.6(3)
∞	4	**1.1(2)**	0.097(2)	0.11(2)	0.13(2)	0.16(3)	0.41(7)	0.46(8)	0.52(9)	0.58(10)	0.16(3)	0.19(3)	0.24(4)	0.31(5)
	4.2	**1.4(2)**	0.12(2)	0.14(2)	0.16(3)	0.20(3)	0.52(9)	0.57(10)	0.64(11)	0.73(12)	0.20(3)	0.24(4)	0.3(5)	0.39(7)
	4.4	**1.8(3)**	0.15(3)	0.17(3)	0.21(4)	0.26(4)	0.65(11)	0.73(12)	0.82(14)	0.9(2)	0.25(4)	0.30(5)	0.39(7)	0.50(8)
	4.6	**2.2(4)**	0.18(3)	0.21(4)	0.25(4)	0.32(5)	0.82(14)	0.9(2)	1.0(2)	1.2(2)	0.31(5)	0.38(6)	0.48(8)	0.62(11)
	4.8	**2.7(5)**	0.21(4)	0.24(4)	0.30(5)	0.38(6)	1.0(2)	1.1(2)	1.2(2)	1.4(2)	0.37(6)	0.45(8)	0.57(10)	0.75(13)
	5	**3.3(6)**	0.24(4)	0.29(5)	0.35(6)	0.45(8)	1.2(2)	1.3(2)	1.5(3)	1.7(3)	0.44(7)	0.54(9)	0.70(12)	0.9(2)

Table 6.5: Resulting NR radiogenic background for different neutron veto configuration, energy deposit thresholds and acquisition windows (τ). For a recoiling deposit from 4 to 50 keV in the corresponding FV.

6.4.5 *Veto tagging efficiency*

The efficiency for all the explored veto arrangements is obtained by rescaling the corresponding NR background curves with respect to the one derived for the case without veto, in Figures 6.21 to 6.23). Since these integrals can only be performed for singular FVs, results depicted in this section are given for FVs of 4 t (solid lines), as the minimum assumed volume for XENONnT operation, and for 5 t (dashed lines), as an optimistic design benchmark for a total LXe target ot $\sim$ 6 t.

Results for the baseline configuration defined in this thesis are shown in Figure 6.24, in comparison with the analogous case with water instead of foam as displacer material.
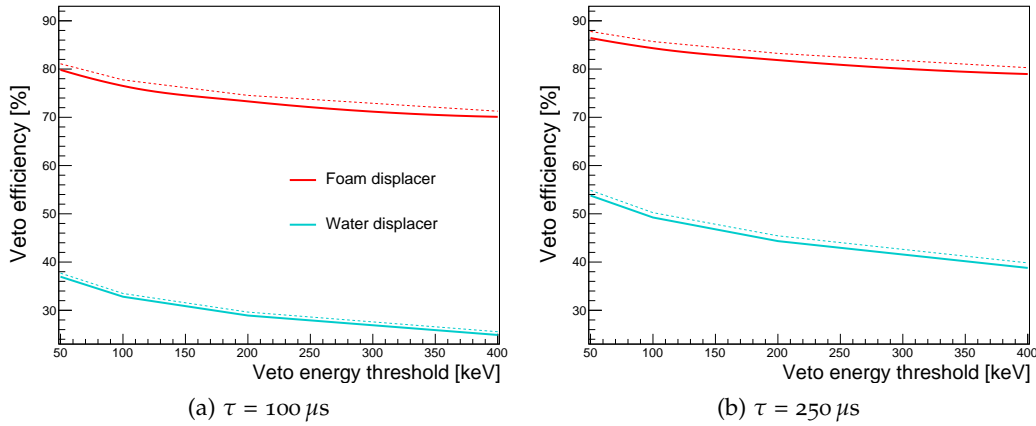

(a) $\tau = 100\,\mu$s

(b) $\tau = 250\,\mu$s

Figure 6.24: Veto efficiency for a 0.1 % Gd-LS veto with 60 cm thickness, for varying displacer materials.

For an optimal veto window of 250 μs, a neutron veto deploying a 0.1 % Gd-LS mixture and foam as displacer material performs with an efficiency ranging from 82 to 88 % for vetoing deposit thresholds up to 400 keV; whereas this efficiency drops to values from 70 to 82 % for a 100 μs veto window.

The final impact of replacing the polyurethane foam with water is revealed in Figure 6.24, with efficiencies of about half of those for the foam displacer configuration.

Figure 6.25 compares the derived efficiency for the baseline veto configuration with those corresponding to identical veto mixtures with different vessel thicknesses, where it can be seen that efficiencies for a neutron veto thickness of 50 cm are almost equal to those for a 60 cm veto.

(a) $\tau = 100\,\mu$s

(b) $\tau = 250\,\mu$s
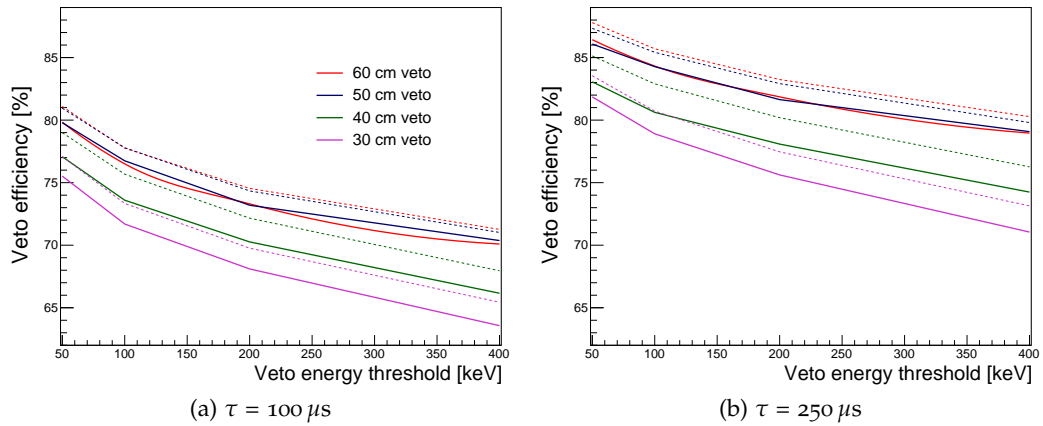
Figure 6.25: Veto efficiency for a 0.1 % Gd-LS veto with foam as displacer material, for varying thicknesses.

Finally, Figure 6.26 yields the comparison between the baseline configuration with respect to geometrically identical outer detectors with different proportions of Gd doping.

(a) $\tau = 100\,\mu$s

(b) $\tau = 250\,\mu$s
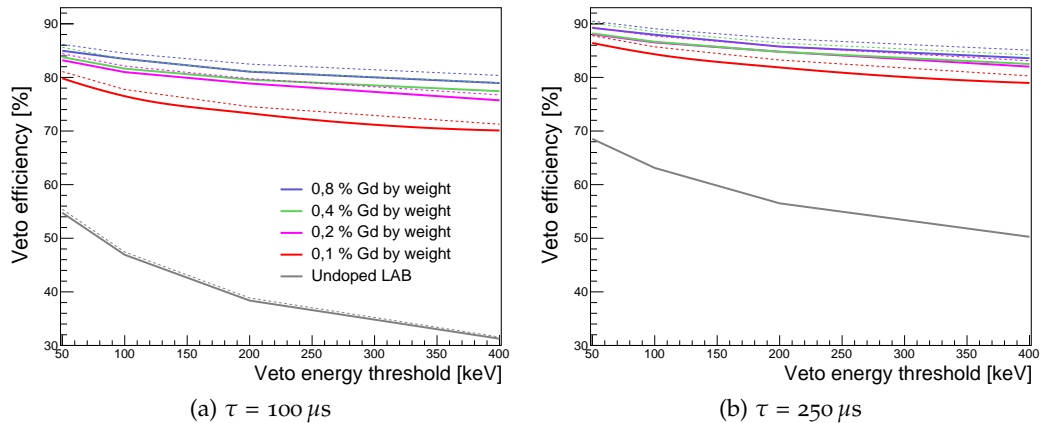
Figure 6.26: Veto efficiency for a veto with 60 cm thickness and foam as displacer material, for varying proportions of Gd in the scintillating mixture.

CONCLUSIONS AND OUTLOOK

In the context of the XENON1T upgrade towards XENONnT, expected to take place within two years, radiogenic nuclear recoil background studies turned out to be crucial in order to effectively define the conditions for the dark matter search operation of the detector.

With the goal of optimizing the liquid xenon fiducial volume in XENONnT, studies on the viability of deploying a gadolinium-doped liquid scintillator neutron veto have taken place. After verifying the expected neutron background for the new designed time projection chamber, this work has focused on developing a realistic scenario for the operation of such an outer detector.

Results indicate that, for a scintillating mixture with 0.1 % of gadolinium by weight, veto efficiencies larger than 80 % can be achieved against radiogenic nuclear recoil background events; if at the same time this mixture is contained in an hermetically sealed cylindrical structure arround the XENONnT outer cryostat, preventing water from penetrating the buffer between this volume and the acrylic liquid scintillator vessels. Considering a veto acquisition window between 100 and 250 μs since the moment of recoiling deposit in the time projection chamber, and setting a conservative energy threshold of 200 keV in liquid scintillator, beyond the carbon-14 β-decay line ($\sim$ 186 keV), this efficiency has been assessed under realistic simulation constraints.

One of the main mechanical challenges for the realization of this neutron veto lies on the ability to fill this buffer with a low-density material, without altering the pressure stability of the vessels subsystem. Another approach to solve the negative impact that water has in the neutron tagging efficiency might be to design acrylic vessels able to operate a few milimeters away from the outer cryostat, allowing for the presence of water in the remaining buffer. This possibility, however, could also endanger the pressure stability of the acrylic containers, depending on the complexity of the designed geometry.

By loading the liquid scintillator with higher proportions of gadolinium, the results on the efficiency increase up to an 8 %, triggering the argument on whether one should aim for such high proportions, also considering the chemical challenges that the mixture synthesis entails.

Simulations to derive the photoelectron yield of the veto outer detector have been also carried out, pointing to the necessity of adding a new array of photomultiplier tubes, placed closer to the detector cryostat than the currently operative ones. To verify the assumptions made in this work regarding the safe position

of this array, new simulations need to be perfomed in order to estimate the induced radioactivity induced by the photosensors in the scintillator. Moreover, the purity levels of the liquid scintillator itself should be also studied, with the goal of providing a number on the dead-time of the neutron veto and give a clear statement on the acquisition windows of veto operation that can be assumed.

DIFFERENTIAL RADIOGENIC NEUTRON YIELD

The radiogenic neutron yield for all the involved components in NR background simulations is derived in Section 5.4, where the differential energy distribution for PTFE is also shown as an example (see Figure 5.8). The remaining spectra are given in the figure below.
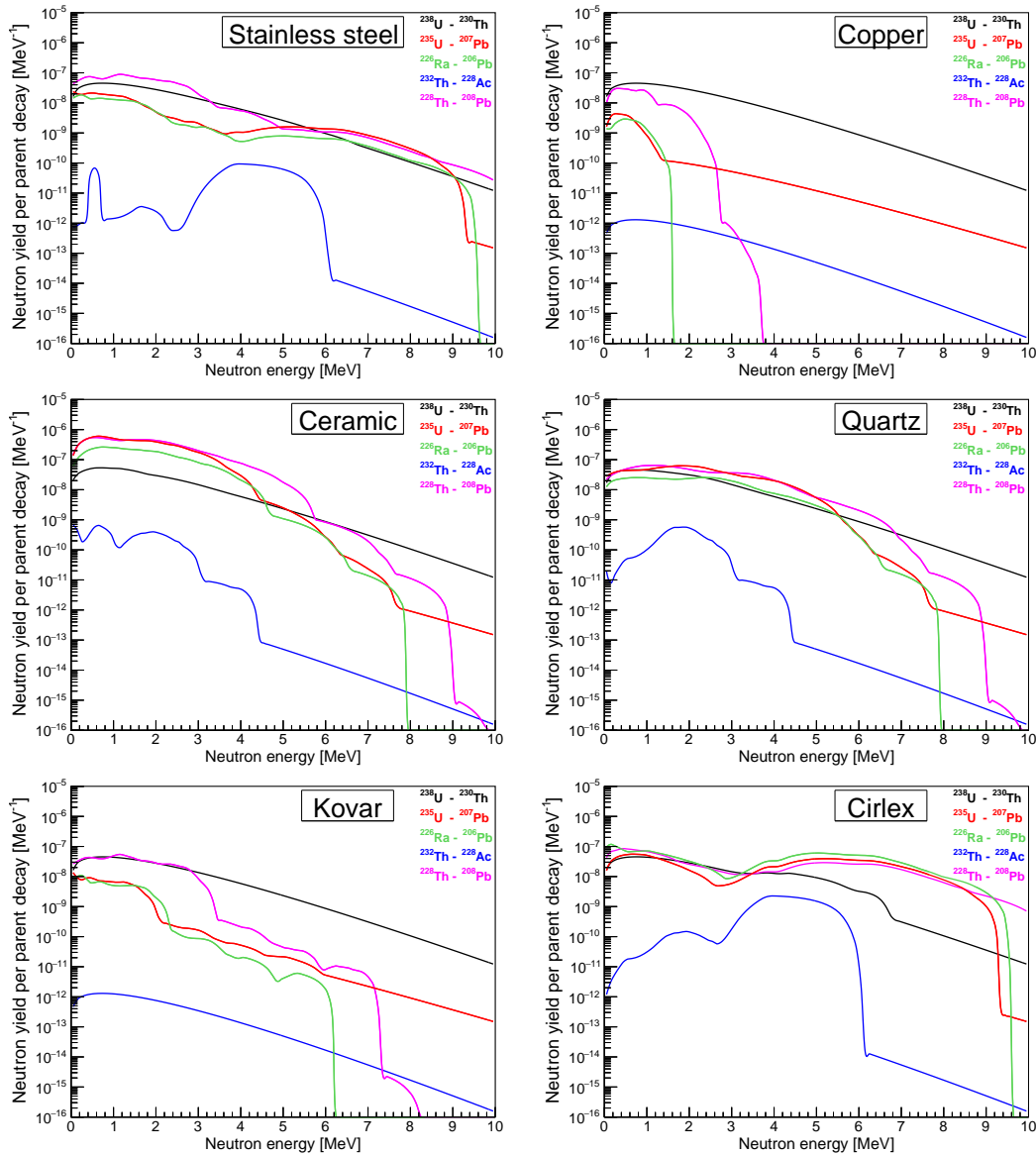

Figure A.1: Differential yield of radiogenic neutrons in SS, copper, ceramic, quartz, kovar and cirlex. ^{238}U and ^{238}Th chains are separated in two branches, to account for their potential disequilibrium.

[1] E. Öpik. Selective absorption of light in space, and the dynamics of the universe. *Bull. de la Soc. Astr. de Russie 21 150*, 1915.

[2] J. C. Kapteyn. First attempt at a Theory of the Arrangement and Motion of the Sidereal System. *Astrophys. J. 55 302*, 1922.

[3] J. H. Jeans. The motions of stars in a Kapteyn universe. *MNRAS. 82 122*, 1922.

[4] J. H. Oort. The force exerted by the stellar system in the direction perpendicular to the galactic plane and some related problems. *Bull. Astron. Inst. Netherlands 6 249*, 1932.

[5] F. Zwicky. Die Rotverschiebung von extragalaktischen Nebeln. *Helvetica Physica Acta 6 110*, 1933.

[6] V. C. Rubin, N. Thonnard, and W. K. Ford. Extended rotation curves of high-luminosity spiral galaxies. *Astrophys. J. 225 L107*, 1978.

[7] K. G. Begeman, A. H. Broeils and R. H. Sanders. Extended rotation curves of spiral galaxies - Dark haloes and modified dynamics. *Mon. Not. Roy. Astron. Soc. 249 523*, 1991.

[8] A. Einstein. Lens-like action of a star by the deviation of light in the gravitational field. *Science 84 506*, 1936.

[9] D. Clowe, M. Bradač, A. H. Gonzalez, M. Markevitch, S. W. Randall, C. Jones and D. Zaritsky. A direct empirical proof of the existence of dark matter. *Astrophys. J. 648 L109*, 2006.

[10] P. A. R. Ade *et al.* (Planck collaboration). Planck 2015 results. I. Overview of products and scientific results. *Astron. Astrophys. 594 A1*, 2016.

[11] P. A. R. Ade *et al.* (Planck collaboration). Planck 2015 results: XIII. Cosmological parameters. *Astron. Astrophys. 594 A13*, 2016.

[12] M. Roos. Astrophysical and cosmological probes of dark matter. *J. Mod. Phys. 3 1152*, 2012.

[13] M. Milgrom. A modification of the Newtonian dynamics as a possible alternative to the hidden mass hypothesis. *Astrophys. J. 270 365*, 1983.

[14] J. D. Bekenstein. Relativistic gravitation theory for the modified Newtonian dynamics paradigm. *Phys. Rev. D 70 083509*, 2004.

[15] G. Bertone. *Particle dark matter: observations, models and searches.* Cambridge University Press, 2010.

[16] C. Alcock *et al.* (MACHO collaboration). The MACHO project: Microlensing results from 5.7 years of LMC observations. *Astrophys. J.* **542** *281*, 2000.

[17] G. Jungman, M. Kamionkowski and K. Griest. Supersymmetric dark matter. *Phys. Rep.* **267** *195*, 1996.

[18] T. Marrodán Undagoitia and L. Rauch. Dark matter direct-detection experiments. *J. Phys. G* **43** *013001*, 2016.

[19] L. Baudis. Dark matter detection. *J. Phys. G* **43** *044001*, 2016.

[20] M. Schumann. Dual-phase liquid xenon detectors for dark matter searches. *JINST* **9** *C08004*, 2014.

[21] E. Aprile *et al.* (XENON collaboration). Design and performance of the XENON10 dark matter experiment. *Astropart. Phys.* **34** *679*, 2011.

[22] E. Aprile *et al.* (XENON collaboration). The XENON100 dark matter experiment. *Astropart. Phys.* **35** *573*, 2012.

[23] E. Aprile *et al.* (XENON collaboration). Dark matter results from 225 live days of XENON100 data. *Phys. Rev. Lett.* **109** *131801*, 2012.

[24] D. S. Akerib *et al.* (LUX collaboration). First results of the LUX dark matter experiment. *Phys. Rev. Lett.* **112** *091303*, 2014.

[25] E. Aprile *et al.* (XENON collaboration). XENON100 dark matter results from a combination of 477 live days. *Phys. Rev. D* **94** *122001*, 2016.

[26] E. Aprile *et al.* (XENON collaboration). The XENON1T dark matter search experiment. *Springer Proc. Phys.* **148** *93*, 2013.

[27] E. Aprile *et al.* (XENON collaboration). The xenon1t dark matter experiment. *In preparation*, 2017.

[28] E. Aprile *et al.* (XENON collaboration). Conceptual design and simulation of a water Cherenkov muon veto for the XENON1T experiment. *JINST* **9** *P11006*, 2014.

[29] E. Aprile *et al.* (XENON collaboration). Lowering the radioactivity of the photomultiplier tubes for the XENON1T dark matter experiment. *Eur. Phys. J. C* **75** *546*, 2015.

[30] E. Aprile *et al.* (XENON collaboration). Material radioassay and selection for the XENON1T dark matter experiment. *Under review at the time of writing*, 2017.

[31] E. Aprile *et al.* (XENON collaboration). Physics reach of the XENON1T dark matter experiment. *JCAP* **2016** *27*, 2016.

[32] Wikimedia Commons. Benzene representation. 2009.

[33] A. Jabłoński. Über den Mechanismus der Photolumineszenz von Farbstoff-phosphoren. *Zeitschrift fur Physik* **21** *38*, 1935.

[34] J. B. Birks. *The theory and practice of scintillation counting*. Pergamon Press, 1964.

[35] G.F. Knoll. *Radiation detection and measurement*. John Wiley & Sons, 4th edition, 2010.

[36] C. Buck and M. Yeh. Metal-loaded organic scintillators for neutrino physics. *J. Phys. G* **43** *093001*, 2016.

[37] C. Aberle, C. Buck, F. X. Hartmann and S. Schönert. Light yield and energy transfer in a new gd-loaded liquid scintillator. *Chem. Phys. Lett.* **516** *257*, 2011.

[38] J. B. Birks. Scintillations from organic crystals: specific fluorescence and relative response to different radiations. *Proc. Phys. Soc. A* **64** *874*, 1951.

[39] F. Reines and C. L. Cowan. Detection of the free neutrino. *Phys. Rev.* **92** *830*, 1953.

[40] J. Cao and K. B. Luk. An overview of the Daya Bay reactor neutrino experiment. *Nucl. Phys. B* **908** *62*, 2016.

[41] International Atomic Energy Agency. *Database of prompt gamma rays from slow neutron capture for elemental analysis*. IAEA, 2007.

[42] A. Wright, P. Mosteiro, B. Loer and F. Calaprice. A highly efficient neutron veto for dark matter experiments. *Nucl. Instrum. Meth. A* **644** *18*, 2011.

[43] S. Westerdale, E. Shields and F. Calaprice. A prototype neutron veto for dark matter detectors. *Astropart. Phys.* **79** *10*, 2016.

[44] P. Agnes *et al.* (DarkSide collaboration). The veto system of the DarkSide-50 experiment. *JINST* **11** *P03016*, 2016.

[45] D. S. Akerib *et al.* (LZ collaboration). LUX-ZEPLIN (LZ) Conceptual Design Report. 2015. arXiv:1509.02910.

[46] W. Beriguete, J. Cao, Y. Ding, S. Hans, K. M. Heeger, L. Hu *et al.* Production of a gadolinium-loaded liquid scintillator for the Daya Bay reactor neutrino experiment. *Nucl. Instrum. Meth. A* **763** *82*, 2014.

[47] J. S. Park, J. Lee, I. S. Yeo, W. Q. Choi, J. K. Ahn, J. H. Choi *et al.* Production and optical properties of gd-loaded liquid scintillator for the RENO neutrino detector. *Nucl. Instrum. Meth. A* **707** *45*, 2013.

[48] S. Agostinelli *et al.* (GEANT4 collaboration). GEANT4: a simulation toolkit. *Nucl. Instrum. Meth. A* **422** *314*, 2003.

[49] M. Schumann. *Internal XENON collaboration note*, 2016.

[50] R. Othegraven, technician at the *Institut für Physik* in Mainz. Private communication. 2016.

[51] X. Hua-Lin, L. Xiao-Bo, Z. Dong, C. Jun, W. Liang-Jian and W. Nai-Yan. Study of absorption and re-emission processes in a ternary liquid scintillation system. *Chin. Phys. C 34 1724*, 2010.

[52] C. Buck, B. Gramlich and S. Wagner. Light propagation and fluorescence quantum yields in liquid scintillators. *JINST 10 P09007*, 2015.

[53] J. K. Ahn *et al.* (RENO collaboration). RENO: An experiment for neutrino oscillation parameter θ_{13} using reactor neutrinos at Yonggwang. 2010. arXiv:1003.1391.

[54] B. von Krosigk, L. Neumann, R. Nolte, S. Rottger and K. Zuber. Measurement of the proton light response of various LAB based scintillators and its implication for supernova neutrino detection via neutrino-proton scattering. *Eur. Phys. J. C 73 2390*, 2013.

[55] B. von Krosigk, M. Chen, S. Hans, A. R. Junghans, T. Kögler, C. Kraus *et al.* Measurement of α-particle quenching in LAB based scintillator in independent small-scale experiments. *Eur. Phys. J. C 76 109*, 2016.

[56] Hamamatsu Photonics K.K. *Large photocathode area photomultiplier tubes*, 2016. http://www.hamamatsu.com/resources/pdf/etd/LARGE_AREA_PMT_TPMH1286E.pdf, Accessed April 2017.

[57] C. Geis, C. Grignon, U. Oberlack, R. Othegraven, D. Ramírez García and Q. Weitzel. Optical response of highly reflective film used in the water Cherenkov muon veto of the XENON1T dark matter experiment. *In preparation*, 2017.

[58] C. Geis. *Untersuchung der DF2000MA Reflektorfolie in Hinsicht auf ihre Verwendung im XENON1T MuonVeto*, Research thesis, Johannes Gutenber-Universität Mainz, Germany, 2012.

[59] 3M. *Daylighting film DF2000MA*, 2007. http://multimedia.3m.com/mws/media/7464690/3m-daylighting-film-df2000ma.pdf, Accessed April 2017.

[60] C. Buck, scientist at the *Max-Planck-Institut für Kernphysik* in Heidelberg. Private communication. 2016.

[61] I. S. Yeo, J. H. Jang, M. S. Kim, J. K. Ahn, S. R. Baik, E. I. Choi *et al.* Measurement of the refractive index of the LAB-based liquid scintillator and acrylic at RENO. *Phys. Scr. 82 065706*, 2010.

[62] F. P. An, Q. An, J. Z. Bai, A. B. Balantekin, H. R. Band, W. Beriguete *et al.* Improved measurement of electron antineutrino disappearance at Daya Bay. *Chin. Phys. C 37 011001*, 2013.

[63] F. An, G. An, Q. An, V. Antonelli, E. Baussan, J. Beacom *et al.* Neutrino physics with JUNO. *J. Phys. G* **43** *030401*, 2016.

[64] W. B. Wilson, R. T. Perry, W. S. Charlton, T. A. Parish, G. P. Estes, T. H. Brown *et al.* SOURCES-4A technical report LA-13639-MS. 1999.

[65] A. Kish. *Dark matter search with the XENON100 experiment*. PhD thesis, Universität Zürich, Switzerland, 2011.

[66] E. Aprile *et al.* (XENON collaboration). The neutron background of the XENON100 dark matter search experiment. *J. Phys. G* **40** *115201*, 2013.

[67] *Credit/citations for data files distributed with GEANT4.* http://geant4.web.cern.ch/geant4/support/datafiles_origin.shtml, Accessed April 2017.

[68] G. Horton-Smith. *Additional gadolinium Support for GLG4sim.* http://neutrino.phys.ksu.edu/~GLG4sim/Gd.html, Accessed April 2017.

[69] C. D. Roecker. *Measurement of the high-energy neutron flux above and below ground*. PhD thesis, University of California, Berkeley, United States of America, 2016.

[70] *GEANT4 Forum for processes involving hadronic interactions.* http://hypernews.slac.stanford.edu/HyperNews/geant4/get/hadronprocess/1404.html, Accessed April 2017.

[71] *G4Scintillation.cc file documentation.* http://www.apc.univ-paris7.fr/~franco/g4doxy/html/G4Scintillation_8cc-source.html, Accessed April 2017.

[72] E. Aprile *et al.* (XENON collaboration). Analysis of the XENON100 dark matter search data. *Astropart. Phys.* **54** *11*, 2014.

[73] E. Hogenbirk. *Internal XENON collaboration note*, 2017.

[74] M. Selvi. *Internal XENON collaboration note*, 2017.

[75] M. Szydagis, N. Barry, K. Kazkaz, J. Mock, D. Stolp, M. Sweany *et al.* NEST: a comprehensive model for scintillation yield in liquid xenon. *JINST* **6** *P10002*, 2011.

ERKLÄRUNG ZUR SELBSTSTÄNDIGKEIT

Hiermit erkläre ich, dass die vorliegende Arbeit selbständig, ohne fremde Hilfe und ohne Benutzung anderer als die angegebenen Quellen von mir angefertigt wurde.

Mainz, May 2017

————————————————————
Diego Ramírez García